A Study of the Centrally Produced K^+K^- System at the CERN Ω Spectrometer

Brian Christopher Earl

Thesis submitted to the Faculty of Science of the University of Birmingham for the degree of Doctor of Philosophy

Omega Group, Particle Physics
School of Physics and Astronomy
The University of Birmingham

March, 1999

Synopsis

QCD predicts that glueballs, particles composed of bound states of gluons should exist. The WA102 experiment is designed to study final states formed in the glue-rich double Pomeron exchange interaction $\mathrm{pp} \longrightarrow \mathrm{p_f}(\mathrm{X}^0)\mathrm{p_s}$, where the subscripts f and s refer to the fastest and slowest particles in the laboratory respectively, and X^0 refers to the central system. This interaction has been predicted to be a good source of glueballs. The WA102 experiment ran for 100 days of data-taking in 1996, resulting in 30 868 events of the type $\mathrm{X}^0 \longrightarrow \mathrm{K}^+\mathrm{K}^-$ after all cuts.

This thesis presents the extraction of the $\mathrm{K}^+\mathrm{K}^-$ channel, the results of a partial wave analysis on the 1996 $\mathrm{K}^+\mathrm{K}^-$ data, and a simple fit to the partial waves. It is found that the mass spectrum is composed of $\sim$80% S-wave and $\sim$10% D_0-wave, with no other statistically significant partial waves contributing. The mass spectrum contains in its S-wave resonances compatible with the $\mathrm{f}_0(980)$, $\mathrm{f}_0(1500)$, and $\theta/\mathrm{f_J}(1710)$; and in its D_0-wave resonances compatible with the $\mathrm{f}_2(1270)/\mathrm{a}_2(1320)$, $\mathrm{f}_2'(1525)$, and $\mathrm{f}_2(2150)$. Thus the $\mathrm{K}^+\mathrm{K}^-$ S-wave contains the two glueball candidates, the $\mathrm{f}_0(1500)$ and the $\theta/\mathrm{f_J}(1710)$.

A key aim of this analysis was to measure the spin of the $\theta/\mathrm{f_J}(1710)$, as this undetermined quantum number has a great significance in the search for the lightest glueball. From a full partial wave analysis it is conclusively found that the $\theta/\mathrm{f_J}(1710)$ is a spin-zero particle, while there is found to be no statistically significant activity in any of the D-waves in the $\theta/\mathrm{f_J}(1710)$ mass region.

Contents

List of Figures

List of Tables

Chapter 1

Introduction

The objective of particle physics is the identification and comprehension of the fundamental constituents of matter, and the forces which cause these particles to interact. The roots of this branch of physics can be traced back to ancient Greece where it is recorded that philosophers pondered the composition of matter. Anaximander of Miletus (*c.* 611–547 B.C.) thought that the primary constituents of the world were four fundamental elements, Earth, Water, Air and Fire, which made all other forms of matter by combining in various proportions.

Particle physics in our modern time is a distillation of the work performed by men and women in many branches of science throughout the ages, and currently exists as a worldwide, internationally coordinated effort concentrated on the understanding of the Universe at its most fundamental level. Although twenty-five centuries have passed since the time of Anaximander of Miletus, it is still believed that everything we observe throughout our lives, in all of its wild variety, is composed of just a handful of elementary components.

Our knowledge of the microscopic arena has deepened in stages. An early pivotal insight into the construction of matter was proposed in 1815 by W. Prout. Based upon the observation that the atomic weights of known elements were almost integer multiples of the atomic weight of hydrogen, he suggested that the elements were composed of a discrete number of atoms of hydrogen. In 1869 the chemists D. Mendeleev and L. Meyer [1] presented empirical evidence supporting the atomic concept with their formulation of the periodic law. The law stated that the properties of elements varied in a periodic manner with their atomic weights, and a periodic table was drawn up to illustrate this postulate. The table possessed gaps, and it was proposed that these gaps should be occupied by elements unknown at that time. The properties of these missing elements were predicted, and all were discovered. In 1904 J.J. Thomson put forward a model of the atom. His 'plum pudding' model consisted of thousands of electrons swarming within an atom, held by a balancing positive charge. The ideas of Thomson had only a brief life-time and were soon replaced by Rutherford's model of the atom. Rutherford's experiments showed that alpha particles mainly passed through matter undisturbed, but that some experienced very large deflections and that some would even be redirected back towards their origin. In 1911 this analysis was published, and it demonstrated that the atom had a small dense charged nucleus containing most of the mass of the atom. The discovery of the neutron in 1932 by J. Chadwick completed the modern picture of the atom.

Since 1932 hundreds of strongly interacting subatomic particles, called *hadrons*, have been discovered. With an increasing number of particles came the observation that patterns of hadrons occurred, and that the hadrons could be grouped according to their characteristics. The resulting groupings, called *multiplets*, could accommodate all of the known particles. The multiplets provided a method of categorisation for the particles, and in addition to this they provided predictive power. In 1962 Gell-Mann predicted the Ω^- particle [2] based upon the knowledge that a multiplet was not complete and had a missing member. He was also able to predict the properties and mass of the Ω^- from the characteristics of the multiplet from which it was missing, and in 1964 the Ω^- was discovered [3]. The existence of multiplets suggests that hadrons may possess sub-structure, and in 1964 Gell-Mann [4] and Zweig [5] independently put forward the *quark model* which postulated that the observed particles were composite objects composed of *quarks*. The quark model provided an explanation for the multiplet grouping of hadrons, and proved highly successful in describing the many known particles.

1.1 Constituents of Matter

Our current knowledge of the fundamental particles of matter is that they are point-like and indivisible. They are spin-half *fermions*, of which there are six *quarks* and six *leptons*, the properties of which are listed in table 1.1. The quarks are fractionally electrically charged objects which feel the strong force, whereas the leptons have integer electrical charge and do not feel the strong force. The force carrying particles are integer spin *bosons* and each of the four forces has one or more particles associated with its propagation. The forces and propagating particles are listed in table 1.2.

Table 1.1: Quarks and leptons.

Particle Class	Charge	Spin	Generations
Quarks	$+\frac{2}{3}$e	$\frac{1}{2}$	u c t
	-$\frac{1}{3}$e	$\frac{1}{2}$	d s b
Leptons	-e	$\frac{1}{2}$	e μ τ
	0	$\frac{1}{2}$	ν_e ν_μ ν_τ

1.2 The Electromagnetic Force

In the mid-nineteenth century Maxwell unified the electric and magnetic forces into electromagnetism. In 1930 the theory was expanded to incorporate special relativ-

Table 1.2: Force carrying particles.

Force	Particle(s)	Spin
Strong	Gluon, g	1
Electromagnetic	Photon, γ	1
Weak	$W^{\pm}$,Z^0	1
Gravitational	Graviton	2

ity and quantum field theory; the resulting relativistically invariant quantum field theory *Quantum ElectroDynamics (QED)* describes how fermions experience force by the absorption or emission of field quanta. The theory demonstrates the mechanism by which a field interacts with matter in an entirely particulate nature *via* the exchange of integer spin bosons. In the case of electromagnetic interactions it is *via* the emission and absorption of photons.

Interactions are represented graphically by Feynman diagrams, an example of which is shown in figure 1.1. These provide an important tool for simplifying the mathematical description of the interaction, while aiding the visualisation of the process. The diagrams are used by drawing an interaction, and following the "Feynman rules" which stipulate that factors must be assigned for the incoming and outgoing fermions, for the propagator, and for the coupling strength at the vertices. This is done in order to be able to find the invariant amplitude corresponding to the interaction depicted by the diagram.

The photon mediates the electromagnetic force, but is itself not electrically charged. For this reason photons cannot interact with one another. From a point electric charge photons are emitted isotropically and radiate away from the source, retaining their isotropic distribution. In addition to this, as the photons do not interact with one another, the number of them passing through a fixed area of space decreases in inverse proportion to the square of the radius from the point charge. These factors result in the Coulomb force and potential exhibiting dependences of the form,

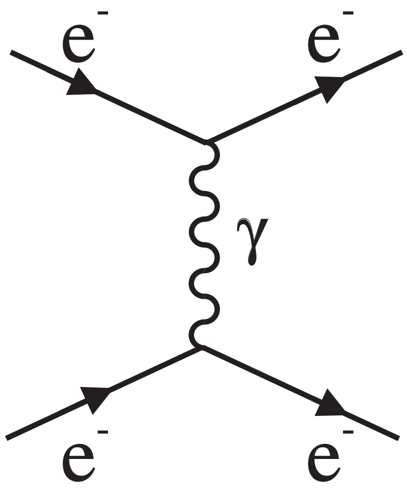

Figure 1.1: The scattering process $e^-e^- \to e^-e^-$. Momentum is transferred between the particles *via* the exchange of a virtual photon.

$$F(R)_{\text{Coulomb}} \propto \frac{1}{R^2}$$

and

$$U(R)_{\text{Coulomb}} \propto \frac{1}{R},$$

where R is the distance from the source.

1.3 The Strong Force

1.3.1 Colour Charge

Quarks and gluons are colour charged particles and hence experience the *strong* (or *colour*) force. Whereas there is only one type of electromagnetic charge the strong force exhibits three different charges, which are equal in magnitude. To distinguish these charges, the three colours red (r), green (g) and blue (b) are used as labels. The colour force is described by the symmetry group $SU(3)_{colour}$, the fundamental representation of which is formed by the colour triplet r, g, b. Quarks are charged with one of the colours while antiquarks are charged with one of the corresponding anticolours, anti-red ($\bar{r}$), anti-green ($\bar{g}$) and anti-blue ($\bar{b}$). Quarks are colour triplets. Gluons have a different configuration of colour charge as each gluon carries one colour and one anticolour. The combination of colour triplet and antitriplet on a gluon decomposes to form octet and singlet representations of the colour group as noted in table 1.3.

Table 1.3: $SU(3)_{colour}$ multiplet representations for the quark and gluon.

Particle	$SU(3)_{colour}$	Decomposition
Quark	3	Triplet
Gluon	$3 \otimes \overline{3} = 8 \oplus 1$	Octet and Singlet

The octet multiplet of gluons are colour charged and mediate the colour force, whereas the singlet gluon state is colourless and therefore cannot. The colour charges of the eight gluons are shown in table 1.4.

1.3.2 Colour Field

The success of QED in describing electromagnetic interactions prompted attempts to describe strong interactions in a similar manner, and an analogous theory to QED emerged, called *Quantum ChromoDynamics (QCD)*. A simple physical difference exists between the electromagnetic and strong forces which has far-reaching conse-

Table 1.4: Colour charges carried by the eight gluons.

Representation	Colour Charge
Octet	$\mathrm{r\overline{g}}$
	$\mathrm{r\overline{b}}$
	$\mathrm{g\overline{r}}$
	$\mathrm{g\overline{b}}$
	$\mathrm{b\overline{r}}$
	$\mathrm{b\overline{g}}$
	$\frac{1}{\sqrt{2}}\left(\mathrm{r\overline{r}} - \mathrm{g\overline{g}}\right)$
	$\frac{1}{\sqrt{6}}\left(\mathrm{r\overline{r}} + \mathrm{g\overline{g}} - 2\mathrm{b\overline{b}}\right)$

quences. The difference is that whereas the mediator of the electromagnetic force is itself not electrically charged, the mediator of the strong force is colour charged, and this enables gluons to interact with one another. This means that the colour field connecting two quarks can interact with itself *en route* between the quarks, collimating the colour field between the quarks into what can be described as a tube, or string, of coloured flux. This collimation has the consequence that the strong force does not weaken with distance, but maintains the same strength connecting the two quarks regardless of their distance from one another. The electromagnetic and strong fields are shown in figures 1.2a and 1.2b respectively.

This completely alters the behaviour of the strong force in comparison with the electromagnetic force, and leads to the strong force and potential exhibiting dependences of the form,

$$\mathrm{F(R)_{colour}} \;\propto\; \frac{\alpha_{\mathrm{s}}}{\mathrm{R}^2} \;+\; \sigma,$$

and,

$$\mathrm{U(R)_{colour}} \;\propto\; \frac{\alpha_{\mathrm{s}}}{\mathrm{R}} \;+\; \sigma\mathrm{R}.$$

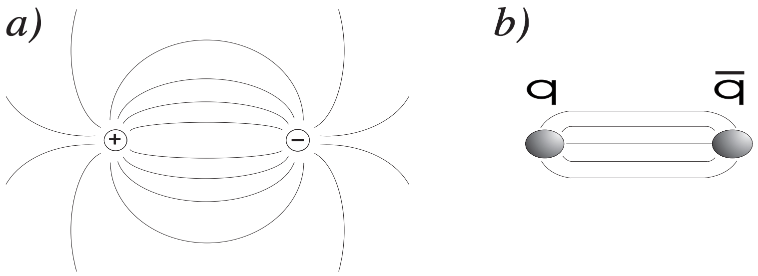

Figure 1.2: Electromagnetic field lines spread out with distance, whereas colour field lines are collimated making the strength of the force essentially independent of distance.

R is the distance from the source, α_s is the strong running coupling constant, and σ is the string tension of the colour field.

The $\frac{1}{R^2}$ contribution to the strong force is due to single gluons travelling between the quarks independently; this is akin to the familiar Coulomb potential due to the exchange of single photons. The contribution to the strong force that is independent of R is due to the collimated field, and it is independent of R as the same number of field lines connect the quark and antiquark regardless of their separation.

1.3.3 Colour Confinement

If two quarks in a bound system are moving apart, the potential between them rises linearly with distance, forming an increasing energy barrier against separation with distance. This rising potential is sufficient to maintain a bound system of quarks if they are undisturbed by external forces. In the situation where the quarks are moving apart with enough energy, there will come a point when the potential developed between them is great enough to create a new quark-antiquark pair from

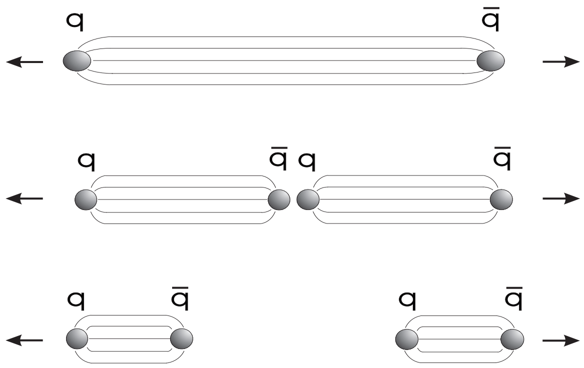

Figure 1.3: As two colour connected quarks move apart the colour potential may increase to the point where a new $q\overline{q}$ pair is created from the vacuum.

the vacuum (as depicted in figure 1.3), which preserves the closure of the colour field. This behaviour of the strong force ensures that colour charged particles and the colour field can never be observed outside of a colourless composite object, the phenomenon is called *infrared slavery*, or *colour confinement*.

Colour confinement ensures that strongly interacting particles must be an $SU(3)_{colour}$ singlets for them to exist as isolated objects. Colour singlets are unchanged by rotations in r, g, b colour space and possess no net colour charge. They are the only colour representation which can be physically manifested.

1.4 Strongly Bound Particles

The quark model postulates that hadrons are composed of quarks, of which only two configurations are required. One configuration is three quarks (qqq), or anti-quarks ($\overline{qqq}$), which are $\frac{1}{2}$-integer spin *baryons*, or *antibaryons*, respectively. The second configuration is $q\overline{q}$ pairs which are integer spin *mesons*.

Table 1.5: The quark combinations of both baryons and mesons produce the colour singlets necessary for physical states. The internal colour configurations composing the overall colourless singlet state are also shown.

	Multiplets	Internal Colour of Singlet State
Baryon	$3 \otimes 3 \otimes 3 = 10 \oplus 8 \oplus 8 \oplus 1$	$\frac{1}{\sqrt{6}}$ { (bg-gb)r + (rb-br)g + (gr-rg)b }
Meson	$3 \otimes \overline{3} = 8 \oplus 1$	$\frac{1}{\sqrt{3}}\ (\mathrm{r\overline{r}+g\overline{g}+b\overline{b}})$

1.4.1 Colour Singlets

A quark configuration which is proposed to describe real particles must be able to provide a colour singlet state, and it is known if this is possible from the quark constituents of the hadron. Baryons are composed of three colour triplet quarks, the decomposition of which leads to a decuplet, two octets, and one singlet state. The same is true for antibaryon states. Mesons are composed of a triplet and an antitriplet, the decomposition of which yields octet and singlet states. Table 1.5 summarises the hadronic decompositions and also shows the internal colour content of the singlet states for both types of hadron. It can be seen that the quark configurations proposed by the quark model both produce the colour singlet state required for physical particles.

1.4.2 Flavour Multiplets

The quark components of light hadrons are combinations of the three light quark flavours, up (u), down (d) and strange (s). This introduces a three-fold nature, which makes SU(3) symmetry not only appropriate to describe the quarks, but also an appropriate way of classifying the hadron states into their groups of multiplets. In an analogous manner to $\mathrm{SU(3)_{colour}}$, $\mathrm{SU(3)_{flavour}}$ predicts that the baryons have decuplet, octet and singlet multiplets; and that the mesons have octet and singlet multiplets (which are grouped together as nonets). Flavour is not confined in the same way as colour and so particles with a 'net flavour' can exist as physical particles.

Unlike $SU(3)_{\text{colour}}$, $SU(3)_{\text{flavour}}$ is not an exact symmetry. A feature of this is that particles with identical quantum numbers mix to produce the physically observed states. This occurs in meson nonets, in which the two physical isoscalar particles are a mixture of their pure $SU(3)_{\text{flavour}}$ singlet and octet states. Typically, mixing produces almost a complete separation between the $\frac{1}{\sqrt{2}}(\mathrm{u\bar{u}} + \mathrm{d\bar{d}})$ and $\mathrm{s\bar{s}}$ quarks in the physical particles, which is called *ideal* (or *magic*) mixing.

1.5 Meson Nonets

A typical nonet is the ground state vector nonet in which the ϕ and ω mesons are almost pure $\mathrm{s\bar{s}}$ and $\frac{1}{\sqrt{2}}(\mathrm{u\bar{u}} + \mathrm{d\bar{d}})$ respectively. The nonet, shown in figure 1.4, consists of an isodoublet state (the $K^{\star}$), an isovector state (the ρ), and two isosinglet states (the ϕ and ω).

The quarks forming the mesons are spin-half objects which results in the intrinsic spin (S) of a meson being either 0 or 1 relating to the spin configurations $\frac{1}{\sqrt{2}}(\uparrow\downarrow + \downarrow\uparrow)$ and $\frac{1}{\sqrt{2}}(\uparrow\uparrow + \downarrow\downarrow)$ respectively. The total spin (J) of the meson is then the vector sum of its intrinsic spin and the relative orbital angular momentum (L) between the quark and antiquark pair. The parity of a meson is given by,

$$\mathrm{P} = \eta(-1)^{\mathrm{L}},$$

where $\eta = -1$ for a quark-antiquark pair, as they have opposite intrinsic parity. A neutral $\mathrm{q\bar{q}}$ system is an eigenstate of the charge conjugation operator C, which for a $\mathrm{q\bar{q}}$ pair is given by,

$$\mathrm{C} = (-1)^{\mathrm{L+S}}.$$

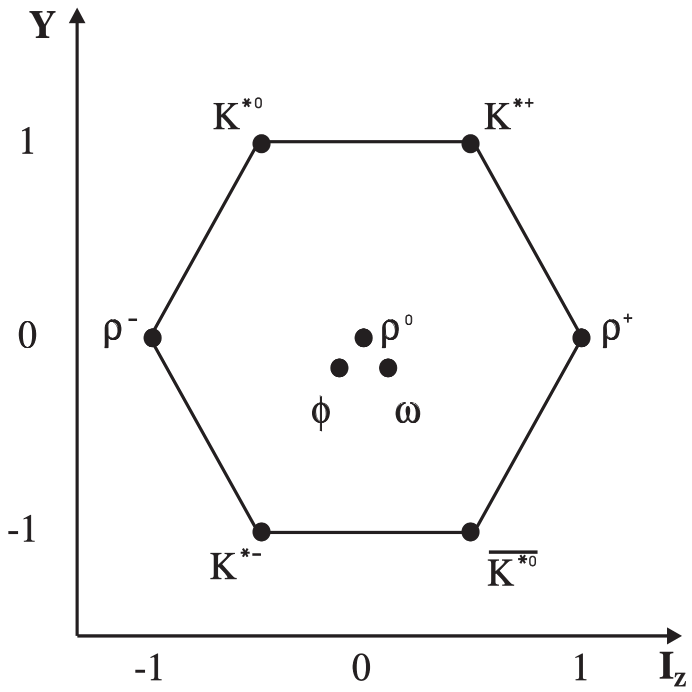

Figure 1.4: The ground state vector nonet.

The resulting J^{PC} quantum numbers identify the nonet.

The quark model has been highly successful in its description of the known strongly interacting particles. However, QCD tells us that the quark model does not provide a complete picture. Arising from the phenomenon of colour confinement, and the fact that the strong force is mediated by coloured propagators, QCD predicts that unusual states of matter should exist which are neither qqq nor $q\overline{q}$. Such states are beyond the quark model.

Chapter 2

Glueballs and Exotic States

2.1 Introduction

The field theory Quantum ChromoDynamics (QCD) describes all strong interactions in terms of originating from interactions between quarks, which are mediated by the quanta of the colour field, the gluons. The gluons are themselves colour charged, which allow them to interact with one another and to bind together into systems called *glueballs*. Colour singlet states are a viable outcome from these gluonic systems, which leads to the expectation that they can be physically manifested. These states are neither qqq nor $q\overline{q}$ and are beyond the quark model. To observe their existence experimentally would substantiate an important prediction of QCD.

2.2 Beyond the Quark Model

Particles beyond the quark model predicted by QCD include

- **Glueballs.** These gluonic mesons contain no valence quarks, but consist of two (gg), three (ggg), or more valence gluons. They are the only possible case of a bound state of force carriers, and a rich spectrum of glueballs is predicted.

- **Hybrids.** These are composed of a quark, antiquark and gluon ($q\overline{q}g$).

Other particles beyond the quark model allowed by QCD include multiquark states such as 4-quark ($q\overline{q}q\overline{q}$) and pentaquark ($qqqq\overline{q}$) states.

2.3 Physics on the Lattice

Hadrons exist in a regime where the strong coupling constant α_s is too large for the application of perturbative QCD calculations. The best methods presently available for simulating hadronic systems are computational ones collectively called *Lattice QCD*. Lattice QCD calculations are performed on a four-dimensional lattice which is used to represent a discretised space-time, within which quarks and gluons are placed.

In lattice QCD calculations particle masses are first calculated as mass ratios, $m/\sqrt{\sigma}$, where σ is the string tension. These quantities are later converted to physical mass units. The mass ratios for a particle are calculated at various finite lattice spacings, a, and these measurements allow an extrapolation to the continuum limit to be performed. Once the mass ratio has been evaluated in the continuum limit, it is then converted to physical mass units.

The introduction of the physical mass scale requires the string tension to be incorporated, the calculation of which can be performed in two ways. It can be inferred from Regge slopes that $\sqrt{\sigma} \approx 400 - 450$ MeV. An alternative method is to calculate the mass ratio of a well measured particle, such as the ρ, on the lattice to obtain a continuum limit value for $m_\rho/\sqrt{\sigma}$. Then by substituting in the experimentally determined mass of the ρ meson, the value of $\sqrt{\sigma}$ can be found. Two independent lattice QCD groups produce consistent values for the mass ratio $m_\rho/\sqrt{\sigma}$, and using a ρ mass of $m_\rho = 770$ MeV/c^2, this yields a value of $\sqrt{\sigma} = 440 \pm 15_{\mathrm{stat.}} \pm 35_{\mathrm{sys.}}$ MeV [6].

The light $q\overline{q}$ mesons have been calculated [7], in part to assess the quality of the lattice glueball calculations. Eleven light hadron masses were calculated on the lattice. Three of these hadrons (the π, K and ρ mesons) were used to set the physical mass scale and the remaining eight masses were predictions. Predictions for the $K^\star(892)$, $\phi(1020)$, N, $\Xi + \Sigma - N$, $\Delta(1232)$, $\Sigma^\star(1385)$, $\Xi^\star(1530)$ and Ω were made and the biggest disagreement with experiment was 6%. This demonstrates that the $q\overline{q}$ spectrum obtained in this way is a good approximation to the physical light $q\overline{q}$ spectrum, it also adds justification to the expectation that the lattice QCD calculations for the masses of glueballs will be of a similar accuracy.

Analyses from independent lattice QCD groups give compatible results for the mass of the lightest scalar glueball. The compatibility is demonstrated by the mass estimates below, and is illustrated in figure 2.1. Figure 2.1 shows calculations of the ground state scalar glueball mass by IBM research (represented by the the symbol $\times$) and other lattice QCD groups (represented by the the symbol $\bullet$). The calculations are at various finite lattice spacings, a, and an extrapolation to the continuum limit ($a \rightarrow 0$) is shown [11].

UKQCD [8]	$m_{0^{++}} = 1568 \pm 89$ MeV/c^2,
IBM [9]	$m_{0^{++}} = 1648 \pm 58$ MeV/c^2,
Morningstar and Peardon [10]	$m_{0^{++}} = 1630 \pm 100$ MeV/c^2.

The masses for glueballs of J^{PC} values 0^{++}, 2^{++} and 0^{-+} have been calculated at several different lattice spacings, allowing reliable extrapolations to the continuum limit with mass errors of typically $\lesssim \mathcal{O}(150$ MeV). The masses of the ground state 2^{++} and 0^{-+} glueballs in the continuum limit from a fit to the available global data are,

$$m_{0^{-+}} = 2190 \pm 260_{\text{stat}} \pm 180_{\text{sys}}\ \text{MeV}/c^2\ [6],$$
$$m_{2^{++}} = 2260 \pm 120_{\text{stat}} \pm 180_{\text{sys}}\ \text{MeV}/c^2\ [6],$$

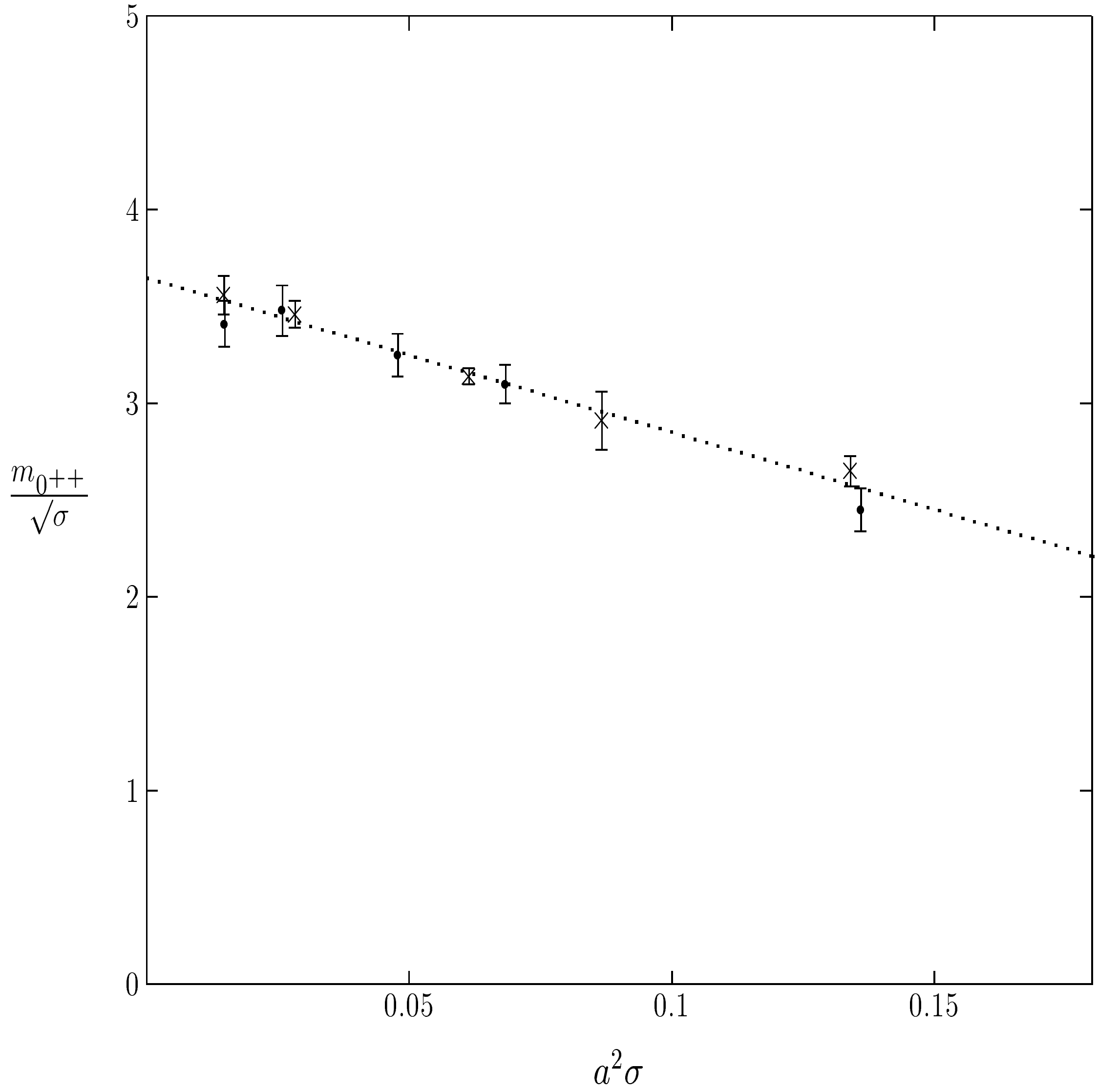

Figure 2.1: Ground state scalar glueball mass calculations performed by IBM research ($\times$), and other lattice QCD groups ($\bullet$), at various finite lattice spacings with an extrapolation to the continuum limit shown [11]. The results produced by the different research groups are compatible.

and the masses of the first excited 2^{++} and 0^{-+} states in the continuum limit are,

$$\mathrm{m}_{0^{-+}} = 2960 \pm 10_{\mathrm{stat}} \pm 140_{\mathrm{sys}}\ \mathrm{MeV}/c^2\ [10],$$
$$\mathrm{m}_{2^{++}} = 3320 \pm 20_{\mathrm{stat}} \pm 160_{\mathrm{sys}}\ \mathrm{MeV}/c^2\ [10].$$

Glueballs other than those listed have not been as thoroughly studied, and consequently cannot be reliably extrapolated to the continuum limit. However, mass calculations for these states at finite lattice spacings indicate that they will be yet higher in mass than the 0^{++}, 0^{-+}, and 2^{++} glueballs [12].

A further result from lattice QCD is an estimation of the width of the glueball. A calculation made by the IBM research group of the width of the lightest scalar glueball decaying to all possible pseudoscalar pairs [13] yields $\Gamma = 108 \pm 29$ MeV/c^2. It is reported that this width, combined with any reasonable guesses for the effects of finite lattice spacing and the remaining width to multibody states, produces a total width small enough for the lightest scalar glueball to be a clearly discernible peak in experiment. Before this estimation, it was a possibility that glueballs could be extremely wide objects, and therefore effectively experimentally unobservable.

2.4 Glueball Production Mechanisms

Much of hadron spectroscopy has been performed using peripheral interactions which are dominated by Reggeon or quark exchange and are not thought to provide good environments for the creation of glueballs. Only production mechanisms which generate *glue-rich* regions are considered to be good sources of gluonic states, and are shown in figure 2.2.

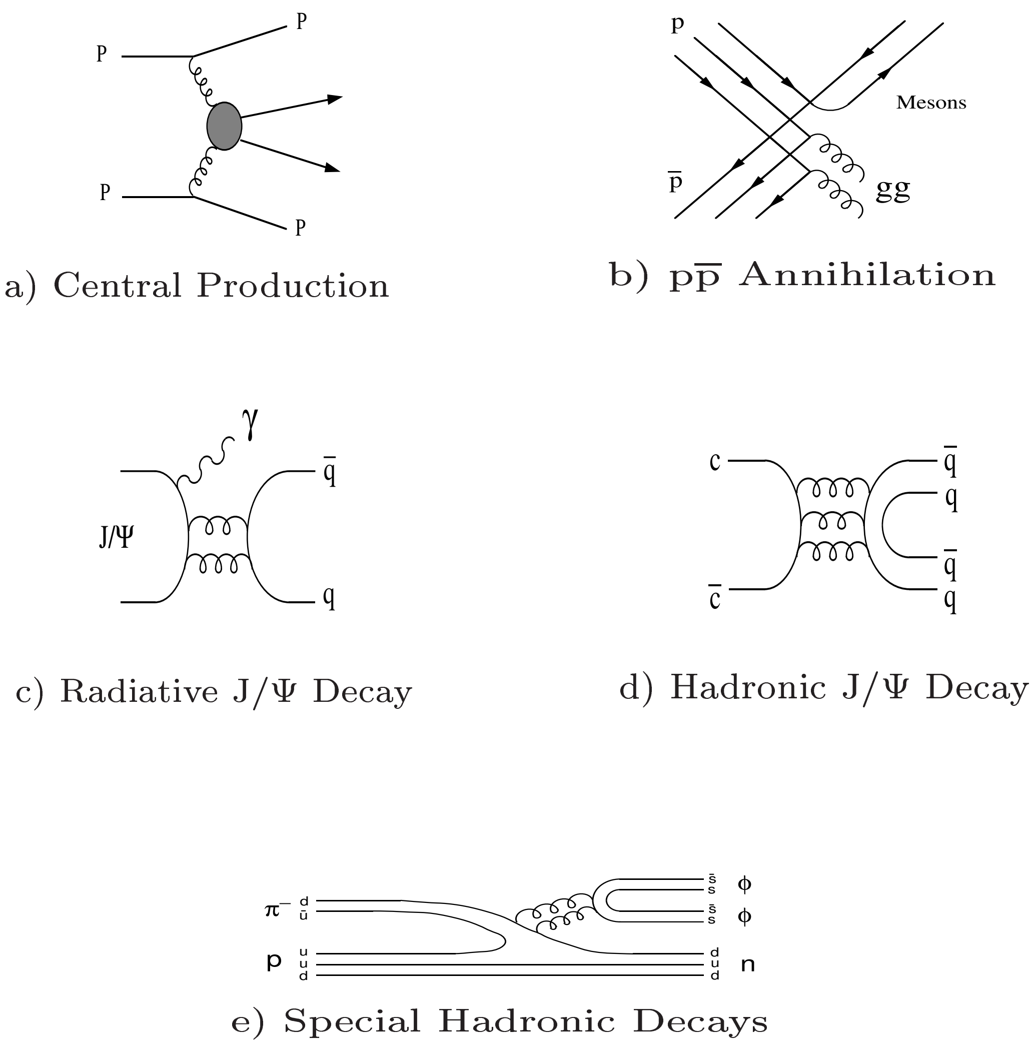

Figure 2.2: Production mechanisms predicted to create glue-rich environments.

2.4.1 Central Production

Central production (figure 2.2a) is a double exchange process in which the initiating beam and target leave the interaction region practically undisturbed, such that the central system is almost at rest in the overall centre-of-mass frame. It is predicted to proceed *via* double Pomeron exchange (DPE) at high centre-of-mass energies ($\sqrt{s}$) and low four-momentum transfers ($|t|$) [14] (the significance of the kinematical region is explained in more detail in section 2.7). The Pomeron is believed to be a colourless multi-gluonic object and for this reason the creation of a central system *via* Pomeron-Pomeron fusion is predicted to be a good source of gluonic states [15, 16]. The Reggeon and Pomeron are discussed in more detail in section 2.6. Although other double exchange processes such as Pomeron-Reggeon and Reggeon-Reggeon are also known to be present, it is believed that Pomeron-Pomeron fusion is an important exchange in the kinematical region used in such experiments. Section 2.8 contains supporting evidence for this claim with regard to the WA102 experiment.

2.4.2 $\overline{\text{p}}$p Annihilation

In the $\overline{\text{p}}$p annihilation process (figure 2.2b) quarks mutually annihilate, generating gluons. This provides a glue-rich region in which gluonic states should be favourably produced.

2.4.3 J/ψ Decays

The J/ψ is a bound state consisting of a charm and an anticharm quark (c$\overline{\text{c}}$). It has a mass of 3097 MeV/c^2 and is not massive enough to decay with connected quark-lines, as the lightest charmed meson has a mass of 1865 MeV/c^2. This restriction forces the J/ψ to decay *via* c$\overline{\text{c}}$ annihilation, either by its radiative decay mode (figure 2.2c), or its hadronic decay mode (figure 2.2d). Both decay modes are glue-rich as gluons are generated from the annihilation of quarks.

2.4.4 Special Hadronic Decays

Special hadronic decays that involve disconnected quark-lines are also considered to be glue-rich mechanisms as they are OZI violating [5, 17]. These decays are expected to be mediated by the annihilation of quark and antiquark into gluons, thereby creating a glue-rich region. A decay which has an OZI violating mode, shown in figure 2.2e, is $\pi^- \mathrm{p} \to \mathrm{n}\phi\phi$. The ϕ meson is an almost pure strange-antistrange ($\mathrm{s\overline{s}}$) state, and so for the decay to proceed disconnected quark-lines are likely[1] to be involved.

2.5 Identification of Non-$\mathrm{q\overline{q}}$ States

2.5.1 Exotic Quantum Numbers

A clear-cut signal for physics beyond the quark model would be to find a state with $\mathrm{J^{PC}}$ quantum numbers that a $\mathrm{q\overline{q}}$ meson cannot possess. One so-called *oddball* $\mathrm{J^{PC}}$ configuration is $\mathrm{J^{PC}} = 1^{-+}$. The lightest 1^{-+} state is predicted to be a hybrid particle (the composition of which is $\mathrm{q\overline{q}g}$), and a number of experiments have reported observations of a 1^{-+} signal in $\pi\eta$ systems. The VES collaboration see evidence for 1^{-+} resonant structures in peripheral π^-Be interactions in both $\pi\eta$ and $\pi\eta'$ systems [19]. A high statistics study at Brookhaven by the E852 collaboration finds a resonance decaying to $\pi\eta$ that is compatible with the VES result in their π^-p peripheral interactions [20]. The parameters for the state are,

$$\begin{aligned} \mathrm{m}_{1^{-+}} &= 1370 \pm 16_{\,\mathrm{stat.}}{}^{+\,50}_{-\,30}{}_{\,\mathrm{sys.}}\ \mathrm{MeV}/c^2, \\ \Gamma_{1^{-+}} &= 385 \pm 40_{\,\mathrm{stat.}}{}^{+\,65}_{-105}{}_{\,\mathrm{sys.}}\ \mathrm{MeV}/c^2. \end{aligned}$$

[1] It has been established [18] that it is also possible for this decay to proceed with connected quark-lines *via* a radially excited η or η'.

The Crystal Barrel collaboration also see evidence for resonant behaviour in their $\pi\eta$ system [21] resulting from $\overline{\mathrm{p}}$d interactions proceeding *via* $\overline{\mathrm{p}}$n annihilation. The resonance parameters found were,

$$\begin{aligned} \mathrm{m}_{1^{-+}} = &\quad 1400 \pm 20_{\ \mathrm{stat.}} \pm 20_{\ \mathrm{sys.}}\,\mathrm{MeV}/c^2, \\ \Gamma_{1^{-+}} = &\quad 310 \pm 50_{\ \mathrm{stat.}}\ {}^{+\ 50}_{-\ 30}{}_{\ \mathrm{sys.}}\,\mathrm{MeV}/c^2. \end{aligned}$$

2.5.2 Glueball Characteristics

Most glueballs are predicted to possess $\mathrm{J^{PC}}$ quantum numbers that conventional $\mathrm{q\overline{q}}$ mesons can also have, which precludes the 'clear-cut' identification possible for oddball states. In addition to this, the lightest glueball states are predicted by lattice QCD to not only possess the same $\mathrm{J^{PC}}$ quantum numbers, but also to exist in the same mass region, and to have properties which are not markedly different from normal $\mathrm{q\overline{q}}$ nonet members. In spite of this glueball characteristics have been predicted, and are searched for in an attempt to locate non-$\mathrm{q\overline{q}}$ states.

Over-Full Nonets

An important method for locating states beyond the quark-model is to find nonets with a surplus of members, and to subsequently identify the non-$\mathrm{q\overline{q}}$ member(s). If an over-full nonet is found then the members can be subjected to particular scrutiny, and identification of the non-$\mathrm{q\overline{q}}$ member is attempted by looking for the traits and characteristics expected of glueball behaviour.

Glue-Rich Production Mechanisms

If a particular state is found produced in various different glue-rich processes and is either not produced or heavily suppressed in normal hadronic interactions, then this is immediate evidence that the state can be considered a glueball candidate, and that its identity should be investigated further.

Radiative J/ψ Decay Widths

The radiative decay of the J/ψ state is now very well defined theoretically [22]. This makes it the only glue-rich production mechanism for which the glueball content of a state X, resulting from the decay J/ψ $\rightarrow$ γ(X), can be quantitatively defined.

Coupling Strength to $\gamma\gamma$

Gluons carry no electric charge and so do not directly couple to photons. For this reason the process,

$$\gamma\gamma \longrightarrow \mathrm{G},$$

is suppressed by a factor of $\sim\frac{1}{\alpha_{\mathrm{S}}^2}$ with respect to the process,

$$\gamma\gamma \longrightarrow \mathrm{M},$$

where G is a glueball and M is a $\mathrm{q\overline{q}}$ meson. For this reason glueballs will be suppressed in $\gamma\gamma$ fusion experiments. Experiments of this type measure the production cross-sections, and hence partial widths, of particles and compare them to values for established $\mathrm{q\overline{q}}$ mesons. This contributes further evidence regarding the gluonic content of a particle.

Flavour Dependence

Glueballs are flavour singlets, and for this reason the naive expectation is that they should couple to final states irrespective of their flavour[2], *i.e.* in a *flavour-blind* manner. A modification to the flavour-blind picture is that glueballs should couple strongly to $\eta\eta$, $\eta\eta'$ and $\eta'\eta'$ channels because of the predicted high gluonic content of the η and η' [23].

It is currently thought that mixing between $q\overline{q}$ states and the lightest scalar glueball will take place, and this complicates the flavour dependence of glueball decays. Although the flavour dependence of the decays is still considered to hold relevant information about the identity of a glueball candidate its interpretation is no longer straightforward, and varies between different mixing scenarios.

dP_T Dependence

In central production the quantity dP_T has been defined by the WA102 collaboration as the difference in transverse momentum between the two exchanged particles in a double exchange process, such that,

$$dP_T = \sqrt{(P_{y1} - P_{y2})^2 + (P_{z1} - P_{z2})^2}.$$

It has been empirically observed that dP_T can be used as an effective glueball/$q\overline{q}$ meson filter [24, 25, 26]. At low dP_T ($<0{\cdot}3$ GeV/c) the production of all of the glueball candidates observed by the WA102 collaboration are enhanced, while the production of the established $q\overline{q}$ states are suppressed. Conversely, at high dP_T ($>0{\cdot}5$ GeV/c) the glueball candidates are found to be suppressed, while the established $q\overline{q}$ mesons are enhanced. In contrast to the predicted glueball characteristics, this is a new and unexpected phenomenon and is not yet fully understood. It seems

[2] After phase-space considerations have been accounted for.

likely, however, that as its effectiveness as a glueball/$q\overline{q}$ filter has been proven, it will continue to yield important information in the identification of glueballs.

2.6 Regge and Pomerančuk Trajectories

When studying hadron-hadron interactions at low momentum transfers the strong coupling constant, α_s, becomes too large for a perturbative expansion of QCD to be appropriate. Instead, a phenomenological description of peripheral interactions has been built up based on Regge theory, and has proved very successful.

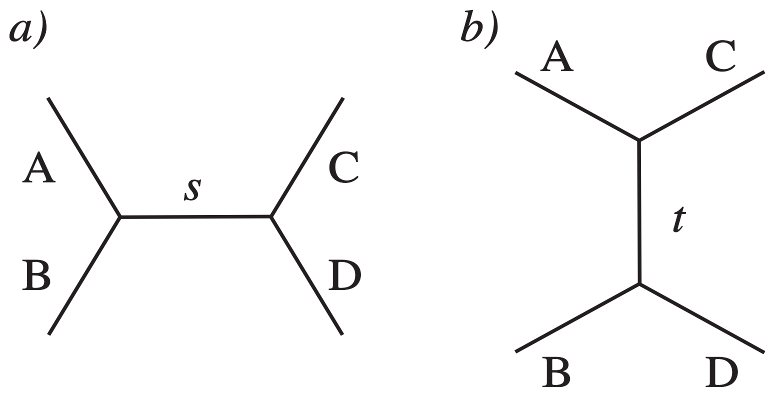

Figure 2.3: Scattering *via* (a) s-channel and (b) t-channel exchanges.

Regge theory is a generalisation of the Yukawa model in that it describes scattering interactions in terms of the exchange of mesons, generically called Reggeons ($\mathbb{R}$). It is convenient to describe these scattering processes in terms of the Lorentz invariant kinematical variables s and t. These Mandelstam variables are defined as,

$$s = (p_A + p_B)^2 = (p_C + p_D)^2,$$

$$t = (p_A - p_C)^2 = (p_B - p_D)^2,$$

where $p_{\rm A}$, $p_{\rm B}$, $p_{\rm C}$, and $p_{\rm D}$ are the 4-momenta of the particles A, B, C, and D respectively, shown in figure 2.3.

Hadronic scattering can either be viewed as an s-channel process as depicted in figure 2.3a, or a t-channel process as depicted in figure 2.3b, and are mediated by real and virtual hadrons respectively. Regge theory uses a t-channel picture of scattering, and if the exchanged Reggeons are viewed on a Chew-Frautschi plot, *i.e.* in the angular momentum (J) *vs.* mass squared ($\mathrm{m}^2 = t$) plane, then in general they lie on a linear *Regge trajectory* which can be expressed as,

$$\alpha(t) \;=\; \alpha(0) + \alpha' t.$$

If a Regge trajectory is extrapolated to physical (integer) J values, it is found that the corresponding mass values are those of the physical mesons believed to be involved in the exchange. The points at which the physical particles are manifested are called the *poles* of the trajectory.

The interpretation of Regge theory at high centre-of-mass energies originally caused problems. It was observed (see figure 2.4) that if only known mesons are considered then the total cross-sections of pp and $\overline{\mathrm{p}}$p interactions ceased to fall as predicted by Regge theory, but became essentially constant, rising only very slowly with s. None of the known mesons could be used to describe the observed cross-sections, and Pomerančuk [27] introduced the idea of a *vacuum exchange* called the *Pomeron* ($\mathbb{P}$) [28], which has proven to be a successful and necessary addition to Regge theory.

Donnachie and Landshoff [29, 30] have produced fits to the total cross-sections for $\overline{\mathrm{p}}$p and pp scattering for centre-of-mass energies ranging from $\sqrt{s} \sim 5$ GeV to $\sqrt{s} \sim 2000$ GeV using a linear sum of the Regge and Pomerančuk amplitudes [30]. The trajectory intercepts from the fits were found to be,

$$\alpha_{\mathbb{P}}(0) = 1.0808,$$
$$\alpha_{\mathbb{R}}(0) = 0.5475.$$

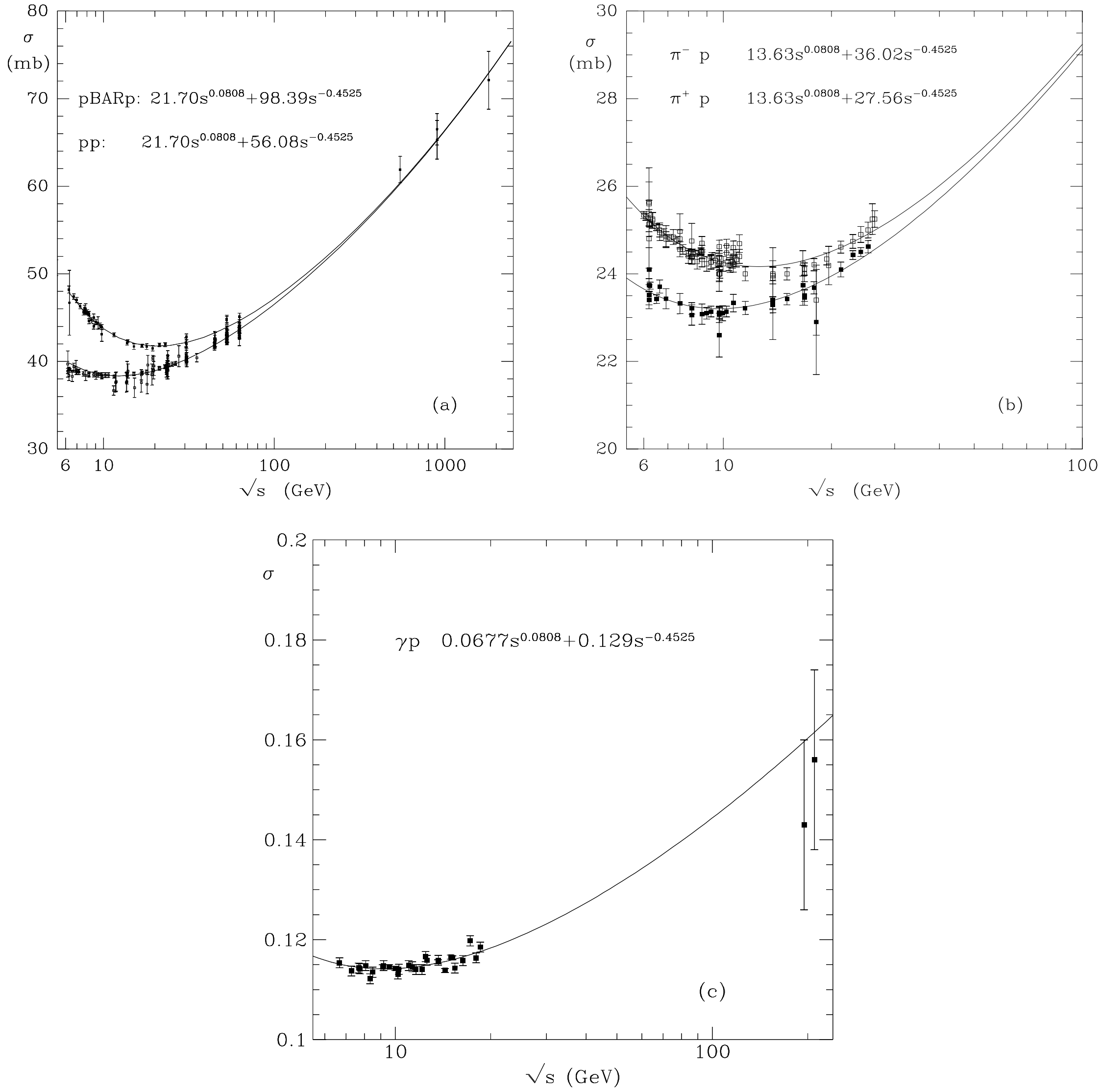

Figure 2.4: Total cross-sections for (a) pp and $\overline{\text{p}}$p scattering, (b) π^-p and π^+p scattering and (c) γp scattering. The solid lines are the Donnachie-Landshoff fits.

In Regge theory total cross-sections are expected to behave as,

$$\sigma_{\rm tot} \propto s^{\alpha(0)-1},$$

where if the parameters above are used it can be seen that the total cross-section dependences on centre-of-mass energy vary approximately as,

$$\begin{aligned}\sigma_{I\!P} &\propto \sqrt{s}^{\;0},\\ \sigma_{I\!R} &\propto \sqrt{s}^{\;-1}.\end{aligned}$$

The interpretation of low momentum transfer scattering being due to the exchange of t-channel states implies that in addition to the Reggeon, the Pomeron can be considered as a distinct entity. It is assumed that the Pomeron trajectory is associated with multiple gluon exchange [31]. This is an assumption supported by the observation of high p_T jets in diffractive $\overline{p}p$ interactions [32] which indicate a partonic structure, and by data taken by the H1 collaboration [33] which is compatible with a Pomeron valence structure consisting of a simple gluon pair. If it is the case that the Pomeron is a multi-gluonic object, then the poles might be expected to have valence gluon structures, such as those predicted for the glueball.

2.7 Double Pomeron Exchange

Double Pomeron Exchange (DPE) proceeds *via* Pomeron-Pomeron ($I\!PI\!P$) fusion. In addition to this process there are expected to be contributions from other double exchange mechanisms, such as Pomeron-Reggeon ($I\!PI\!R$) and Reggeon-Reggeon ($I\!RI\!R$) exchanges. To maximise the proportion of glue-rich $I\!PI\!P$ interactions with respect to the other interactions, experiments using this mechanism must attempt to use the optimal kinematic regions for the process.

2.7.1 s-Dependence of DPE

From the energy dependences of the single exchanges, the energy dependences for the three possible double exchanges are found to be,

$$\sigma_{\mathbb{PP}} \propto \sqrt{s}^{\,0},$$
$$\sigma_{\mathbb{PR}} \propto \sqrt{s}^{\,-1},$$
$$\sigma_{\mathbb{RR}} \propto \sqrt{s}^{\,-2}.$$

It is seen that Reggeon exchange dominates at low $\sqrt{s}$ but diminishes at higher $\sqrt{s}$ values, where it is superseded by Pomeron exchange. For an experiment to successfully use DPE as a mechanism for the production of glueballs, it must operate at an energy where the proportion of $\mathbb{PP}$ interactions are large enough to provide a sufficient DPE signal-to-background ratio.

2.7.2 t-Dependence of DPE

For a fixed Feynman x, defined as,

$$x_{\mathrm{F}} = \frac{p_{\mathrm{L}}}{p_{\mathrm{Lmax.}}},$$

where $\mathrm{p_L}$ and $\mathrm{p_{Lmax.}}$ are the actual and maximum longitudinal momenta available for a particle respectively, the DPE signal-to-background ratio varies approximately as $e^{-\alpha|t|}$ [14]. Hence DPE becomes dominant as $|t|$ tends to zero.

2.8 DPE in the WA102 Experiment

It is important to gauge the significance of $\mathbb{PP}$ interactions as compared with the $\mathbb{PR}$ and $\mathbb{RR}$ interactions for a particular experiment. Although the DPE signal-to-background ratio cannot be quantitatively ascertained, evidence for a good DPE signal-to-background ratio is available.

The relative strengths of the Pomeron and Reggeon exchanges at the energy used by the WA102 experiment ($\sqrt{s} = 29{\cdot}1$ GeV) can be estimated from figure 2.4. At this energy it can be seen that the total cross-section is rising, indicating that Pomeron exchange is a significant mechanism at this point.

A more direct source of evidence comes from the data gathered from the predecessor central production experiments to WA102, which have taken data using beams at different momenta. Data with beams at 85 GeV/c, 300 GeV/c and 450 GeV/c have been taken, corresponding to centre-of-mass energies of 12·7 GeV, 23·8 GeV and 29·1 GeV respectively. Isospin conservation allows DPE to produce only $I = 0$ states, therefore the production of other isospin states is an indicator that $\mathbb{P}\mathbb{R}$ and/or $\mathbb{R}\mathbb{R}$ must be occurring.

The effective $\pi^+\pi^-$ mass spectrum from the interaction,

$$\mathrm{pp} \longrightarrow \mathrm{p_f}(\pi^+\pi^-)\mathrm{p_s},$$

taken with a beam energy of 85 GeV/c is shown in figure 2.5a, in which the $\rho(770)$ is prominent. The mass spectrum from the same interaction, but with an increased beam energy of 450 GeV/c, is shown in figure 2.5b. In comparison with the lower energy data the resonance is heavily suppressed, and as the $I = 1$ $\rho(770)$ resonance cannot be produced by DPE this indicates an increased level of DPE interactions with respect to $\mathbb{P}\mathbb{R}$ and/or $\mathbb{R}\mathbb{R}$ interactions at the higher centre-of-mass energy.

A similar criterion can be applied to examine the prediction for the $|t|$ dependence of DPE behaviour by comparing different $|t|$ regions of data taken with a constant beam energy of 450 GeV/c. Shown in figures 2.5c and 2.5d are the $\pi^+\pi^-$ effective mass spectra for the regions $|t| < 0{\cdot}3$ GeV^2 and $|t| > 0{\cdot}3$ GeV^2 respectively. The suppression of the $\rho(770)$ in the low $|t|$ sample confirms the prediction that DPE is more dominant at low $|t|$.

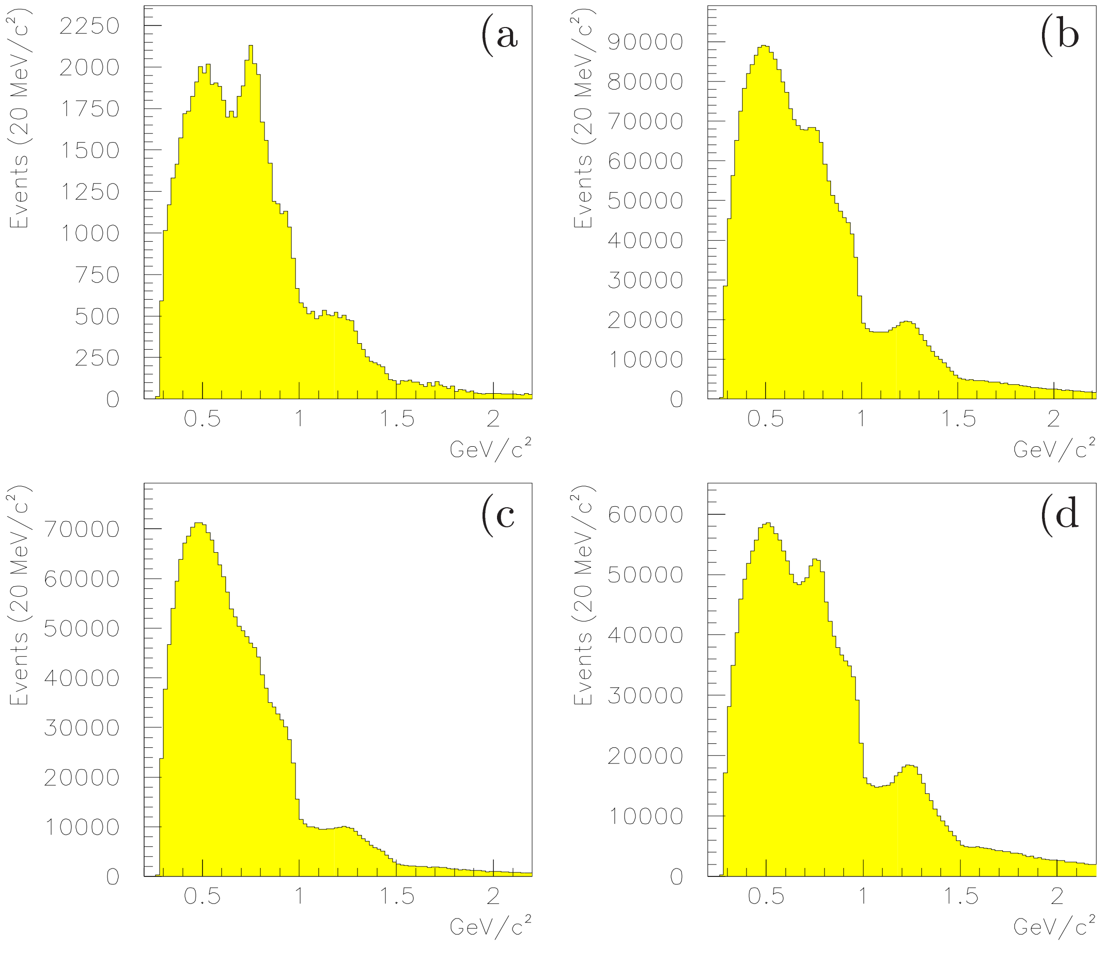

Figure 2.5: Effective $\pi^+\pi^-$ mass spectra. Shown for (a) $\sqrt{s}$ = 12·7 GeV, (b) $\sqrt{s}$ = 29·1 GeV; and at the higher centre-of-mass energy for (c) $|t|$<0·3 GeV^2, and (d) $|t|$>0·3 GeV^2.

2.9 Summary

The highly successful theory Quantum ChromoDynamics (QCD) predicts new and unusual forms of matter, a prime example of which are glueballs. Glueballs are difficult to produce as they require specific glue-rich mechanisms to be created, and difficult to identify as their masses and properties are expected to be similar to those of normal $q\overline{q}$ mesons. The search for glueballs is further hindered by the inapplicability of perturbative QCD techniques to the low momentum regime of hadronic resonances.

The search for glueballs is performed by experiments using glue-rich production mechanisms in order to study glueball candidates and the surrounding $q\overline{q}$ meson environment. Theoretical calculations of the QCD governing glueballs cannot be performed; however, the search is aided by computational simulations of QCD which use lattices created by supercomputers to predict the masses of the glueballs, which allow particular mass regions to be focussed upon by experiments. When either likely mass regions or potential glueball candidates have been found, glueball characteristics are looked for in order to assess the possible gluonic nature of any relevant particles. Theoretical developments in the radiative decays of vector mesons now allow quantitative predictions to be made of the partial widths of glueballs and $q\overline{q}$ mesons from such decays. The production rates of resonances in $\gamma\gamma$ fusion interactions, in which glueballs should be suppressed, provide further information by which to assess the gluonium nature of a particle. The new phenomenon of the kinematical glueball/$q\overline{q}$ filter is a further technique used in the assessment of the gluonic nature of a particle.

The attention directed towards the discovery of glueballs has resulted in considerable clarification of the experimental situation. This has been achieved by dedicated glueball searches taking high statistics data which has been used to develop a better understanding of the $q\overline{q}$ nonet compositions, in the vicinity of which the lightest glueball is expected to exist, and by isolating and testing the glueball characteristics of glueball candidates.

Chapter 3

The Ground State 0^{++} Nonet and Glueball

3.1 Introduction

Predictions for the mass of the lightest scalar glueball from the lattice QCD community have converged at a range of 1500 MeV/c^2 to 1700 MeV/c^2. This places it close to the ground state scalar $q\overline{q}$ nonet, which has attracted special attention to the scalar states in this mass region. High statistics data have been taken by dedicated glueball experiments in recent years in an effort to explore this mass region. In contributing towards the identification of the scalar glueball the work has proved essential, as analyses of the data have revealed the new scalar particles $f_0(1370)$, $a_0(1450)$ and the glueball candidate $f_0(1500)$. Knowledge of these new states is crucial for a more complete understanding of the 0^{++} nonet, close to which the glueball lies. Equally important are increased data sets on the glueball candidate $\theta/f_J(1710)$, to allow a reliable spin analysis to be performed to clarify the spin of the particle.

This chapter first reviews the status of the 0^{++} nonet in section 3.2, which is followed by a short discussion of the two scalar glueball candidates in section 3.3. The spin of the $\theta/f_J(1710)$ has not yet been determined as analyses throughout the years have produced conflicting results for the quantum number, and a primary objective of this thesis is to add clarification to this situation by presenting a reliable spin analysis of the $\theta/f_J(1710)$ using data from the WA102 experiment. The results from significant experiments on the spin of the $\theta/f_J(1710)$ are summarised in section 3.4, and the consequences of the two potential outcomes are then briefly reported on in sections 3.4.1 and 3.4.2. The experimental observations of the two glueball candidates are then presented in section 3.5 for the $f_0(1500)$, and in section 3.6 for the $\theta/f_J(1710)$. Finally, the likely situation of three-state mixing between the isoscalars is discussed in section 3.7, and the chapter is summarised in section 3.8.

3.2 The 0^{++} Nonet

Before 1994 the 0^{++} nonet was thought to include the $K_0^\star(1430)$, $a_0(980)$, and $f_0(980)$, this composition however was never very satisfactory. One immediate reason was that the mass differences between the components were unusual in comparison with the mass differences between members of other nonets. In addition to this, the $a_0(980)$ and $f_0(980)$ exhibit behaviour not expected from the isovector and isoscalar members of the 0^{++} nonet, based upon their strong coupling to $K\overline{K}$ final states and small $\gamma\gamma$ partial widths [34].

With the exception of the $K_0^\star(1430)$, the perceived composition of the nonet has evolved as further information about its candidate states has become available. The discoveries of the new scalar states, the $f_0(1370)$ [35], $a_0(1450)$ [36] and $f_0(1500)$ [37], have demanded a re-evaluation of the nonet. It is no longer thought that the $a_0(980)$ and $f_0(980)$ states are part of the nonet, and it has been proposed [34] that a natural explanation for their properties is provided by a $K\overline{K}$ molecule interpretation. The composition that the 0^{++} nonet is now thought to possess is shown in table 3.1. The nonet currently has a satisfactory association of particles to nonet positions, with the exception of the $s\bar{s}$ member. There are candidates for the $s\bar{s}$ member of the nonet, and it will be described in this chapter how the arguments for the identification

Table 3.1: Current particle assignments to the 0^{++} nonet.

Nonet position	Particle Assignment
Isodoublet	$K_0^\star(1430)$
Isovector	$a_0(1450)$
Isosinglet – $\{\frac{1}{\sqrt{2}}(u\overline{u}+d\overline{d})\}$	$f_0(1370)$
Isosinglet – $\{s\overline{s}\}$	UNDETERMINED

of the scalar glueball, for the $s\overline{s}$ member, and for the spin of the $\theta/f_J(1710)$ are somewhat entwined.

3.3 Glueball Candidates — The $f_0(1500)$ and $\theta/f_J(1710)$

The $f_0(1500)$ and $\theta/f_J(1710)$ resonances both display clear glueball characteristics, and are good glueball candidates. They are both seen in glue-rich production mechanisms, and are either not seen, or are heavily suppressed in normal hadronic interactions. In addition to this, the $\theta/f_J(1710)$ is clearly seen decaying to $K\overline{K}$ final states and therefore couples to strange quarks, and yet it is not produced in K^-p interactions [40]. Figure 3.1 compares data from the glue-rich interaction $J/\psi \longrightarrow \gamma(K_S^0K_S^0)$ from Mark III [41], with data from the peripheral hadronic interaction $K^-p \longrightarrow K_S^0K_S^0\Lambda$ from LASS, normalised to the $f_2'(1525)$ peaks. The absence of the $\theta/f_J(1710)$ from the K^-p interaction is apparent. Both the $f_0(1500)$ and the $\theta/f_J(1710)$ are in the appropriate mass range for the lightest scalar glueball predicted by lattice QCD. Both states are also suppressed in $\gamma\gamma$ interactions. A measurement of the production of a state in $\gamma\gamma$ fusion interactions allows the *stickiness* [42] of a state to be calculated, where stickiness is a measure of the gluonic nature of a particle. The stickiness of a particle X is defined as the partial width of the decay

$J/\psi \longrightarrow \gamma(X)$ divided by partial width of the decay $X \longrightarrow \gamma\gamma$, which is proportional to the production cross-section of the interaction $\gamma\gamma \longrightarrow X$. The stickiness for the undisputed $q\overline{q}$ meson $f_2(1270)$ is set to one, and the stickiness for other particles are normalised to this. A recent measurement [43] of the suppression of the $f_0(1500)$ in $\gamma\gamma$ interactions gives a lower limit for the stickiness of the particle of ~13, this is in contrast to the expected stickiness of a conventional $q\overline{q}$ meson which is ~1.

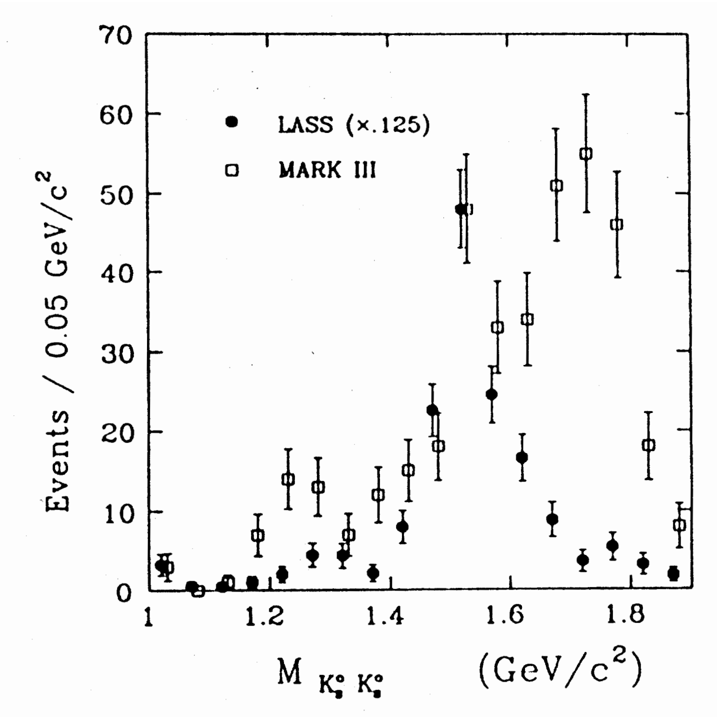

Figure 3.1: A comparison of $K^0_S K^0_S$ effective mass spectra produced in peripheral interactions by the LASS experiment, and in radiative J/ψ decays by the Mark III experiment. The $\theta/f_J(1710)$ is produced in the glue-rich production mechanism, but is absent in the peripheral one. Figure from reference [40].

The partial width of the decay $J/\psi \longrightarrow \gamma(X)$ also holds information about the gluonic nature of a particle. The partial width of the decay $J/\psi \longrightarrow \gamma(f_0(1500))$ indicates [22] that it is probably produced at too high a rate to be a $q\overline{q}$ state. Although the experimental situation for the width requires some clarification, the world average of data suggests that the $f_0(1500)$ is a glueball-$q\overline{q}$ mixture. The gluonic nature of the $\theta/f_J(1710)$ as indicated by the width of the decay $J/\psi \longrightarrow \gamma(\theta/f_J(1710))$ is interesting, as this is the only glueball characteristic of the $\theta/f_J(1710)$ which depends on its spin. If the $\theta/f_J(1710)$ is spin-zero, then it is produced at a rate which is too high for it to be a $q\overline{q}$ state, but is consistent with it being a glueball or mixed glueball-$q\overline{q}$ state having a large glueball component. If, however, it is spin-two then its partial width in radiative J/ψ decays would suggest that the $\theta/f_J(1710)$ is consistent with being a $q\overline{q}$ particle.

To summarise, the $f_0(1500)$ and $\theta/f_J(1710)$ both display the characteristics expected of glueball behaviour. The $f_0(1500)$ is a good scalar glueball candidate, and the candidacy of the $\theta/f_J(1710)$ for the scalar glueball depends only upon its spin.

3.4 The Spin of the $\theta/f_J(1710)$

The $\theta/f_J(1710)$ was discovered in radiative J/ψ decays in 1982, and since its discovery its spin has remained a matter of uncertainty. The particle is observed decaying to $\eta\eta$ in radiative J/ψ decays, and to two identical bosons in the process $\theta/f_J(1710) \longrightarrow K^0_S K^0_S$; this means that it must have $J^{PC} = \text{even}^{++}$. A spin of zero or two is expected, as $J \geqslant 4$ is unlikely for a particle of mass <2 GeV/c^2. Early analyses by several experiments including the Crystal Ball, MARK II, MARK III, and WA76, favoured spin-two for the particle. Later, reports by Mark III, and the results from a re-analysis of Mark III data by Bugg *et al.* find a dominantly spin-zero contribution in the $\theta/f_J(1710)$ region. A more recent analysis of $J/\psi \longrightarrow \gamma(K^+K^-)$ by the BES group, finds the $\theta/f_J(1710)$ region to be dominated by a spin-two amplitude.

The spin of the $\theta/f_J(1710)$ is arguably the most significant measurement still to be made in order to identify the scalar glueball, as the implications of the alternative possible spin values are very different.

3.4.1 The $\theta/f_{J=0}(1710)$

If the $\theta/f_J(1710)$ is found be spin-zero, then both the $f_0(1500)$ and $\theta/f_{J=0}(1710)$ are good candidates for the scalar glueball. Furthermore, they are the only two states which are compatible with being the ground state scalar glueball. In this situation the simplest interpretation is that one of the states is the $s\bar{s}$ nonet member, and the other is the scalar glueball[1].

3.4.2 The $\theta/f_{J=2}(1710)$

If the $\theta/f_J(1710)$ is found to be spin-two, then it can be excluded from the discussion of the 0^{++} sector and the $f_0(1500)$ would stand unchallenged as the scalar glueball.

The $\theta/f_{J=2}(1710)$ would be too low in mass to be consistent with lattice QCD predictions for the ground state tensor glueball, and as its partial width in $J/\psi \longrightarrow \gamma(\theta/f_{J=2}(1710))$ decays would be consistent with a $q\bar{q}$ member [22], it could possibly be interpreted as a member of a radially or orbitally excited tensor nonet. However, the glueball characteristics exhibited by the state would still require explanation. One difficulty with the $\theta/f_{J=2}(1710)$ scenario is that it implies that there is a mainly $s\bar{s}$ 0^{++} nonet member lying in the 1600 MeV/c^2 region [44] which has not yet been observed.

3.5 Experimental Observations of the $f_0(1500)$

3.5.1 The GAMS-4000 Collaboration

The first published observation of the $f_0(1500)$ was by the GAMS collaboration in 1983 [37]. They reported an unusual resonance, dubbed the G(1590), with quantum

[1] Although mixing between the isoscalar scalars will complicate this picture. See section 3.7.

numbers $J^{PC} = 0^{++}$, which preferentially decayed into $\eta\eta$ and $\eta\eta'$. GAMS confirmed the state in a further investigation of $\eta\eta$ systems produced in the interactions,

$$\begin{array}{llll} \pi^- \mathrm{p} & \longrightarrow & (\eta\eta)\mathrm{N} & \text{at 100 GeV}/c \text{ [45]}, \\ \pi^- \mathrm{N} & \longrightarrow & (\eta\eta)\pi^- \mathrm{N} & \text{at 300 GeV}/c \text{ [46]}. \end{array}$$

Since this first sighting of the state it has been confirmed by several experiments.

3.5.2 The WA102 Collaboration

In 1989 the WA76 collaboration published evidence [47] for a new enhancement in the centrally produced $\pi^+\pi^-\pi^+\pi^-$ system with the parameters,

$$\begin{aligned} \mathrm{m}_{\mathrm{X}_0(1450)} &= 1449 \pm 4 \ \mathrm{MeV}/c^2, \\ \Gamma_{\mathrm{X}_0(1450)} &= 78 \pm 18 \ \mathrm{MeV}/c^2, \end{aligned}$$

which subsequent publications have confirmed [49, 50]. The $\pi^+\pi^-\pi^+\pi^-$ effective mass spectrum is shown in figure 3.2, in which the resonances $\mathrm{f}_1(1285)$, $\mathrm{X}_0(1450)$, and $\mathrm{X}_2(1900)$ are the three prominent peaks. The WA102 collaboration have performed a more recent analysis of the centrally produced $\pi^+\pi^-\pi^+\pi^-$ system using improved statistics [48] and showed that if the peak at 1450 MeV/c^2 is fitted with a single Breit-Wigner, its parameters are found to be,

$$\begin{aligned} \mathrm{m}_{\mathrm{X}_0(1450)} &= 1445 \pm 4 \ \mathrm{MeV}/c^2, \\ \Gamma_{\mathrm{X}_0(1450)} &= 95 \pm 15 \ \mathrm{MeV}/c^2. \end{aligned}$$

A new scalar state was also found in the centrally produced $\pi^+\pi^-$ channel by the WA76 collaboration [49] in 1991. The combined WA76 and WA91 $\pi^+\pi^-$ mass spectrum is shown in figure 3.3a. To fit the high mass part above the $\mathrm{f}_2(1270)$,

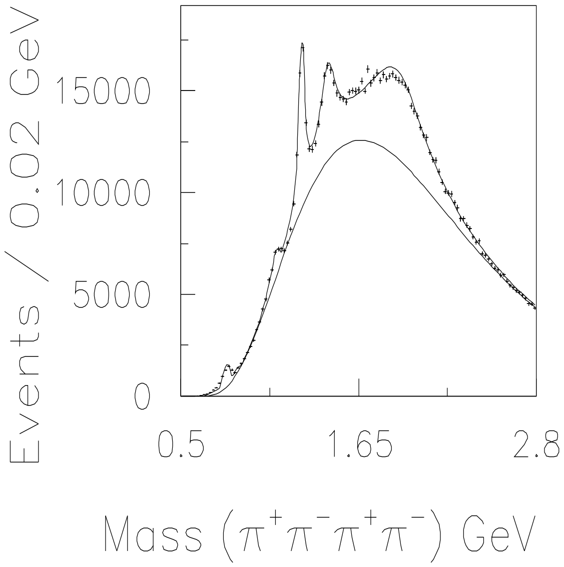

Figure 3.2: The WA102 collaboration's $\pi^+\pi^-\pi^+\pi^-$ effective mass spectrum from the interaction $pp \longrightarrow p_f(\pi^+\pi^-\pi^+\pi^-)p_s$. The main peaks are the $f_1(1285)$ and the new enhancements $X_0(1450)$ and $X_2(1900)$. Figure from reference [48].

a new Breit-Wigner interfering with the background was required. The fit with the new resonance is shown in figure 3.3b. If instead the $X_0(1450)$ is used to fit the region the description of the data is clearly worse, as is shown in figure 3.3c. The parameters for the new Breit-Wigner were found to be,

$$\begin{aligned} m_{f_0(1500)} &= 1472 \pm 12 \text{ MeV}/c^2, \\ \Gamma_{f_0(1500)} &= 195 \pm 33 \text{ MeV}/c^2. \end{aligned}$$

This observation was confirmed in 1995 [51] with parameters of,

$$\begin{aligned} m_{f_0(1500)} &= 1497 \pm 30 \text{ MeV}/c^2, \\ \Gamma_{f_0(1500)} &= 199 \pm 30 \text{ MeV}/c^2. \end{aligned}$$

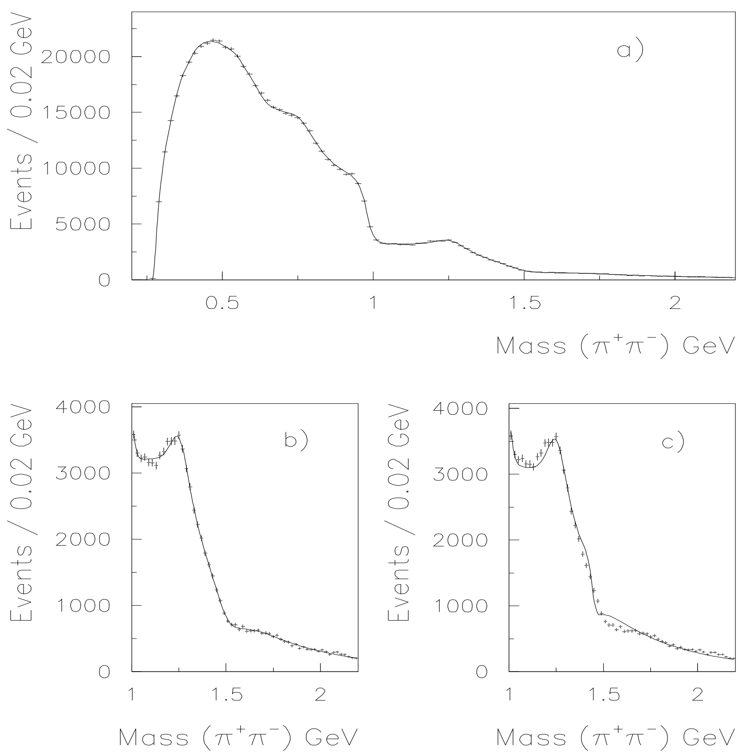

Figure 3.3: (a) The combined WA76 and WA91 $\pi^+\pi^-$ effective mass spectrum from the interaction pp $\longrightarrow$ $p_f(\pi^+\pi^-)p_s$. The area above the $f_2(1270)$ can be fitted with either (b) the new $f_0(1500)$ state or (c) the $X_0(1450)$. The new state clearly provides a better fit to the data. Figure from reference [51].

Possible reasons for the mass difference between these two new scalar states was investigated and analyses by the WA91 [51] and WA102 [48] collaborations proposed the hypothesis that the $X_0(1450)$ could be the result of interference between the $f_0(1370)$ and $f_0(1500)$ states seen by other experiments. To investigate this possibility a fit was performed to the dominant decay mode of the $X_0(1450)$ ($\rho\rho$ in the 0^+ wave), allowing interference between the $f_0(1370)$ and $f_0(1500)$. The result of the fit describes the data well, and the parameters obtained from this fit are,

$$\begin{aligned} m_{f_0(1370)} &= 1290 \pm 15 \text{ MeV}/c^2, \\ \Gamma_{f_0(1370)} &= 290 \pm 30 \text{ MeV}/c^2, \end{aligned}$$

and,

$$\begin{aligned} m_{f_0(1500)} &= 1510 \pm 20 \text{ MeV}/c^2, \\ \Gamma_{f_0(1500)} &= 120 \pm 35 \text{ MeV}/c^2, \end{aligned}$$

These parameters are consistent with those found for the $f_0(1370)$ and $f_0(1500)$ by other experiments.

A possible problem with the interference interpretation is that the $X_0(1450)$ decays dominantly to $\rho\rho$, whereas other analyses in $\overline{p}p$ annihilation [52] and radiative J/ψ decay [53] find a dominant decay mode for the $f_0(1500)$ of $\sigma\sigma$, where σ denotes the broad $\pi\pi$ S-wave enhancement with a maximum at ~800 MeV/c^2. To investigate this, a Monte Carlo simulation was used in which the $f_0(1370)$ was made to decay equally to $\sigma\sigma$ and $\rho\rho$, and the $f_0(1500)$ was made to decay solely to $\sigma\sigma$. The results from this show that it is possible to extract a result of pure $\rho\rho$ for the decay of the $X_0(1450)$, as is observed in the experimental data.

The new state has subsequently been confirmed as the $f_0(1500)$. The interference between the $f_0(1370)$ and $f_0(1500)$ which affects the $\pi^+\pi^-\pi^+\pi^-$ channel, is not apparent in the $\pi^+\pi^-$ case as the $f_0(1370)$ is not observed decaying to $\pi^+\pi^-$ in central production.

3.5.3 The Crystal Barrel Collaboration

The Crystal Barrel collaboration have taken high statistics data, the majority of which are on neutral final state interactions, and have been able to perform a thorough analysis of the $f_0(1500)$ decaying to several final states.

The Crystal Barrel collaboration first published an observation of the $f_0(1500)$ in 1994 [35] in a simultaneous analysis of the interactions $\overline{p}p \longrightarrow \pi^0(\pi^0\pi^0)$ and

$\overline{\mathrm{p}}\mathrm{p} \longrightarrow \pi^0(\eta\eta)$, where the $\mathrm{f}_0(1500)$ decays to $\pi^0\pi^0$ and $\eta\eta$ respectively. The parameters for the $\mathrm{f}_0(1500)$ are found to be,

$$\begin{aligned} \mathrm{m}_{\mathrm{f}_0(1500)} &= 1520 \pm 25 \ \mathrm{MeV}/c^2, \\ \Gamma_{\mathrm{f}_0(1500)} &= 148 \begin{smallmatrix} +\ 20 \\ -\ 25 \end{smallmatrix} \ \mathrm{MeV}/c^2. \end{aligned}$$

Since this initial observation the Crystal Barrel collaboration has also found evidence for the state in the decay channels $\pi^0(\pi^0\eta)$ [36], $\pi^0(\eta\eta')$ [54], high statistics $\pi^0(\pi^0\pi^0)$ data [55], high statistics $\pi^0(\eta\eta)$ data [56], $\pi^0(\pi^0\pi^0\pi^0\pi^0)$ [52] and $\pi^0(\mathrm{K}^0_\mathrm{L}\mathrm{K}^0_\mathrm{L})$ [57]. The $\pi^0\pi^0$ mass spectrum from the high statistics $\pi^0(\pi^0\pi^0)$ data is shown in figure 3.4. The fit requires contributions from the $\mathrm{f}_2(1270)$ and $\mathrm{f}_0(1370)$ for the peak at $\sim$1300 MeV/c^2, and contributions from the $\mathrm{f}_0(1500)$ and $\mathrm{f}_2'(1525)$ for the peak at $\sim$1500 MeV/c^2. The $\eta\eta$ mass spectrum from the high statistics $\pi^0(\eta\eta)$ data is shown in figure 3.5, the two peaks are associated with the $\mathrm{f}_0(1370)$ and the $\mathrm{f}_0(1500)$ mesons.

A coupled channel analysis [58] of the $\pi^0(\pi^0\pi^0)$, $\pi^0(\pi^0\eta)$ and $\pi^0(\eta\eta)$ channels produce a mass and width of,

$$\begin{aligned} \mathrm{m}_{\mathrm{f}_0(1500)} &= 1509 \pm 10 \ \mathrm{MeV}/c^2, \\ \Gamma_{\mathrm{f}_0(1500)} &= 116 \pm 17 \ \mathrm{MeV}/c^2, \end{aligned}$$

while an average mass evaluated from the Crystal Barrel's eight data sets gives,

$$\begin{aligned} \mathrm{m}_{\mathrm{f}_0(1500)} &= 1500 \pm 8 \ \mathrm{MeV}/c^2, \\ \Gamma_{\mathrm{f}_0(1500)} &= 132 \pm 15 \ \mathrm{MeV}/c^2. \end{aligned}$$

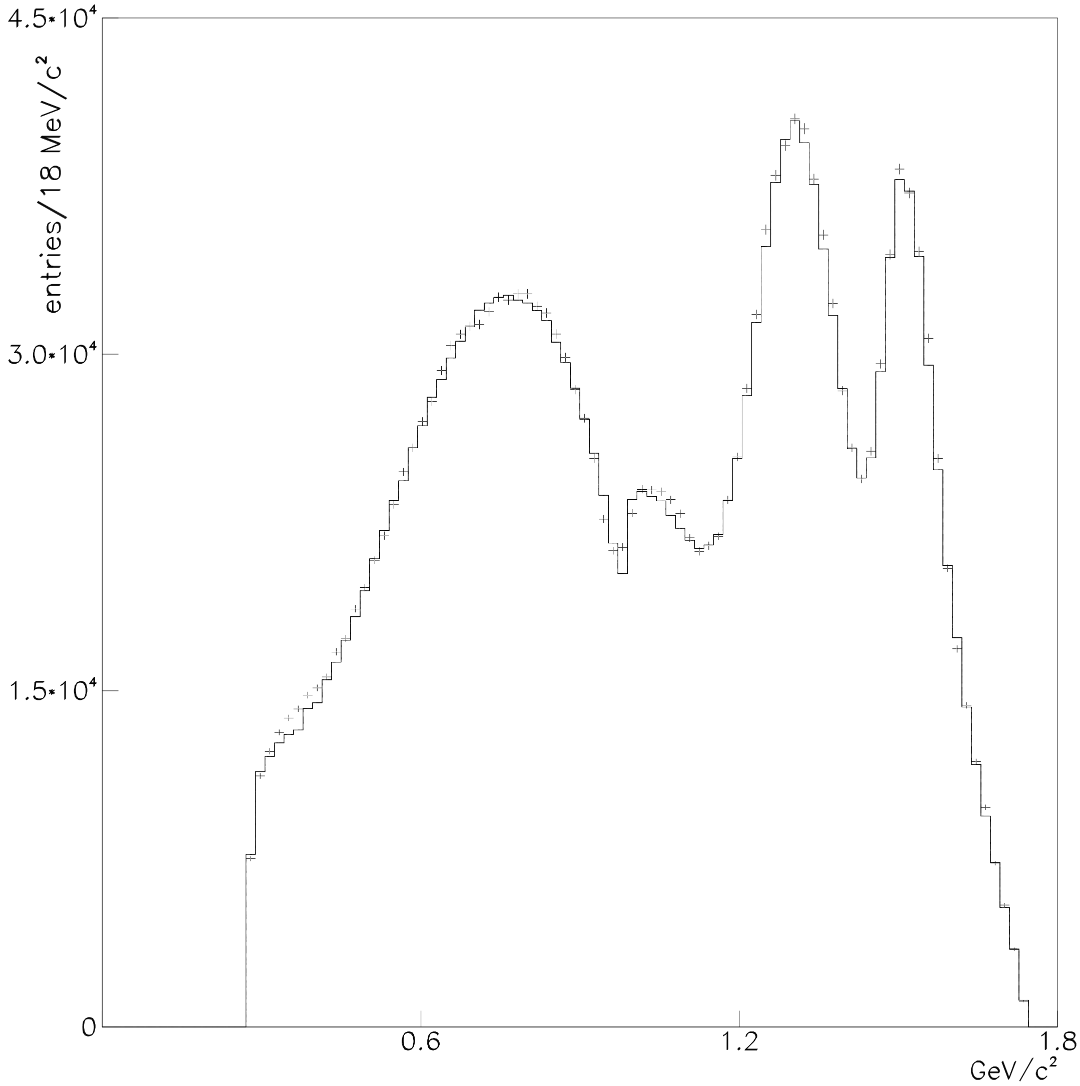

Figure 3.4: The Crystal Barrel collaboration's $\pi^0\pi^0$ effective mass spectrum from the interaction $\overline{\mathrm{p}}\mathrm{p} \longrightarrow \pi^0(\pi^0\pi^0)$. The $\mathrm{f}_0(1370)$ and $\mathrm{f}_0(1500)$ contribute to the peaks at $\sim$1300 MeV/c^2 and $\sim$1500 MeV/c^2 respectively. Figure from reference [55].

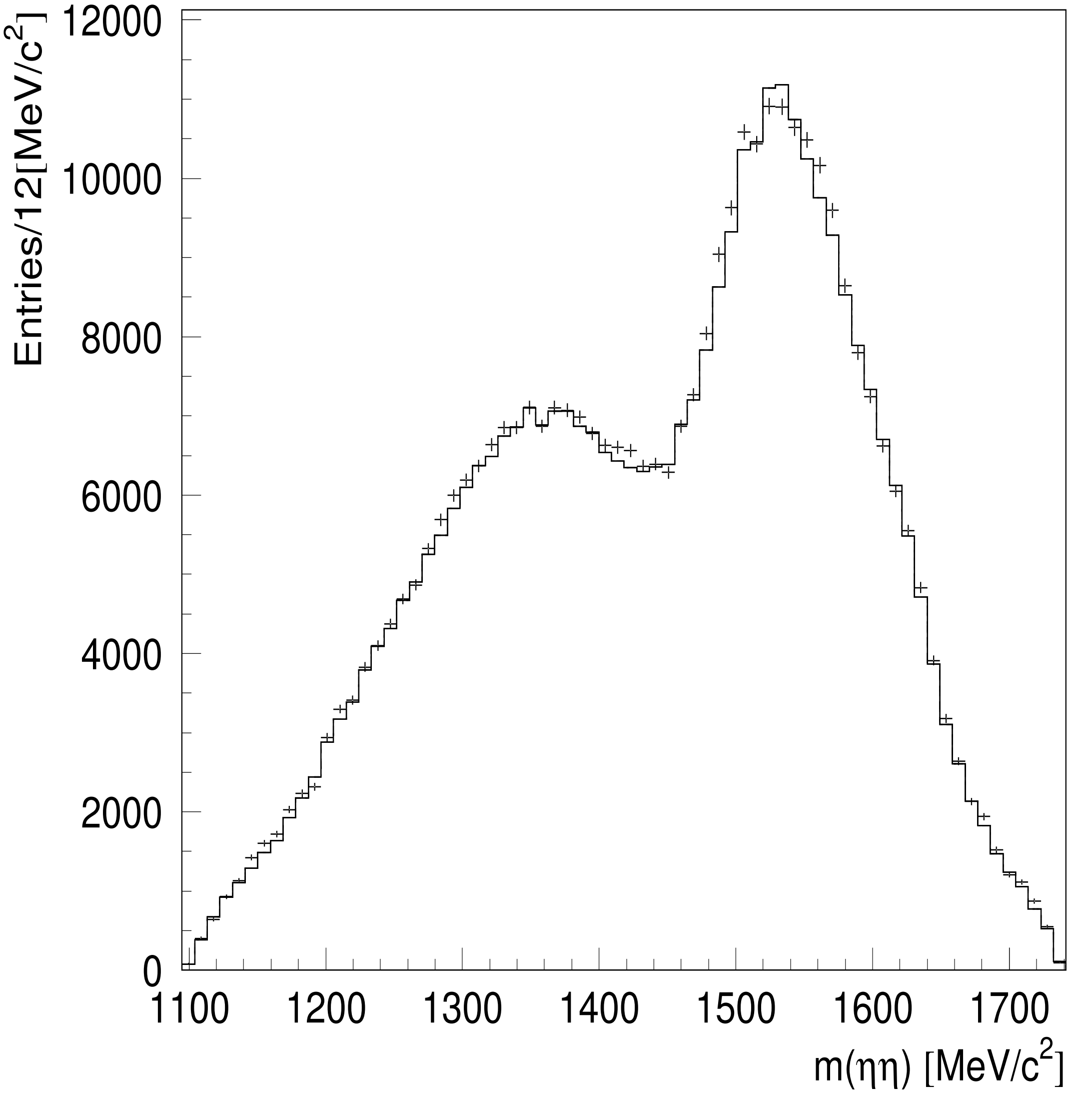

Figure 3.5: The Crystal Barrel collaboration's $\eta\eta$ effective mass spectrum, from the interaction $\overline{\mathrm{p}}\mathrm{p} \longrightarrow \pi^0(\eta\eta)$, clearly shows the $f_0(1370)$ and $f_0(1500)$ states. Figure from reference [56].

3.5.4 The E690 Collaboration

The E690 collaboration have performed a fixed target central production experiment using an 800 GeV/c beam, obtaining central $\mathrm{K^0_S K^0_S}$ systems from the interaction

$$\mathrm{pp} \longrightarrow \mathrm{p_s(K^0_S K^0_S)p_f},$$

where,

$$\mathrm{K^0_S} \longrightarrow \pi^+\pi^-,$$

the mass spectrum from which is shown in figure 3.6. A spin analysis [59] of the data shows that the $\mathrm{K^0_S K^0_S}$ system up to 1·58 GeV/c^2 is produced mainly in the S-wave, and hence the S-wave peak in the ~1·5 GeV/c^2 region is associated with the $\mathrm{f_0}(1500)$. The spin of the $\theta/\mathrm{f_J}(1710)$ has not been determined from this spin analysis as ambiguous solutions between the S-wave and the D-waves occur above a mass of 1·58 GeV/c^2.

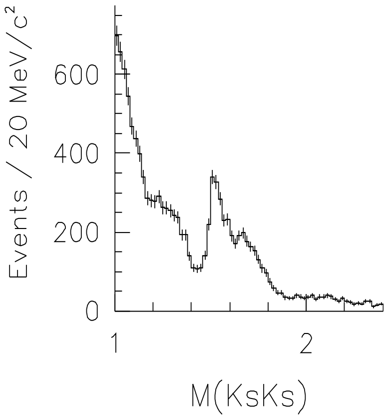

Figure 3.6: The E690 collaboration's centrally produced $\mathrm{K^0_S K^0_S}$ effective mass spectrum from the interaction $\mathrm{pp} \longrightarrow \mathrm{p_f(K^0_S K^0_S)p_s}$. Figure from reference [60].

3.5.5 A Re-analysis of Mark III Data

The $f_0(1500)$ is also seen in radiative J/ψ decays in a re-analysis of Mark III data performed by Bugg *et al.*, and is reported on in section 3.6.6.

3.6 Experimental Observations of the $\theta/f_J(1710)$

3.6.1 The Crystal Ball Collaboration

The $\theta/f_J(1710)$ was first observed in 1982 by the Crystal Ball collaboration [61] in the decay $J/\psi \longrightarrow \gamma(\eta\eta)$. A fit to the resonance (figure 3.7) yielded the parameters,

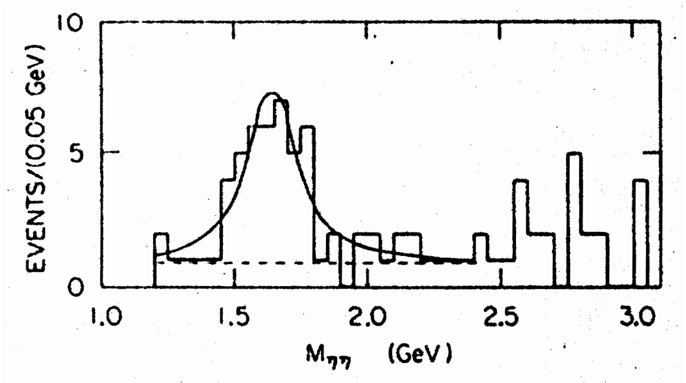

Figure 3.7: The Crystal Ball collaboration's $\eta\eta$ mass spectrum from the decay $J/\psi \longrightarrow \gamma(\eta\eta)$. The $\theta/f_J(1710)$ is seen as an enhancement in the 1650 MeV/c^2 region. The solid curve represents a fit to the mass distribution, while the dashed line represents the background. Figure from reference [61].

$$\begin{aligned} m_{\theta/f_J(1710)} &= 1640 \pm 50 \text{ MeV}/c^2, \\ \Gamma_{\theta/f_J(1710)} &= 220 \,^{+100}_{-\ 70} \text{ MeV}/c^2. \end{aligned}$$

The C-parity of the $\theta/\mathrm{f_J}(1710)$ must be even since it is produced in a radiative decay of the J/ψ, while the $\eta\eta$ decay mode establishes both the spin and parity of the $\theta/\mathrm{f_J}(1710)$ to be even. Although very statistically limited, an analysis of the angular distributions of the decay products was made. It is reported that although both the predictions for a 0^{++} and a 2^{++} $\theta/\mathrm{f_J}(1710)$ fitted the data reasonably well, the spin-two prediction gave a slightly better fit, and so was the favoured result.

3.6.2 The Mark III Collaboration

The Mark III collaboration clearly see the $\theta/\mathrm{f_J}(1710)$ in the first results of their radiative J/Ψ decays. Parameters from the decay $\mathrm{J}/\psi \longrightarrow \gamma(\mathrm{K^+K^-})$ [62] (figure 3.8a) are found to be,

$$\begin{aligned} \mathrm{m}_{\theta/\mathrm{f_J}(1710)} &= 1719 \pm 6\ \mathrm{MeV}/c^2, \\ \Gamma_{\theta/\mathrm{f_J}(1710)} &= 117 \pm 23\ \mathrm{MeV}/c^2. \end{aligned}$$

The $\theta/\mathrm{f_J}(1710)$ is also seen in the $\mathrm{J}/\psi \longrightarrow \gamma(\pi^+\pi^-)$ decay (figure 3.8b).

In 1986 results from hadronic J/ψ decays were published [63]. The decay $\mathrm{J}/\psi \longrightarrow \omega(\mathrm{K^+K^-})$ shows a clear peak in the $\mathrm{K^+K^-}$ invariant mass (figure 3.8c), and yields parameters consistent with the $\theta/\mathrm{f_J}(1710)$. The parameters are,

$$\begin{aligned} \mathrm{m}_{\theta/\mathrm{f_J}(1710)} &= 1731 \pm 10 \pm 10\ \mathrm{MeV}/c^2, \\ \Gamma_{\theta/\mathrm{f_J}(1710)} &= 110\ {}^{+\,45}_{-\,35} \pm 15\ \mathrm{MeV}/c^2. \end{aligned}$$

In the decay $\mathrm{J}/\psi \longrightarrow \phi(\mathrm{K^+K^-})$ there is some evidence of a high mass shoulder to the $\mathrm{f}_2'(1525)$ (figure 3.8d). Using a fit that parameterises the mass spectrum with an $\mathrm{f}_2'(1525)$ plus a non-interfering Breit-Wigner produces parameters for the shoulder of,

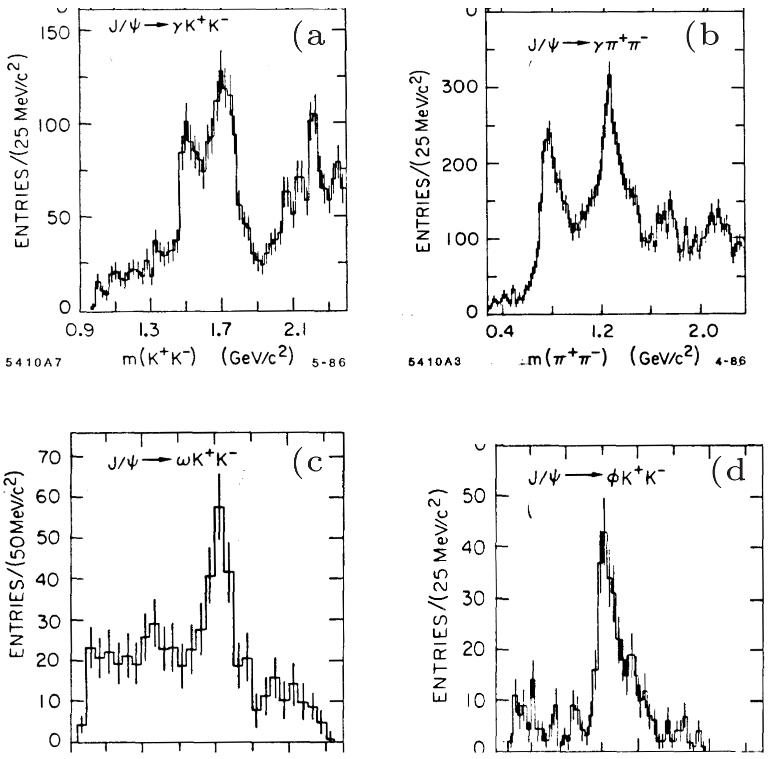

Figure 3.8: The Mark III collaboration's (a, c, d) K^+K^- and (b) $\pi^+\pi^-$ effective mass spectrum from the interactions (a) $J/\psi \longrightarrow \gamma(K^+K^-)$, (b) $J/\psi \longrightarrow \gamma(\pi^+\pi^-)$, (c) $J/\psi \longrightarrow \omega(K^+K^-)$, and (d) $J/\psi \longrightarrow \phi(K^+K^-)$. The $\theta/f_J(1710)$ is produced in all four cases. Figure from reference [63].

$$
\begin{aligned}
m_{\theta/f_J(1710)} &= 1669 \pm 15 \text{ MeV}/c^2, \\
\Gamma_{\theta/f_J(1710)} &= 93 \pm 41 \text{ MeV}/c^2.
\end{aligned}
$$

It is also reported that a fit that parameterises the mass spectrum with an $f_2'(1525)$ and an interfering Breit-Wigner amplitude yields parameters of,

$$
\begin{aligned}
m_{\theta/f_J(1710)} &= 1708 \pm 64 \text{ MeV}/c^2, \\
\Gamma_{\theta/f_J(1710)} &= 100 \pm 40 \text{ MeV}/c^2.
\end{aligned}
$$

These are consistent with the $\theta/\mathrm{f_J}(1710)$.

The results from a spin analysis were published in 1987 [64] using data from the decay $\mathrm{J}/\psi \longrightarrow \gamma(\mathrm{K^+K^-})$. The analysis assumed that the $\theta/\mathrm{f_J}(1710)$ region was pure spin-zero or pure spin-two, and ignored possible interference effects between the $\theta/\mathrm{f_J}(1710)$ and the $\mathrm{f}_2'(1525)$. Results from the analysis showed that spin-two was preferred over spin-zero.

The results from a more sophisticated analysis by Mark III, which includes simultaneous spin-zero and spin-two amplitudes in the fit, and also includes the possibility of an interference effect were published in 1991 [65] and 1992 [66]. These revised analyses produced consistent results for the spin of the $\theta/\mathrm{f_J}(1710)$ region from the J/ψ radiative decays into $\mathrm{K^+K^-}$, $\mathrm{K^0_SK^0_S}$ and $\pi^+\pi^-$ in the mass regions of the $\theta/\mathrm{f_J}(1710)$ and the $\mathrm{f}_2'(1525)$. They show a large spin-zero component in the $\theta/\mathrm{f_J}(1710)$ mass region with the parameters,

$$\begin{aligned} \mathrm{m}_{\theta/\mathrm{f_J}(1710)} &= 1710 \pm 20\ \mathrm{MeV}/c^2, \\ \Gamma_{\theta/\mathrm{f_J}(1710)} &= 186 \pm 30\ \mathrm{MeV}/c^2, \end{aligned}$$

where the errors are statistical only. It is noted that the presence of a smaller ($\sim$24%) spin-two component in the $\theta/\mathrm{f_J}(1710)$ mass region for the $\mathrm{K\overline{K}}$ data cannot be ruled out.

This result is reinforced by the most recent analysis [67] which again examines the decays $\mathrm{J}/\psi \longrightarrow \gamma(\pi^+\pi^-)$, $\mathrm{J}/\psi \longrightarrow \gamma(\mathrm{K^+K^-})$ and $\mathrm{J}/\psi \longrightarrow \gamma(\mathrm{K^0_SK^0_S})$. It is shown that a large amount of S-wave is required near 1·7 GeV/c^2 for the $\mathrm{K\overline{K}}$ data, and that S-wave is required in the range 1·4 GeV/c^2 to 1·8 GeV/c^2 for the $\pi^+\pi^-$data. In addition, there is no evidence for significant structure in the D-wave in the vicinity of 1·7 GeV/c^2, although the existence of small contributions cannot be excluded. The S-wave $\theta/\mathrm{f_J}(1710)$ is found to have the parameters,

$$\mathrm{m}_{\theta/\mathrm{f_J}(1710)} = 1704 \,^{+\,16}_{-\,23}\ \mathrm{MeV}/c^2,$$

$$\Gamma_{\theta/f_J(1710)} = 124 \, {}^{+\,52}_{-\,44} \ \mathrm{MeV}/c^2.$$

3.6.3 The WA76 Collaboration

In 1989 the WA76 collaboration published results [68] from the analyses of centrally produced K^+K^- and $K^0_SK^0_S$ systems at a beam momentum of 300 GeV/c^2. The $K\overline{K}$ mass spectra are shown in figure 3.9. The $\theta/f_J(1710)$ is seen in both channels with parameters for the K^+K^- decay mode of,

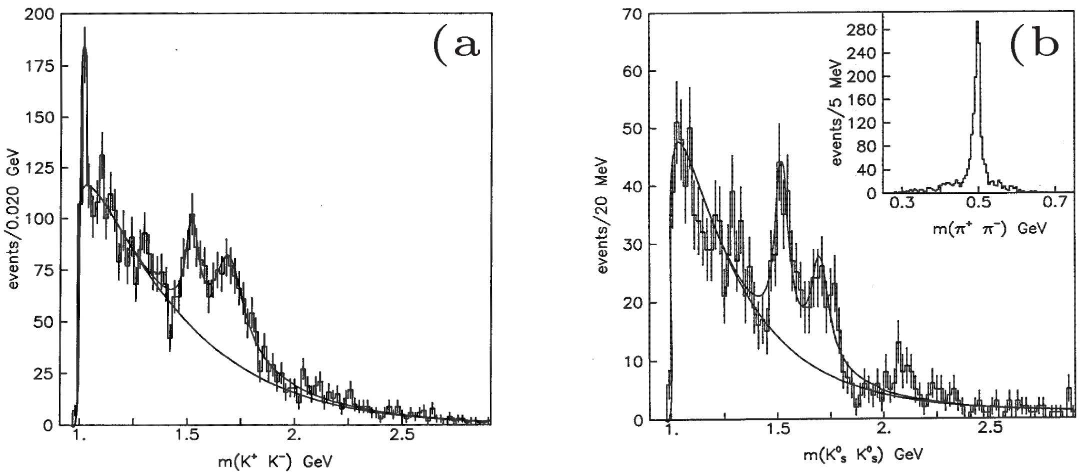

Figure 3.9: The WA76 collaboration's (a) K^+K^- and (b) $K^0_SK^0_S$ effective mass spectra with fits, from the interaction $pp \longrightarrow p_f(K\overline{K})p_s$. Figure from reference [68].

$$m_{\theta/f_J(1710)} = 1713 \pm 10 \ \mathrm{MeV}/c^2,$$
$$\Gamma_{\theta/f_J(1710)} = 181 \pm 30 \ \mathrm{MeV}/c^2,$$

and for the $K^0_SK^0_S$ decay mode of,

$$m_{\theta/f_J(1710)} = 1706 \pm 10 \ \mathrm{MeV}/c^2,$$
$$\Gamma_{\theta/f_J(1710)} = 104 \pm 30 \ \mathrm{MeV}/c^2.$$

In an attempt to assess the spin of the $\theta/\mathrm{f_J}(1710)$ an angular analysis was performed. The resonances at 1500 MeV/c^2 and 1700 MeV/c^2 were isolated into two mass regions, and the decay angular distributions from these two regions were examined. The results showed that the two regions were dominated by D-wave, thus favouring the $\theta/\mathrm{f_J}(1710)$ to be spin-two.

3.6.4 The BES Collaboration

The BES collaboration have published the results of an analysis on data from the interaction $\mathrm{J}/\psi \longrightarrow \gamma(\mathrm{K^+K^-})$ [69]. The mass spectrum, shown in figure 3.10, is very similar to the Mark III data from the same decay (shown in figure 3.8a, page 49). A spin analysis finds that the peak at 1500 MeV/c^2 has $\mathrm{J^{PC}} = 2^{++}$ and hence it is identified with the $\mathrm{f}_2'(1525)$. The peak at 1700 MeV/c^2 is also found to be dominantly $\mathrm{J^{PC}} = 2^{++}$, with the parameters,

$$\begin{aligned} \mathrm{m}_{\theta/\mathrm{f_{J=2}}(1710)} &= 1696 \pm 5\,^{+\,9}_{-\,34}\ \mathrm{MeV}/c^2, \\ \Gamma_{\theta/\mathrm{f_{J=2}}(1710)} &= 103 \pm 18\,^{+\,30}_{-\,11}\ \mathrm{MeV}/c^2, \end{aligned}$$

although it is claimed that there is some evidence for a small scalar component, which accounts for $(30 \pm 10)\%$ of the observed $\mathrm{f_J}(1710)$ region with the parameters,

$$\begin{aligned} \mathrm{m}_{\theta/\mathrm{f_{J=0}}(1710)} &= 1781 \pm 8\,^{+\,10}_{-\,31}\ \mathrm{MeV}/c^2, \\ \Gamma_{\theta/\mathrm{f_{J=0}}(1710)} &= 85 \pm 24\,^{+\,22}_{-\,19}\ \mathrm{MeV}/c^2. \end{aligned}$$

3.6.5 The E760 Collaboration

The E760 collaboration [70] observe a peak at $\sim$1750 MeV/c^2 in the $\eta\eta$ mass spectrum from the interaction $\overline{\mathrm{p}}\mathrm{p} \longrightarrow \pi^0(\eta\eta)$. The mass spectra from interactions with

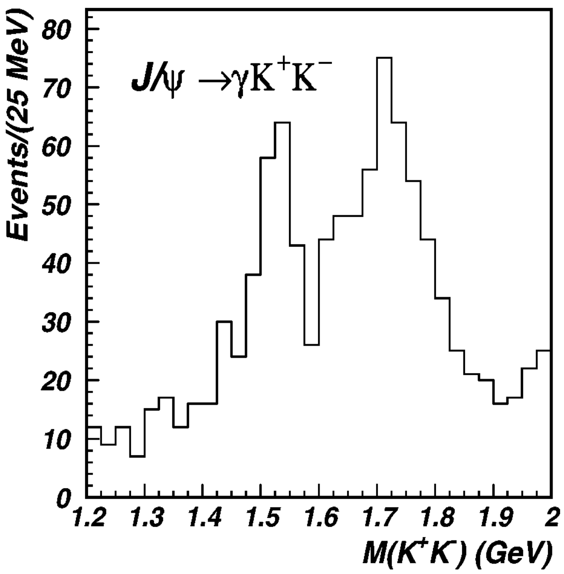

Figure 3.10: The BES collaboration's K^+K^- effective mass spectrum, from the interaction $J/\psi \longrightarrow \gamma(K^+K^-)$. The resonances are identified with the $f_2'(1525)$ and $\theta/f_J(1710)$. Figure from reference [69].

centre-of-mass energies $\sqrt{s} = 3{\cdot}0$ GeV and $\sqrt{s} = 3{\cdot}5$ GeV are shown in figures 3.11a and 3.11b respectively. They are fitted with three Breit-Wigner functions and a polynomial background over the full mass range for the lower centre-of-mass data, and up to a mass of 2250 MeV/c^2 for the higher centre-of-mass data. The central peak in each case is interpreted as the $\theta/f_J(1710)$. The parameters from an average of the two fits are,

$$\begin{aligned} m_{\theta/f_J(1710)} &= 1748 \pm 10 \text{ MeV}/c^2, \\ \Gamma_{\theta/f_J(1710)} &= 264 \pm 25 \text{ MeV}/c^2. \end{aligned}$$

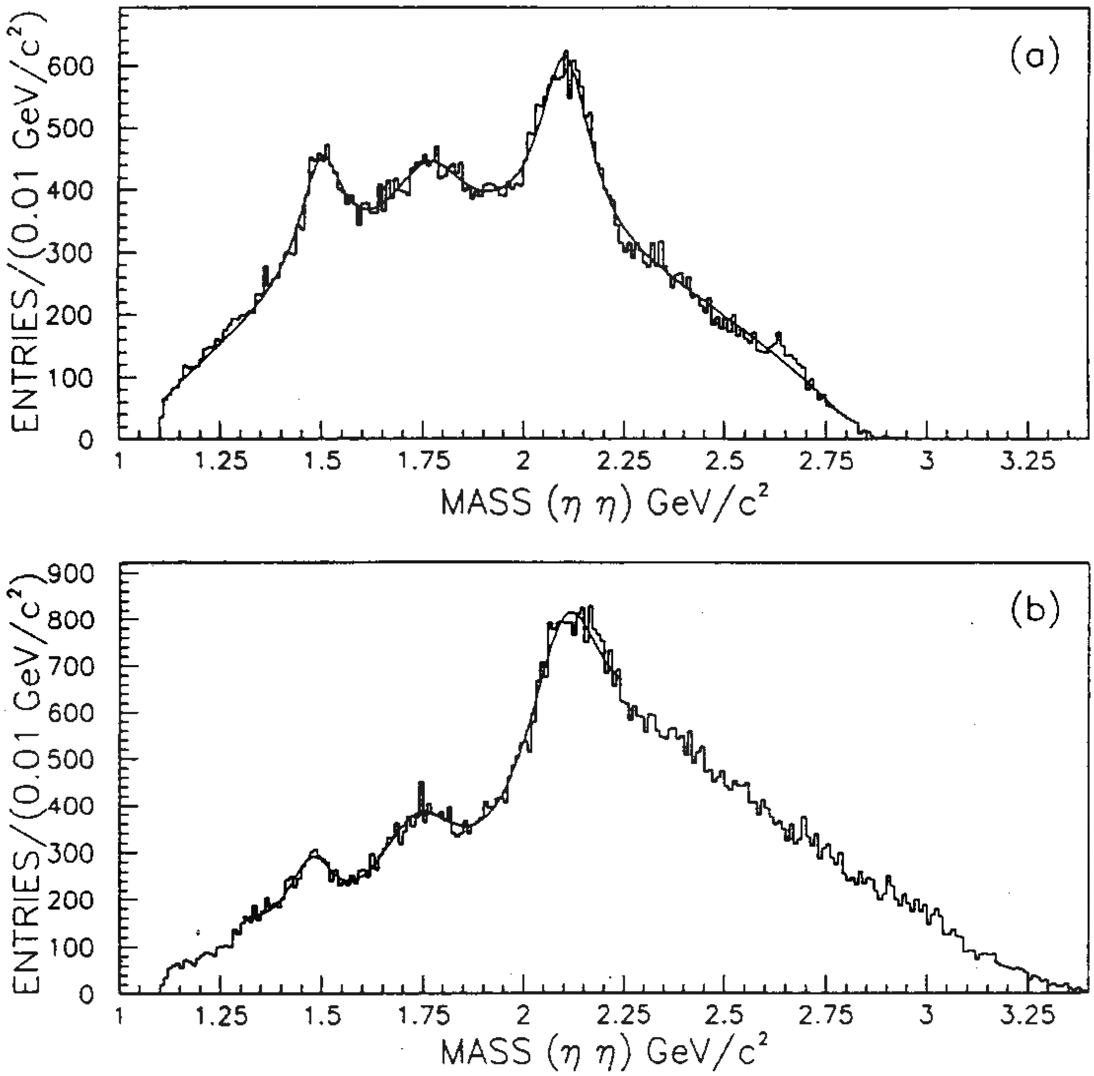

Figure 3.11: The E760 collaboration's $\eta\eta$ effective mass spectrum from the interaction $\overline{\mathrm{p}}\mathrm{p} \longrightarrow \pi^0(\eta\eta)$ at the centre-of-mass energies of (a) $\sqrt{s} = 3{\cdot}0$ GeV and (b) $\sqrt{s} = 3{\cdot}5$ GeV. The peak at ~1700 MeV/c^2 is interpreted as the θ/f$_\mathrm{J}$(1710). Figure from reference [70].

3.6.6 A Re-analysis of Mark III Data

Bugg *et al.* have performed a re-analysis [53] of Mark III's $J/\psi \longrightarrow \gamma(\pi^+\pi^-\pi^+\pi^-)$ data [71]. A significant difference between the original analysis, and the re-analysis, is the inclusion of the $\pi\pi$ S-wave, called the σ. This allows the re-analysis to include the possibility of $J/\psi \longrightarrow \gamma(\sigma\sigma)$ in addition to $J/\psi \longrightarrow \gamma(\rho\rho)$, and gives a considerably improved fit to the data which changes the conclusions drawn about the quantum numbers. The data used is shown in figure 3.12. It is similar in its main features to the data from the E760 collaboration, with peaks at ~1500 MeV/c^2, ~1700 MeV/c^2, and ~2100 MeV/c^2.

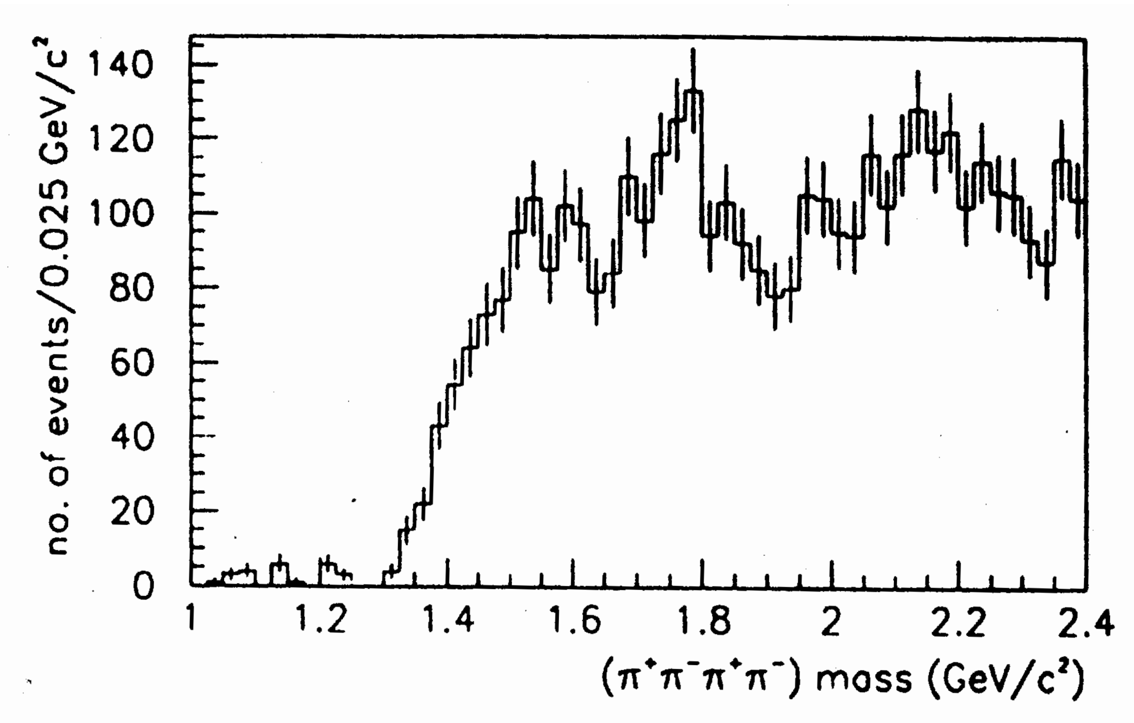

Figure 3.12: The Mark III collaboration's $\pi^+\pi^-\pi^+\pi^-$ effective mass spectrum from the interaction $J/\psi \longrightarrow \gamma(\pi^+\pi^-\pi^+\pi^-)$. These data are used in the re-analysis by Bugg *et al.* Figure from reference [53].

The re-analysis shows evidence for both the $f_0(1500)$ and $\theta/f_J(1710)$ in this mass spectrum. The final fit requires a $J^P = 0^+$ state at 1505 MeV/c^2 which is associated with the $f_0(1500)$. The re-analysis also fits the $\theta/f_J(1710)$ region with a $J^P = 0^+$ component at 1750 MeV/c^2 and a $J^P = 2^+$ component at 1620 MeV/c^2. Table 3.2 shows the masses and widths for the three resonances, while table 3.3 lists the decay modes, the decay fractions required by the fit, and the change in log likelihood (ΔS) to the fit if a component is removed and the remaining contributions are re-optimised. It is noted in Bugg *et al.* that a guideline found from previous experience is that a log likelihood change of $\Delta S = 20$ is strongly suggestive that the original set of decays is correct, while a log likelihood change of $\Delta S = 40$ can be considered definitive.

Table 3.2: Masses and widths of resonances in the 1·5 GeV/c^2 to 1·7 GeV/c^2 mass region, from a re-analysis of Mark III $\pi^+\pi^-\pi^+\pi^-$ data.

	Mass	Width
$f_0(1500)$	1505 MeV/c^2	—
$f_2(1640)$	1620 ± 16 MeV/c^2	$140\,^{+60}_{-20}$ MeV/c^2
$f_0(1750)$	1750 ± 15 MeV/c^2	160 ± 40 MeV/c^2

Table 3.3: Decay properties of resonances in the 1·5 GeV/c^2 to 1·7 GeV/c^2 mass region from a re-analysis of Mark III $\pi^+\pi^-\pi^+\pi^-$ data.

	Decay Mode	Decay Fraction	ΔS
$f_0(1500)$	$\sigma\sigma$	∼100%	38·0
	$\rho\rho$	∼0%	0·41 – omitted
$f_2(1640)$	$\sigma\sigma$	∼0%	0·02 – omitted
	$\rho\rho$	∼100%	41·1
$f_0(1750)$	$\sigma\sigma$	(92 ± 15)%	72·7
	$\rho\rho$	∼8%	14·4

It is noted that the mass of the tensor resonance suggests identification with the $f_2(1640)$ established by the Particle Data Group [72], and that this is the preferred identification in Bugg *et al.*

3.7 Three-State Mixing

The three underlying, or bare, isoscalar scalar states in the mass region of the scalar nonet are the $q\overline{q}$ singlet, the $q\overline{q}$ octet, and the glueball. These states all have the same quantum numbers and so are expected to mix, producing the three physically observed scalar states. This is the same phenomenon as the familiar mixing of isoscalar singlet and octet $q\overline{q}$ states in a nonet. A consequence of this expectation is that the pure glueball will not be an observable entity as once was naively expected, but instead there will be a dominantly glueball state that has some $q\overline{q}$ in its wavefunction, and sticky $q\overline{q}$ mesons that have some glueball component in their wavefunctions. The state that is dominantly glueball may be identified by applying the same criteria as previously outlined. Although the expected glueball characteristics will not be as pronounced for a mixed glueball-$q\overline{q}$ state as for a pure glueball, the same predicted traits are expected to apply.

The only glueball characteristic which is qualitatively altered is that of the flavour dependence of the decays. Even if there is only a relatively small non-$x\overline{x}$[2] admixture in the wavefunction of an $x\overline{x}$ state, the flavour dependence of the decays of that state can differ significantly from what would be expected if it were a pure $x\overline{x}$ state.

If the $\theta/f_J(1710)$ is spin-zero then the $f_0(1370)$, $f_0(1500)$, and $\theta/f_{J=0}(1710)$ will be the three isoscalar states involved in this mixing. By using the bare masses determined from the lattice, and the expected level of mixing, the proportions of the bare states contributing to the physical particles can be evaluated. This provides information about the whole isoscalar scalar system, and specifically it allows the identification

[2]Where $x\overline{x}$ refers to any one of the three pure states, $\frac{1}{\sqrt{2}}(u\overline{u} + d\overline{d})$, $s\overline{s}$ or gg.

of the dominantly glueball state.

Two scenarios of three-state mixing which have been proposed are those of Amsler and Close [44], and Lee and Weingarten [73]. The former explores the situation where the glueball is between the $f_0(1370)$ and the $f_0(1500)$ in mass, leading to an approximately equal sharing of the glueball wavefunction between the $f_0(1500)$ and the $\theta/f_{J=0}(1710)$. The latter explores the situation where the glueball is above the $f_0(1370)$ and the $f_0(1500)$ in mass, leading to the glueball wavefunction residing dominantly within the $\theta/f_{J=0}(1710)$.

The same three-state mixing method is used in both cases, and despite the different conclusions about the identification of the glueball, the results from the calculations share several similar features. The solutions for the lowest mass state are similar, as is the qualitative importance of the glueball component in the high mass state. Also, both solutions exhibit destructive interference between the $n\overline{n}$ and $s\overline{s}$ flavours for the middle state, which causes the suppression of decays to $K\overline{K}$ final states.

3.8 Summary

The knowledge of scalar states in the mass region of 1·3 GeV/c^2 to 1·7 GeV/c^2 has improved greatly due to results from the analyses of high statistics experiments. In addition to this two glueball candidates are now known of, the $f_0(1500)$ and the $\theta/f_J(1710)$, while no other known scalar states are compatible with possessing a gluonic sub-structure. Although it is known from the decays $\theta/f_J(1710) \longrightarrow \gamma(\eta\eta)$ and $\theta/f_J(1710) \longrightarrow \gamma(K^0_S K^0_S)$ that the J^{PC} values of the $\theta/f_J(1710)$ must be either 0^{++} or 2^{++}, measurements of the spin of the $\theta/f_J(1710)$ have so far been contradictory. It is crucial for the identification of the lightest glueball to reliably measure this quantum number.

If the $\theta/f_J(1710)$ is found to be tensor, then the $f_0(1500)$ will stand unchallenged as the lightest scalar glueball. The $\theta/f_{J=2}(1710)$ is too light to be the tensor glueball according to lattice QCD calculations, and this conclusion is reinforced by the partial decay width of $J/\psi \longrightarrow \gamma(\theta/f_{J=2}(1710))$, which would be too small for the $\theta/f_{J=2}(1710)$ to be the tensor glueball according to Close, Farrar and Li [22]. A satisfactory interpretation of the $\theta/f_{J=2}(1710)$ would be required to reconcile the theoretical predictions that the $\theta/f_{J=2}(1710)$ is not a glueball with the experimental evidence that the $\theta/f_J(1710)$ possesses many glueball characteristics, including that fact that it is seen in all glue-rich interactions and is heavily suppressed in normal hadronic interactions, and that the $\theta/f_J(1710)$ decays strongly to $K\overline{K}$ final states and yet is not seen in K^- incident beam experiments as would be expected if it were a dominantly $s\overline{s}$ state.

If the $\theta/f_J(1710)$ is found to be scalar, then the $f_0(1500)$ and $\theta/f_{J=0}(1710)$ will both be good candidates for the scalar glueball, and furthermore, the need for the existence of glueballs to explain the experimental data will be firmly established. The expected three-state mixing predicts that one of the resonances will be predominantly glueball while the other will be predominantly $s\overline{s}$, or that there may even exist an equal sharing of the glueball's wavefunction between the two.

Chapter 4

The WA102 Experiment in 1996

The WA102 experiment is a continuation of the WA76, WA76′, and WA91 experiments and has had two 100 day runs, one in 1995 and one in 1996. Half a billion triggered events were recorded by the experiment and these have now been processed through the event reconstruction programs (described in section 4.4) and are being analysed.

4.1 Particle Detectors and Hardware

There follows a description of the detectors and major components of the 1996 run of the WA102 experiment, the layout of which is shown in figure 4.1. The co-ordinate system of the Ω Spectrometer is defined with a vertical z-axis that is positive in the upward direction, and which is anti-parallel to the direction of the magnetic field. The x-axis is defined to be along the beam direction, and is positive in the downstream direction. The y-axis is horizontal, mutually perpendicular to both the z and x-axes, and is defined to be positive in the leftwards direction when looking downstream. For more detailed information than is presented here on the layout of the apparatus, the trigger conditions, and the data processing, see references [74, 75].

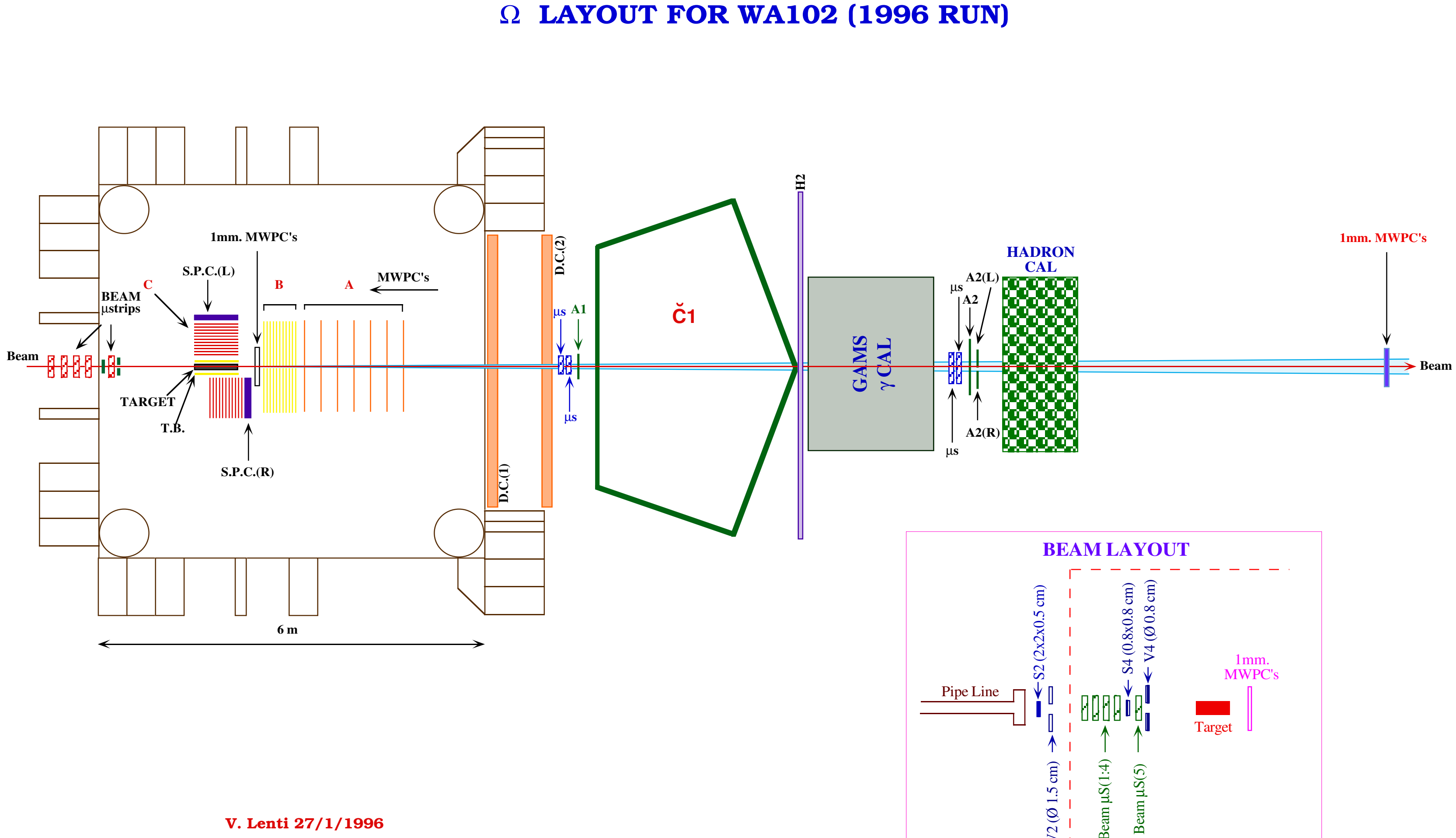

Figure 4.1: The Ω layout for the 1996 WA102 run.

4.1.1 The Magnet

The Ω Spectrometer uses a superconducting magnet in a Helmholtz coil arrangement which can sustain a magnetic field of up to 1·8 Tesla. The field is very uniform in the region enclosing the A, B and C multi-wire proportional chambers (described in section 4.1.8). The magnet was operated at 1·35 Tesla during the WA102 run to optimise the curvature of the medium momentum tracks and the slow proton track for reconstruction.

4.1.2 The Beam

The experiment operates using a proton beam at a momentum of 450 GeV/c which is emitted from the H1 beam line in the West Area at CERN. The beam is extracted from the Super Proton Synchrotron and is essentially entirely protons at a very precise momentum. No secondary targets were used.

4.1.3 Beam Scintillators

The beam is measured before it interacts with the target (see inset in figure 4.1). Two scintillator counters (S2 and S4) measure the beam intensity, while two veto scintillator counters (V2 and V4) are required to have no hits. All of the above are square slabs;

- S2 is of side 2·0 cm and is 0·5 cm thick.
- S4 is of side 0·8 cm and is 0·5 cm thick.
- V2 is of side 17 cm and thickness 1 cm, and has a hole in its centre of diameter 1·5 cm to allow the beam through.
- V4 is of side 17 cm and thickness 1 cm, and has a hole in its centre of diameter 0·8 cm to allow the beam through.

4.1.4 Beam Microstrips

These consist of silicon strips at a pitch of 20 μm held at a bias voltage of $\sim$80 V. Their high spatial accuracy is necessary for the reconstruction of the beam so that its direction can be accurately found. There are 10 planes which are grouped into doublets and attached to a rigid optical bench which serves as a reference for the microstrip planes. The specifications for doublets 1 to 5 are listed in table 4.1.

Table 4.1: Specifications of the beam microstrips used in the 1996 run.

Name	Planes	Pitch	Channels	Dimensions (mm)	x-position (m)
Doublet 1	2 (ZY)	20 μm	512	$10{\cdot}24 \times 10{\cdot}24$	$-3{\cdot}998, -3{\cdot}995$
Doublet 2	2 (ZY)	20 μm	512	$10{\cdot}24 \times 10{\cdot}24$	$-3{\cdot}942, -3{\cdot}931$
Doublet 3	2 (ZY)	20 μm	512	$10{\cdot}24 \times 10{\cdot}24$	$-3{\cdot}326, -3{\cdot}315$
Doublet 4	2 (ZY)	20 μm	512	$10{\cdot}24 \times 10{\cdot}24$	$-2{\cdot}729, -2{\cdot}718$
Doublet 5	2 (YZ)	20 μm	512	$10{\cdot}24 \times 10{\cdot}24$	$-2{\cdot}686, -2{\cdot}676$

4.1.5 Target

The target is a 60 cm long cylinder of liquid hydrogen contained within a mylar and aluminium canister, it represents 10% of an interaction length. It is common to use beryllium targets to give a similar interaction length in a shorter physical distance. This enables the interaction vertex to be reconstructed more easily. However, this is not done in WA102 so as not to introduce nuclear effects, and to ensure that only pp interactions can occur. The interaction vertex can be reconstructed accurately in the x-direction by the slow proton detection system.

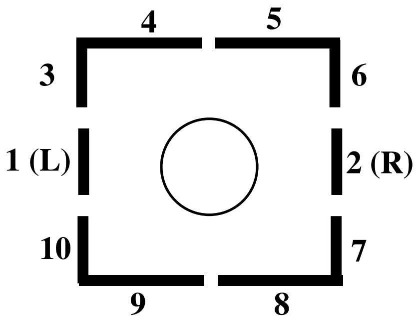

Figure 4.2: Labelling of the target box elements.

4.1.6 Target Box

The target box consists of 10 scintillator slabs surrounding the target on four sides. The slabs are numbered as depicted in figure 4.2. The box is left open at the upstream and downstream ends in order to let through the beam, and particles from interactions. The box is 60 cm long in the beam direction while the two vertical faces are positioned at $y = -20$ cm and $y = 20$ cm, and similarly the horizontal faces are positioned at $z = -20$ cm and $z = 20$ cm. Slabs 3 – 10 are 1 cm thick, and veto an event if they record any hits. Either slab 1 or 2 must record a hit for a good event, and so they are thinner (at 0·5 cm thick) to reduce the quantity of material through which a slow proton must pass.

4.1.7 Slow Proton Counters

There are two slow proton counters, one on the left side of the target, SPC(L), and one on the right side, SPC(R). Both are composed of 14 scintillator slabs held in an aluminium frame in such a way that the entire assembly is vertical. The SPC(L) slabs were of width 6 cm, and all were active. The SPC(R) slabs were of width 7 cm and all were active with the exception of two, the highest and lowest slabs in the array.

4.1.8 Multi-Wire Proportional Chambers

The Multi-Wire Proportional Chambers (MWPCs) are labelled A, B and C in figure 4.1. The A and B-chambers are located downstream of the target and are used to define the medium momentum forward-going tracks. The C-chambers are positioned on either side of the target, and are used to measure the the slow proton tracks. The left C-chambers are mounted with their planes parallel to the x-axis, and the right C-chambers are mounted perpendicularly to it. The reason for this arrangement is shown in figure 4.3.

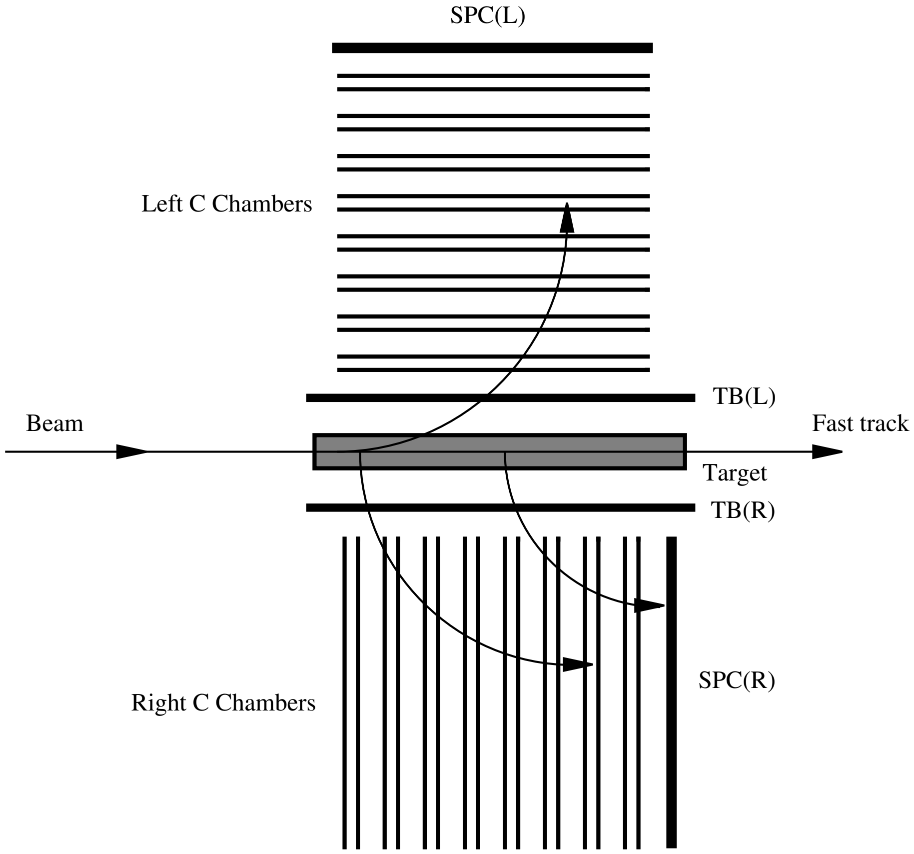

Figure 4.3: Orientation of the C-chambers.

It can be seen that because of the direction in which positive particles are bent in the Ω magnetic field, in order to get the best acceptance for slow protons the two C-chambers must be mounted at right angles to one other. This improves the acceptance of the right C-chambers, although it should be noted that the acceptance is still limited in comparison to that of the left C-chambers. This is because particles emitted to the left from any point along the length of the target have a high probability of traversing all, or nearly all, of the planes in the left C-chambers, whereas those emitted to the right will traverse a significant number of planes in the right C-chambers only for a more restricted range along the length of the target cylinder. This is an important effect which is apparent in the data presented in chapter 5 by the relatively low numbers of events with a slow right proton as compared with those with a slow left proton.

The A-chambers consist of 7 modules, each containing 3 planes of wires, labelled Y, U, and V. The Y planes are aligned to the vertical axis in the Ω system, and the U and V planes are inclined at $\pm 10{\cdot}14^{\circ}$ to the Y planes respectively. The B and C-chambers both have 8 modules, where each module consists of 2 planes, one Y and the other alternately U and V. In all cases, the wire spacing is 2 mm. The chambers are filled with a mixture of isobutane and alcohol.

4.1.9 One Millimetre Chambers

In addition to the A, B and C MWPCs, three further sets of MWPCs with a wire spacing of 1 mm are used, each of which has four planes. The first of these is located between the target and the B-chambers at $x = -0{\cdot}80$ m. Its planes are, Y, Z, U, and V (YZUV), where the Z-direction is perpendicular to both Y and the beam direction; it is used to give extra points for track reconstruction for the fast track and centrally produced tracks. The other two chambers are placed at $x = 19{\cdot}00$ m and $x = 19{\cdot}40$ m, these chambers contain YZYZ and YZUV planes respectively. Both are used to provide extra information for accurate reconstruction of the fast track.

4.1.10 Drift Chambers

Immediately outside the Ω magnet, situated at 3·27 m and 4·41 m in the x-direction, are two high-precision drift chambers, marked DC(1) and DC(2) in figure 4.1. Each chamber comprises 4 planes, Y, U, Y, and V, using the same notation as that for the MWPCs in section 4.1.8. Each plane has a 2·5 cm spacing between the sense and field wires, the sense wires are where the liberated electrons are collected and the field wires are used to stabilise the field across the volume of the chamber, the drift velocity is $\sim$5 cm/μs. Information from the drift chambers is used in the reconstruction of the tracks of medium momentum particles, and DC(2) is the last recorded point of a track that is used for the momentum determination of the particle by the reconstruction program TRIDENT.

4.1.11 Downstream Microstrips

The downstream microstrips are used to reconstruct the fast track. They are also used to reconstruct beam particles which pass through the target without interacting, the information from which is used as a reference for detector alignment. There are two quadruplets, one at $x \sim 5$ m and the other at $x \sim 10$ m, their specifications are shown in table 4.2.

Table 4.2: Specifications of the downstream microstrips used in the 1996 run.

Name	5 m QUAD	10 m QUAD
Planes	4 (ZYZY)	4 (ZYZY)
Pitch	25 μm	25 μm
Channels	2048	2048
Dimensions (mm)	51·2 $\times$ 51·2	51·2 $\times$ 51·2
x position (m)	5·330, 5·355, 5·380, 5·405	10·462, 10·487, 10·512, 10·537

4.1.12 Downstream Scintillators

The downstream scintillators used to trigger on the fast proton are A1, A2, A2(L), and A2(R). A1 is a square slab of side 2·5 cm, positioned at $x = 4{\cdot}9$ m. A2 is also a square slab, but of side 5·0 cm and positioned at $x = 10{\cdot}8$ m. A2(L) and A2(R) are located immediately behind A2, to the left and right sides of the beam direction respectively as shown in figure 4.1. The reason for this is to find the position of the fast track in the y-direction at this point.

4.1.13 Čerenkov Detector

The threshold Čerenkov detector (Č1) is used in the identification of charged kaons. The shape of the detector is such that the acceptance is optimised for centrally produced particles of momenta between $\sim$5 GeV/c and $\sim$20 GeV/c after the magnetic field has altered their trajectory. Č1 has 32 mirrors of high reflectivity along the back wall in two rows of 16, the horizontal line dividing the rows being at $z = -0{\cdot}5$ cm. The mirrors reflect and focus light towards 32 corresponding photomultiplier tubes. A horizontal light-opaque membrane is also at $z = -0{\cdot}5$ cm to prevent the light-cone from a particle at $z < -0{\cdot}5$ cm hitting a mirror in the top row, or *vice versa*, and hence causing an ambiguity in the data. The chamber Č1 was originally filled with N_2 but was changed to CO_2 during the run. The change is made to the gas with the higher refractive index to increase the photon yield in the chamber, and hence improving efficiency.

4.1.14 Hodoscope

The hodoscope H2 measures the location in the y-direction through which central particles pass. H2 consists of 72 vertically oriented scintillator slabs. These are constructed into two rows of 36 slabs each and the slabs in a row overlap each other by a third of their width on either side. A horizontal gap of $\sim 0{\cdot}5$ cm exists at $z = -5$ cm which separates the two rows and provides a space for the beam to pass through.

4.1.15 Electromagnetic Calorimeter: GAMS-4000

GAMS-4000 [76] is a large photon detector forming a lead-glass wall of nearly 2·5 m × 2·5 m, made of 4096 lead-glass cells (each of dimensions 38 mm × 38 mm × 450 mm) assembled in a 64 × 64 matrix. A high energy ($\geqslant 0{\cdot}2$ GeV) photon incident on the detector develops an electromagnetic shower inside the lead-glass. The electrons and positrons from a shower emit Čerenkov light proportional to the energy of the incident photon. Each lead-glass cell is viewed at one end by a photomultiplier tube which measures the intensity of the light emitted in that cell. The width (38 mm) of each cell has been chosen to be of the same order as the lateral extension of the showers (as a result, at most 25 cells (5 × 5) around the cell which contains the impact point of an incident photon give a significant signal). Thus by a summation of these signals it is possible to obtain the energy of the incident photon. The co-ordinates of the incident photon can also be calculated, with a precision of the order of 1 mm, from the light distribution amongst the cells. The granularity of this detector allows the measurement of the position and the energy of up to 20 photons per event. The four central cells of GAMS-4000 are missing to provide a hole for the beam.

4.2 Trigger Requirements

As double Pomeron exchange becomes more important at high $\sqrt{s}$ and low $|t|$ transfers, the WA102 experiment is designed to record events of the form $\mathrm{pp} \longrightarrow \mathrm{p_f}(\mathrm{X}^0)\mathrm{p_s}$ in these kinematical regions. To ensure that low $|t|$ interactions were measured the experiment is designed to trigger upon one very slow momentum proton (<

1 GeV/c), and one very fast momentum proton (typically in the range of 350 GeV/c to 450 GeV/c) with low p_{T}. This forms the principal trigger requirement for an event to be recorded. For certain classes of event evidence of central particles is also required.

4.2.1 Slow Proton

The slow proton fulfills its trigger tests if the following points are satisfied (these conditions are for a slow left proton, with the corresponding condition for a slow right proton following in square brackets if different);

- Elements $3 \rightarrow 10$ of the target box have no hits.
- Element 1 [Element 2] of the target box fires. See target box figure (figure 4.2).
- SPC(L) [SPC(R)] has 1 or 2 hits with pulse heights compatible with a proton.
- The C-chambers C5 and C7 on the left side [C7 and C9 on the right side] both show hits compatible with the passage of a single particle.

4.2.2 Fast Proton

For a fast proton to trigger it is required that (these conditions are for a fast left proton, with the corresponding condition for a fast right proton following in square brackets if different);

- The A1 scintillator fires in coincidence with the A2 scintillator.
- The A2(L) [A2(R)] scintillator fires.

4.2.3 Central Particles

The central particles have less trigger requirements than the protons. If during an event the fast and slow protons are emitted either both in a leftwards direction, or both in a rightwards direction, then central particles are not checked for as they must be present for the interaction to conserve momentum. If the protons are not emitted in either of these configurations then the FASTRO [77] readout system on the A3 chamber (see section 4.3.4), or the GAMS-4000 trigger, are required to display hits as evidence of the presence of central particles.

4.2.4 Antiselection Considerations

The trigger is designed to enhance the number of Double Pomeron Exchange (DPE) interactions recorded with respect to other types of interaction by only triggering on events with a low momentum transfer. This kinematical design enhances the proportion of DPE interactions recorded. However, there are still two production processes which have greater cross-sections than DPE, and which need to be vetoed.

1. **Elastic Interactions.**

   The elastic scattering pp $\longrightarrow$ pp is a low momentum transfer interaction and so has kinematically similar fast and slow protons to DPE. This type of interaction is vetoed by requiring either (i) that an event cannot have originated from a single-exchange process due to momentum conservation, or (ii) that there is evidence for the production of medium momentum central particles, which is found by checking for activity in the A3 A-chamber, and in GAMS-4000.

2. **Forward Diffraction.**

Forward diffractive interactions of the type,

$$\mathrm{p\,p} \longrightarrow \mathrm{p_s}\,\Delta^{++}(1232)\,\pi^-,$$

followed by $$\Delta^{++}(1232) \longrightarrow \mathrm{p_f}\,\pi^+,$$

and,

$$\mathrm{p\,p} \longrightarrow \mathrm{p_s}\,\Lambda^0(1520)\,\mathrm{K}^+,$$

followed by $$\Lambda^0(1520) \longrightarrow \mathrm{p_f}\,\mathrm{K}^-,$$

where the beam proton is changed in the interaction to an excited baryon that subsequently decays to a fast proton and a pion, produces fast and slow protons which may be triggered upon. If the mesons produced are then kinematically compatible with central particles they will also be accepted, thereby contaminating the DPE signal.

It has been found duing the analysis of the $\pi^+\pi^-$ channel [78], where there is a high contamination from the Δ^{++}, that the problem can be dealt with by cutting on the effective $\mathrm{p_f}\pi^+$ mass to exclude events with $m_{\mathrm{p_f}\pi^+} \leqslant 1{\cdot}5$ GeV/c^2.

3. **Backward Diffraction.**

If backward diffraction occurs, the target may fragment into low momentum particles, where the target undergoes the same processes as the beam in forward diffraction. The target box requires that one, and only one, of its elements (either element 1 or element 2) may be hit, which reduces the chance of this type of interaction being accepted. It is, of course, possible that two or more slow particles may exit through the same, valid element of the target box. The possibility of them completing the slow proton part of the trigger requirements is further reduced by the criterion that $\leqslant 2$ slabs of the SPC fire. In addition to this the pions are distinguishable from the protons by the pulse-heights from the SPC slabs, as they deposit less energy in the scintillator than protons. In this way the pions are discriminated against thereby reducing the possibility of contamination from backward diffraction.

4.3 Trigger Logic

The relatively small cross-section for DPE compared with competing processes such as those briefly discussed in section 4.2.4 means that an effective and stringent trigger needs to be used. Although the trigger logic is complex some key features are described in this section.

4.3.1 Clean Beam

It is required that the beam protons are single and that they have a minimum separation from one another – this is the definition of *clean beam*. If two protons in the beam are too close to one another then products from both interactions could be observed by the detectors, producing information that will be incorrectly interpreted as a single central production interaction. If this were to occur on a regular basis it would slow the data acquisition considerably as the later, more time-intensive checks would be needed to filter out these erroneous events; they may even be written to tape and analysed, wasting further resources. For these reasons a rapid early test is used. A beam veto decision is taken based upon the pulse height from the S2 scintillator, which must not be greater than the pulse height that typically results from a single proton at the beam momentum.

The *past-future protection* logic deals with vetoing double beams and ensures that only clean beam is used, its operation is illustrated in figure 4.4. First, the existence of a good beam signal is established using signals from S2, $\overline{\mathrm{V2}}$, S4 and $\overline{\mathrm{V4}}$. Clean beam is then dependent upon the coincidence of four signals. Three of the signals are the original S2 (S2), a shaped S2 signal (S2P) and a good beam signal (BEAM),

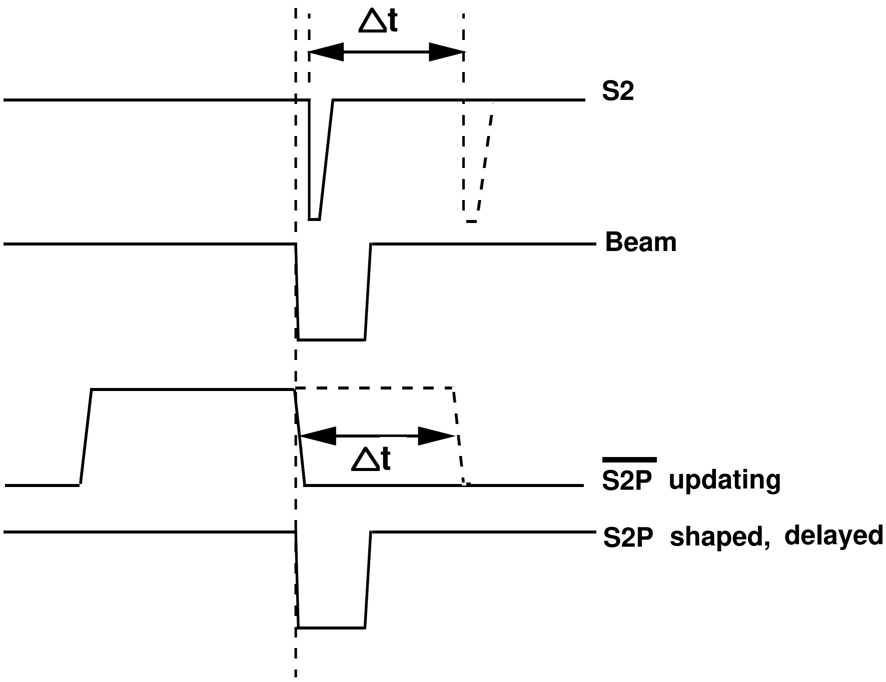

Figure 4.4: Timing of clean beam coincidence signals.

these are all delayed by the same time (∼50 ns). The fourth signal is that of a shaped and inverted S2 ($\overline{\text{S2P}}$); this signal is produced in an updating discriminator. It can be seen that if a proton passes then the $\overline{\text{S2P}}$ signal goes to 0. When it returns to 1 the other three inputs to clean beam (due to the specific delay of ∼50 ns) are also at 1. This is defined as clean beam. However, should a second proton pass through before the $\overline{\text{S2P}}$ plateau has expired then the updating discriminator maintains $\overline{\text{S2P}}$ at 0 for a further ∼50 ns, and the coincidence of the four signals is disrupted.

4.3.2 Trigger Types

The trigger logic makes a distinction as to whether the slow and fast particles are on the left (L) or right (R) side of the beam. The notation used is 'slow fast', so for example if the slow proton was on the left of the beam, and the fast proton was on the right then it would be called an 'LR' event. This gives four combinations, LL, RR, LR and RL.

4.3.3 Dead Time

It can be noted that the WA102 experiment is not dead time (DT) limited, as only about 30% of the time during normal operation is spent in DT. If an event passes certain criteria then the DT signal, which lasts for 450 ns, is started. The DT signal means that the information from the event will be analysed further, using the *level 1* electronics. It also means that any subsequent events will be ignored until DT ends. DT needs to be started as late as possible as a greater time before starting DT means that more stringent criteria can be enforced on the event before the electronics commit themselves to level 1. It is important that the chosen event is selected by the best fast checks possible before this happens.

The biggest time constraint for the trigger is the need to *strobe* the 5 m and 10 m microstrips. The 'Front End Read Out microStrip' (FEROS) cards contain the pre-amplifier electronics attached to the microstrips which require ∼250 ns to reach the optimum pre-amplification point for reading out information. This means that if time zero (t = 0 ns) is assigned to when the beam proton passes the S2 scintillator, there exists ∼250 ns in which to send an affirmative signal to the 5 m and 10 m microstrips to strobe the pattern. Taking into account the time required for a signal to travel the distance between the trigger room and the two microstrip stations, and the time saved by the time of flight of the incident particle, a decision to strobe the microstrips and to begin DT must be made in $\leqslant$ 83 ns.

4.3.4 Central Particle Logic

If an event is LR or RL the trigger requires that either the FASTRO[1] [77] device on A3 records activity, or that GAMS-4000 triggers (which occurs when a particle

[1]A Fast Readout (FASTRO) device is attached to the chamber A3. This can detect activity in the A3 chamber and relay the information quickly enough for it to be involved in the trigger decision.

deposits > 5 GeV of energy in it). These criteria are applied so that there is evidence of the passage of central particles. A multiplicity counter (MUSIC) also attached to A3 vetos events if it detects 6 or more hits in A3. The FASTRO can rapidly read the A3 chamber because it reads wires in groups of eight at a time as opposed to individually. This brings the time taken for read out down from $\sim$100 μs to $\sim$10 μs for this chamber.

4.3.5 Level 2 Trigger

While DT is in operation, the level 1 electronics check the C-chambers for activity and for multiplicity. If these qualify then level 1 is passed and the data acquisition system (DAQ) reads out all information into the buffers. This requires $\sim$200 μs, and during this time a busy signal is sent to maintain DT. This stage is dealt with by the trigger processor MUTUN, and if passed then the DAQ collects all the buffered information together and reads it out to tape, which requires $\sim$700 μs.

4.4 Event Reconstruction

4.4.1 Track Fitting

The experimental data taken were processed through a track reconstruction program, called TRIDENT, which attempts to reconstruct events by track recognition, momentum calculation and the production of fits to primary and/or secondary vertices. Wire hits in several planes at different inclinations are combined to provide a large number of constraints to the fitting procedure, this also helps to reduce the effects of chamber inefficiencies. The curve fitting for the slow proton is achieved by using C-chamber data in coincidence with the fired SPC element. For the fast proton the momentum is found from the 5 m and 10 m microstrip detectors combined with the 1 mm MWPCs at $\sim$19 m. The final 1 mm chamber is less spatially accurate than the microstrips, but its distance makes it a valuable lever-arm. Charged medium momentum central particles are measured using the A and B-chambers and the drift chambers DC(1) and DC(2). Electromagnetic decays are recorded using GAMS-4000 which measures the energy deposited in its cells and the spatial co-ordinates of the hits.

Charged kaon identification is performed using the threshold Čerenkov counter Č1. Kaons are also required to exhibit a complementary hit in the H2 element directly behind the Čerenkov cell through which they had passed. This confirms the passage of particle through Č1 and reduces the possibility that an interaction, decay, or incorrect software track tracing between DC(2) and Č1 has occurred.

4.4.2 Vertex Finding

The x co-ordinate of the primary vertex is found by intersecting the slow proton track with the beam track. The beam track is then retraced to this x-position. The y and z co-ordinates of the beam are accurately known, and they are used as the y and z co-ordinates of the primary vertex. The last measured points of the forward going particles are in the drift chambers. Including the central track information from the A-chambers, B-chambers, and drift chambers, a fit is made to find the best track parameters.

Tracks coming from the decay of a V^0 near the primary vertex may be incorrectly assigned as originating at the primary vertex. In order to deal with this problem all events are run through a V^0 recovery program [79] after the initial TRIDENT process. This takes all combinations of positive and negative tracks that have not been assigned to a V^0 by TRIDENT and further investigates the possibility that they may have in fact originated from a V^0. In order to do this the combinations are assessed to see if they will trace to a vertex at least 3 cm downstream from the primary vertex, with an impact parameter greater than 0·05 cm at the primary vertex.

Chapter 5

Selection of the K^+K^- Channel

The WA102 experiment ran in 1996 for 100 days of data taking, during which 300 million triggers were accumulated. The reconstruction package TRIDENT was used to process the information recorded by the detectors from the interactions into full events. Once completed, the various decay channels were isolated by selecting different final states such as $\pi^+\pi^-$, K^+K^-, $K^0_S K^\pm \pi^\mp$, *etc.* The selection of each channel requires specific sets of cuts to reduce to a minimum contamination from other decay modes. This chapter describes the criteria and cuts applied to select a clean K^+K^- channel.

5.1 Initial Signal Selection

Initially $pp \longrightarrow p_s(h^+h^-)p_f$ events (where h refers to a hadron), such as $\pi^+\pi^-$, K^+K^-, and $p\overline{p}$, are selected by requiring that an interaction has four outgoing charged tracks, with no V^0s present. The longitudinal and transverse missing momentum spectra of these events are shown in figures 5.1a and 5.1b respectively. The asymmetry in the longitudinal missing momentum distribution, and the excess of events peaking at $\sim$0·3 GeV/c in the transverse missing momentum distribution are

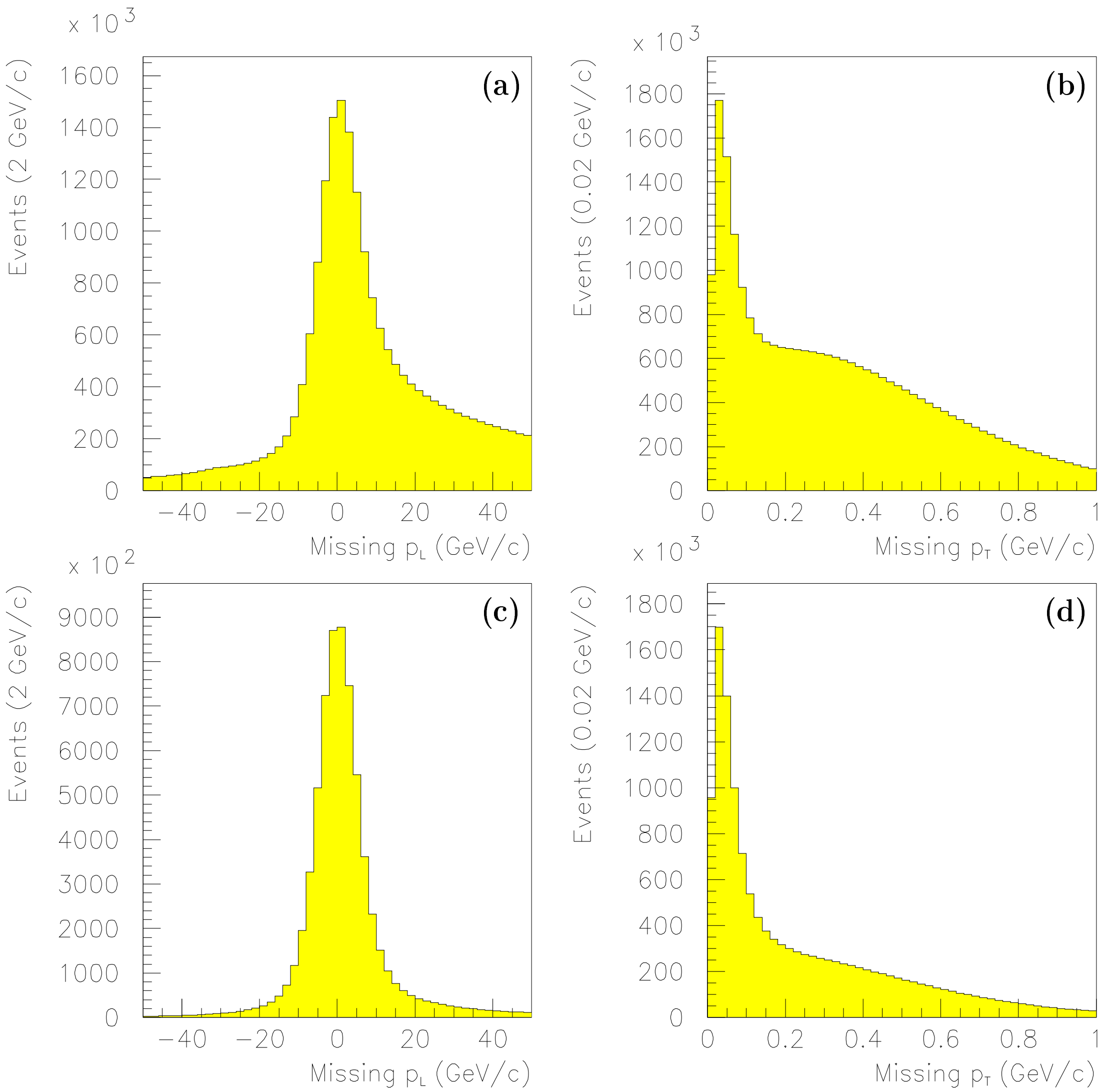

Figure 5.1: The (a) longitudinal and (b) transverse missing momentum spectra for h^+h^- events. The same spectra are shown in (c) and (d) after reciprocal missing momentum cuts.

due almost entirely to $\pi^+\pi^-(\mathrm{n}\gamma)$ central systems, the main contributor to which is $\pi^+\pi^-(\pi^0\rightarrow 2\gamma)$. In order to remove the unwanted events, missing momentum cuts are applied. The cuts used are,

$$
\begin{aligned}
|\text{missing } p_x| &< 14{\cdot}0 \text{ GeV}/c, \\
|\text{missing } p_y| &< 0{\cdot}16 \text{ GeV}/c, \\
|\text{missing } p_z| &< 0{\cdot}08 \text{ GeV}/c.
\end{aligned}
$$

The longitudinal missing momentum after the missing p_y and p_z cuts is shown in figure 5.1c, while the transverse missing momentum after the missing p_x cut is shown in figure 5.1d. The longitudinal missing momentum distribution is now almost symmetrical and Gaussian in shape with little background, and the transverse missing momentum distribution no longer has the shoulder of events previously evident. The distributions are now consistent with centrally produced $\mathrm{h}^+\mathrm{h}^-$ events, and the data within the stated missing momentum cuts are used.

5.2 Diffractive Contamination

The centrally produced $\pi^+\pi^-$ channel suffers from contamination from diffractive events of the type $\mathrm{pp} \longrightarrow \mathrm{p_s}\pi^-\Delta^{++}$, where $\Delta^{++} \longrightarrow \mathrm{p_f}\pi^+$, as can be seen by the Δ^{++} signal dominating the $\mathrm{p_f}\pi^+$ mass spectrum in figure 5.2. During data taking this type of event is indistinguishable from centrally produced events, and so they must be removed during the analysis of the recorded data. Although genuine $\mathrm{p_s}(\mathrm{K}^+\mathrm{K}^-)\mathrm{p_f}$ systems cannot be produced by the mechanism described above, it is still necessary to remove the Δ^{++} events from the $\pi^+\pi^-$ channel in the selection of the $\mathrm{K}^+\mathrm{K}^-$ channel. The reason for this is that the primary source of contamination to the $\mathrm{K}^+\mathrm{K}^-$ channel is from $\pi^+\pi^-$ central systems, which is made worse if the central $\pi^+\pi^-$ systems are themselves heavily contaminated. To deal with this contamination a cut to remove events with $m_{\mathrm{p_f}\pi^+} < 1{\cdot}5$ GeV/c^2 is applied. The data removed by this cut contains no evidence of K^+K^- events, as is shown in figure 5.4a after the Čerenkov particle identification has been applied.

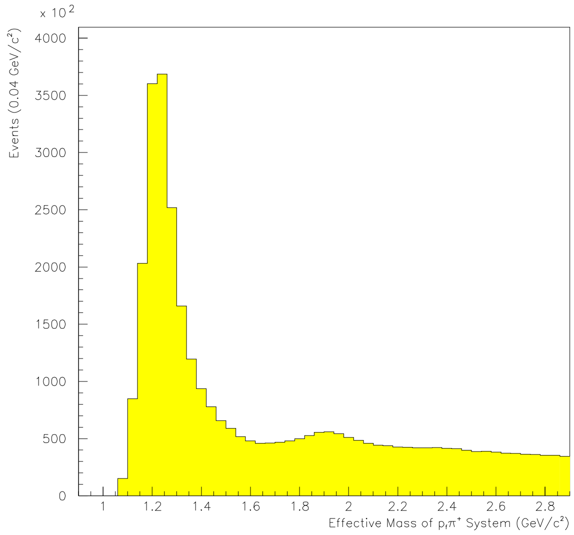

Figure 5.2: The $p_f\pi^+$ mass spectrum for h^+h^- events is contaminated by a prominent Δ^{++} signal.

5.3 Particle Identification

5.3.1 Ehrlich Mass Squared

The quantity *Ehrlich mass squared* (m^2_{Ehrl}) [80] is used to assess the particle content of a central system without the need for a detector to be employed for particle identification. It is calculated for each event using the energy and momentum of the incoming protons, and of the outgoing four tracks (see appendix A). It makes the assumption that the two centrally produced particles have the same mass. Shown in figure 5.3 is the m^2_{Ehrl} distribution for the data obtained by the selection cuts outlined thus far. A peak at the pion mass squared dominates the distribution, while a shoulder at the kaon mass squared provides evidence for a far smaller production of K^+K^- systems.

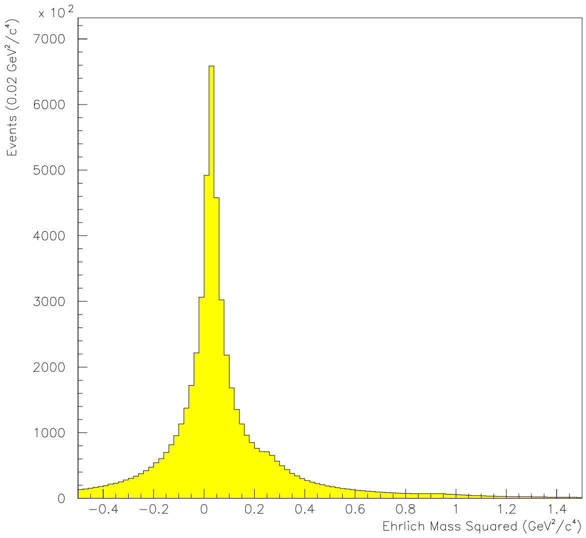

Figure 5.3: The m^2_{Ehrl} distribution after the missing momentum cuts and Δ^{++} cut for $\mathrm{h^+h^-}$ events.

5.3.2 Threshold Čerenkov Detector

The information provided by the threshold Čerenkov counter, Č1, is essential to filter the far more prolific $\pi^+\pi^-$ systems away from the desired $\mathrm{K^+K^-}$ events. It is used for particle identification by exploiting the fact that particles with different masses emit Čerenkov light at different momentum thresholds. During the 1996 run the momentum thresholds for pions, kaons and protons were 7, 25 and 49 GeV/c respectively. The centrally produced kaons were typically in a momentum range of 0 GeV/c to 20 GeV/c, although a lower statistics distribution of kaons extended up to approximately 50 GeV/c. This means that a centrally produced particle can be identified as an ambiguous K/p particle if it is in the momentum range 7 GeV/$c < p <$ 25 GeV/c, and it does not emit Čerenkov light. An event is labelled as an ambiguous $\mathrm{K^+K^-/p\overline{p}}$ event if either one, or both, of the centrally produced particles from an $\mathrm{h^+h^-}$ event is identified as an ambiguous K/p particle, with the additional condition that both particles must be compatible with being a K.

Different methods for incorporating the information from the Čerenkov detector were tested, and the method which gave the cleanest K^+K^- signal was used. This method is outlined as follows:-

1. Each medium momentum track is traced out to locate its $y-z$ position at the Č1 mirrors. This locates which Čerenkov cell the track passes through.
2. Each track is also traced to the hodoscope (HY2) directly behind Č1, to identify which hodoscope element the track passes through.
3. Information from the relevant Čerenkov cell is examined. If a track passes sufficiently close to an adjacent cell, then light is looked for in both cells.
4. If no light is seen in the Čerenkov cell(s) then a co-incidence hit is looked for in the corresponding element of HY2. It is the absence of light in the Čerenkov cell(s) which will identify a K/p particle, and for this reason a co-incidence hit is required as it ensures that the particle does in fact pass through the cell, and does not interact or decay before the Čerenkov system.

The Čerenkov detector enhances the K^+K^- to $\pi^+\pi^-$ ratio greatly, as can be seen from the Ehrlich mass squared distribution of the events selected as ambiguous $K^+K^-/p\overline{p}$ events, shown in figure 5.4b. However, the initial $\pi^+\pi^-$ to K^+K^- ratio is so large that even an efficient Čerenkov detector, such as Č1[1], can only produce a final data set in which the $\pi^+\pi^-$ to K^+K^- ratio is of the order 2:1. In spite of this, the improvement of the signal-to-background ratio is sufficient, and the K^+K^- sample of central events can be selected by placing a cut on m^2_{Ehrl} around the kaon mass squared peak. The selected K^+K^- data sample is given by the Ehrlich mass squared region,

$$0{\cdot}14 \text{ GeV}^2/c^4 < m^2_{\text{Ehrl}} < 0{\cdot}55 \text{ GeV}^2/c^4.$$

[1] The global efficiency of Č1 is found to be 94±1%. The methods by which this has been calculated are described in section 5.8.

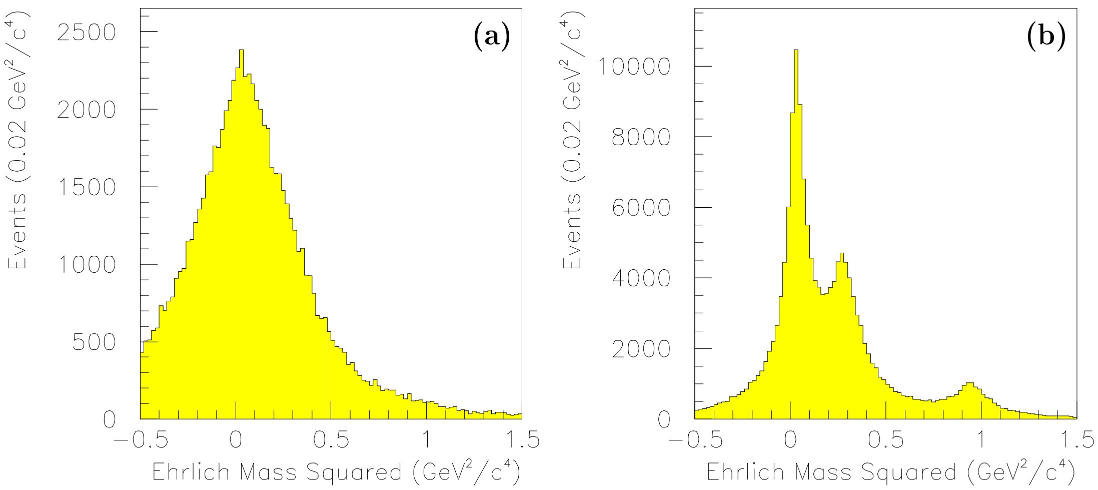

Figure 5.4: After the Čerenkov particle identification, the m^2_{Ehrl} distributions of (a) events removed by the Δ^{++} cut, and (b) events which have been selected as ambiguous $K^+K^-/p\bar{p}$ central systems..

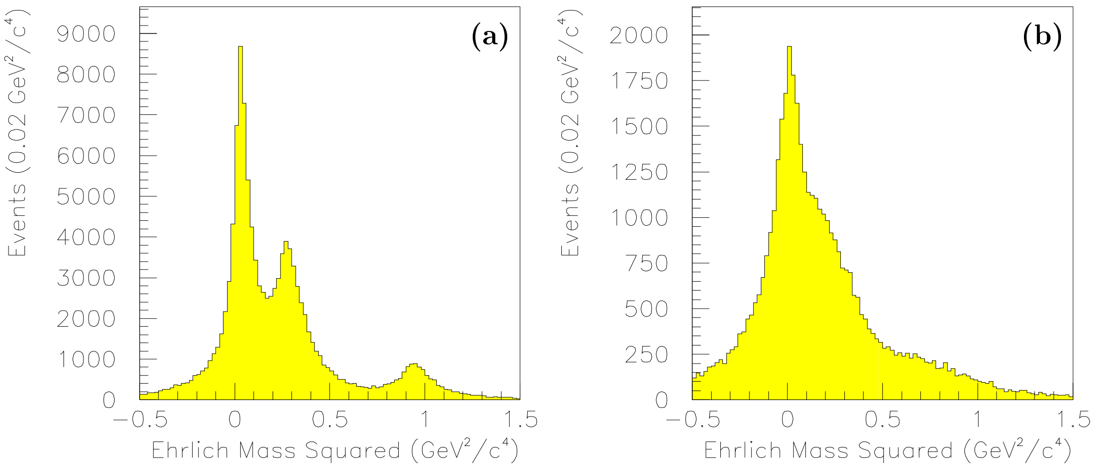

Figure 5.5: The m^2_{Ehrl} distribution for events with (a) a slow left proton, and (b) a slow right proton.

5.4 Trigger Types

The quality of the K^+K^- signal differs greatly according to whether the event is triggered by a left or a right slow proton, as right slow protons are not measured as well as left slow protons. The larger momentum error for slow right protons means that the π and K peaks in the m^2_{Ehrl} distribution merge together, preventing the selection of the K^+K^- channel. Figure 5.5a shows the Ehrlich mass squared for events which triggered on a slow left proton in which the kaon mass squared peak is clearly visible. Events which triggered on a slow right proton are shown in figure 5.5b, the π and K peaks are merged together, preventing the separation of the signal from background by an m^2_{Ehrl} cut. For these reasons only events which triggered on slow left protons are used in the analysis.

5.5 Categories of K^+K^- Systems

It is useful to classify the K^+K^- central systems by the way in which they are identified for the purposes of further cuts. A track is identifiable as a K/p particle if it is in the momentum range of 7 GeV/$c < p <$ 25 GeV/c, let this situation take the symbol $\bullet$. It is also true that a particle cannot be identified as a kaon if it has a momentum of $p <$ 7 GeV/c, or $p >$ 25 GeV/c, let this situation take the symbol $\circ$. A K^+K^- event may be identified by either one, or both tracks being found to be a K/p particle, which leads to three mutually exclusive classes of identification for a K^+K^- event. These three classes have been labelled $K_{\mathrm{I.D.}} = 1$ if the positive track is identified as an ambiguous K/p particle; $K_{\mathrm{I.D.}} = 2$ if the negative track is identified as an ambiguous K/p particle; and $K_{\mathrm{I.D.}} = 3$ if both tracks are identified as ambiguous K/p particles. For clarity the $K_{\mathrm{I.D.}}$ definitions are shown in table 5.1.

Table 5.1: The three identification classes of K^+K^- events.

$K_{I.D.}$	K^+: • K/p Identifiable ∘ K/p Non−Identifiable	K^-: • K/p Identifiable ∘ K/p Non−Identifiable
1	•	∘
2	∘	•
3	•	•

5.6 Diffractive Contamination of the K^+K^- Signal

It is found that the K^+K^- channel requires more stringent cuts on the effective mass of the $p_f\pi$ systems than those already performed for the preliminary selection of the h^+h^- channel. Contamination originates from diffractive events that generate doubly-charged, and neutral baryon excitations from the interactions,

$$\begin{array}{llll} & pp \longrightarrow p_s\pi^-\Delta^{++} & \text{where} & \Delta^{++} \longrightarrow p_f\pi^+, \\ \text{and} & pp \longrightarrow p_s\pi^+(\Delta^0 \text{ or } N^\star) & \text{where} & \Delta^0 \text{ or } N^\star \longrightarrow p_f\pi^-. \end{array}$$

Because of the kinematics of these diffractive events, the samples of data they contaminate are specific to particular $K_{I.D.}$ classes, and so the cuts applied to rectify the problem are also $K_{I.D.}$ dependent.

5.6.1 $K_{I.D.} = 1$ Data

Diffractive events creating neutral baryons such as $N^\star$s and Δ^0s subsequently generate a very fast π^-, which is likely to have a momentum of $p > 25$ GeV/c. If these events are to be misidentified as K^+K^- events then they must be identified by the positive track, and so will fall into the classification $K_{I.D.} = 1$. The $K_{I.D.} = 2$ class of events is not affected by the decay of these neutral baryons, as the negative track associated with them must be in the momentum range 7 GeV/$c < p < 25$ GeV/c.

The $m_{\mathrm{Pf}\pi^-}$ distribution of centrally produced $\mathrm{K}_{\mathrm{I.D.}} = 1$ events peaks at a higher mass than for the $m_{\mathrm{Pf}\pi^-}$ distribution of neutral baryons, due to centrally produced systems having almost no events with a track that has a momentum $p > 25$ GeV/c. This means that π^-s from central events are almost entirely in the momentum range $p < 7$ GeV/c while the π^-s from diffractive contamination are almost entirely in the momentum range of $p > 25$ GeV/c. This mass difference separates the signal from the contamination in the $m_{\mathrm{Pf}\pi^-}$ distribution, and a cut is applied to remove data with,

$$m_{\mathrm{Pf}\pi^-} < 2{\cdot}0 \ \mathrm{GeV}/c^2 \qquad \text{if} \qquad \mathrm{K}_{\mathrm{I.D.}} = 1.$$

The Ehrlich mass squared of the events removed by this cut is shown in figure 5.6a, it can be seen that the quantity of kaons contained is negligible.

5.6.2 $\mathrm{K}_{\mathrm{I.D.}} = 2$ Data

The reciprocal situation applies to the $\mathrm{K}_{\mathrm{I.D.}} = 2$ data sample, in which diffractive contamination originates only from doubly-charged baryons. The very fast π^+ generated by the decay of the Δ^{++} ensures that if these events are misidentified, then it will be as $\mathrm{K}_{\mathrm{I.D.}} = 2$ events. For similar reasons as above, the $m_{\mathrm{Pf}\pi^+}$ distribution peaks at a higher mass for good central $\mathrm{K}^+\mathrm{K}^-$ events than for the $m_{\mathrm{Pf}\pi^+}$ distribution arising from contamination. The cut used to remove this source of contamination is,

$$m_{\mathrm{Pf}\pi^+} < 2{\cdot}0 \ \mathrm{GeV}/c^2 \qquad \text{if} \qquad \mathrm{K}_{\mathrm{I.D.}} = 2.$$

Figure 5.6b shows the Ehrlich mass squared of the data removed by this cut, and as before, the quantity of kaons contained is negligible.

To investigate whether it is simply data with $m_{\mathrm{Pf}\pi^+} < 2{\cdot}0$ GeV/c^2 that is highly contaminated, regardless of its $\mathrm{K}_{\mathrm{I.D.}}$, the m^2_{Ehrl} distribution of the remaining data

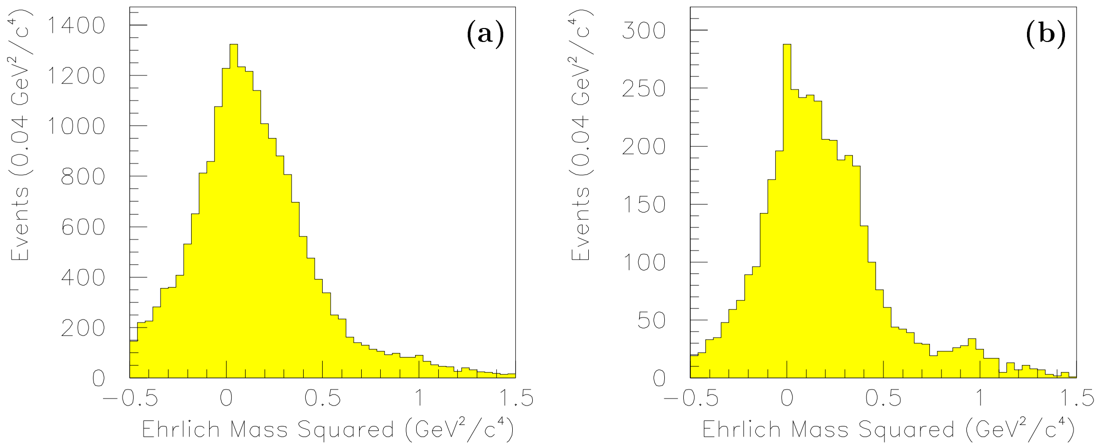

Figure 5.6: The m^2_{Ehrl} distributions for data removed by the cuts (a) $m_{\mathsf{pf}\pi^-} < 2{\cdot}0$ GeV$/c^2$ if $\mathsf{K}_{\mathsf{I.D.}} = 1$, and (b) $m_{\mathsf{pf}\pi^+} < 2{\cdot}0$ GeV$/c^2$ if $\mathsf{K}_{\mathsf{I.D.}} = 2$.

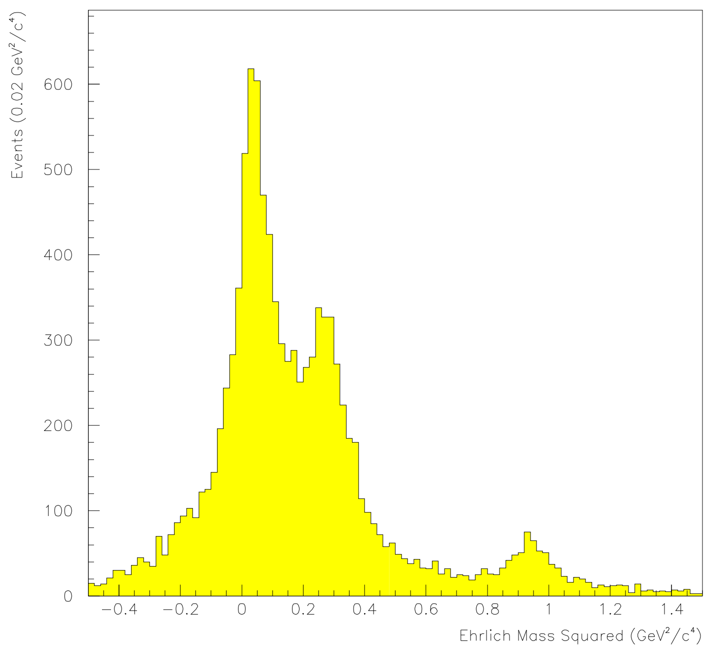

Figure 5.7: The m^2_{Ehrl} distribution of the data with $m_{\mathsf{pf}\pi^\pm} <$ $2{\cdot}0$ GeV$/c^2$ remaining after the mass cuts contains a reasonable $\mathsf{K}^+\mathsf{K}^-$ signal.

with $m_{\mathrm{Pf}\pi^\pm} < 2{\cdot}0$ GeV/c^2 can be examined. These data are shown in figure 5.7 and are of a reasonable quality, they contain a distinct $\mathrm{K^+K^-}$ peak and so are not removed.

5.6.3 $\mathrm{K_{I.D.}} = 3$ Data

Central systems which have been identified as $\mathrm{K^+K^-}$ by both tracks are found to have almost zero $\pi^+\pi^-$ contamination, and require no additional cuts to deal with diffractive contamination.

5.7 Localised Čerenkov Inefficient Regions

If regions exist in the $y - z$ plane of Č1 that are less efficient than average they will contain more misidentified pions than average. Due to the more numerous production of $\pi^+\pi^-$ systems as compared with $\mathrm{K^+K^-}$ systems these inefficient zones will appear as 'hot-spots' of activity. The quality of the data given by these hot-spots can be checked by examining their Ehrlich mass distributions, and comparing them with other regions. By conducting these region-by-region checks in the $y - z$ plane, areas which fall below a reasonable signal-to-background ratio can be identified. There are found to be two inefficient regions in Č1, which are both dependent on the $\mathrm{K_{I.D.}}$ of the event. Positive medium momentum tracks are swept by the magnetic field into the $+y$ half of Č1, and negative medium momentum tracks into the $-y$ half. For this reason the inefficient area in the $+y$ half of Č1 can only contribute contamination to the $\mathrm{K_{I.D.}} = 1$ class of data, and the inefficient area in the $-y$ half can only contribute contamination to the $\mathrm{K_{I.D.}} = 2$ class of data.

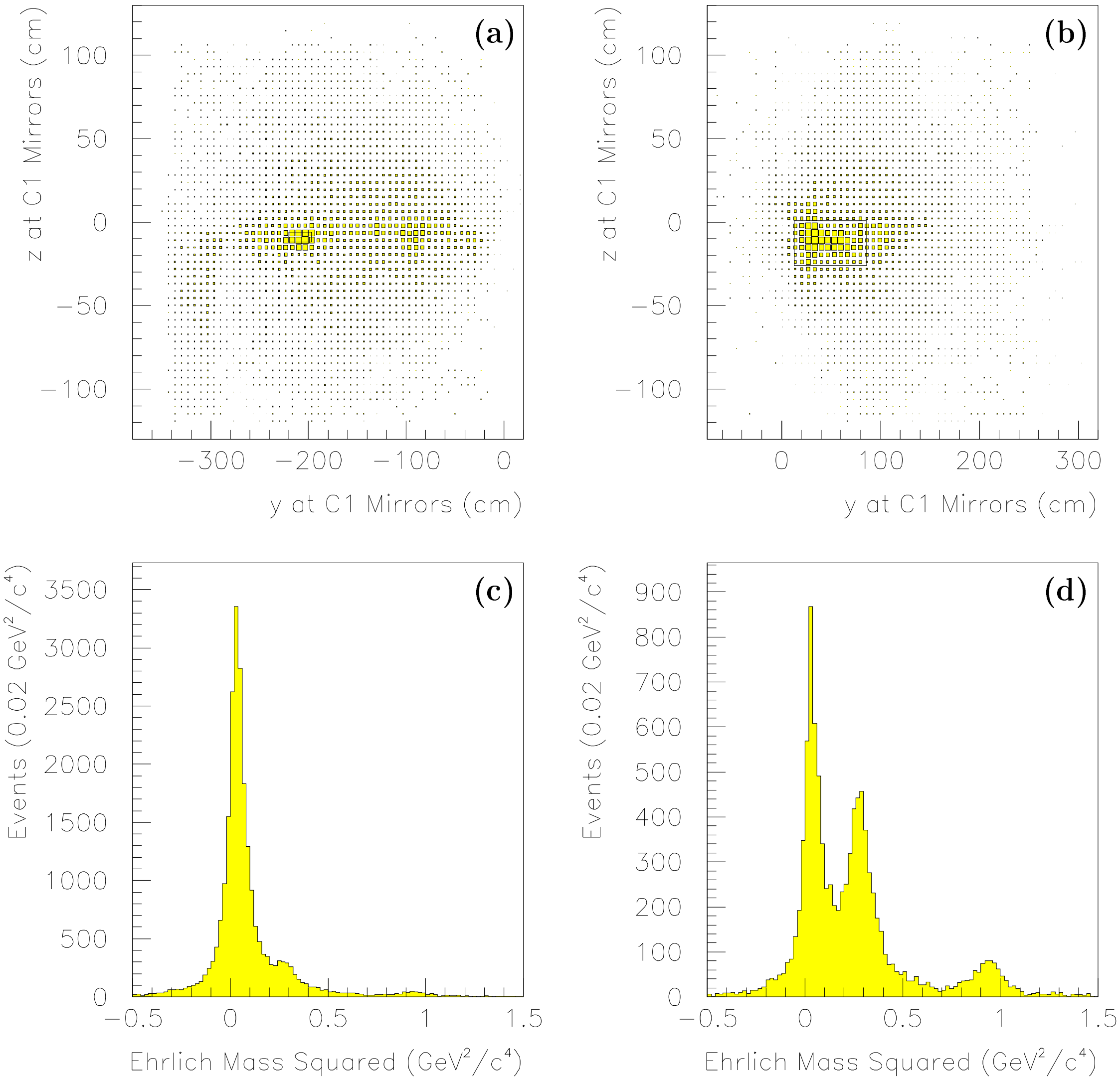

Figure 5.8: The impact of (a) negative, and (b) positive tracks at Č1's mirrors; (c) the m^2_{Ehrl} distributions of the data removed by the area cuts; (d) the additional data which would be removed if the cuts were not $K_{\text{I.D.}}$ dependent.

Data originating from the poor regions are removed by the $\mathrm{K}_{\mathrm{I.D.}}$ dependent cuts,

$$
\begin{array}{lllll}
13 \text{ cm} \leqslant y < 86 \text{ cm}, & -26 \text{ cm} \leqslant z < 1 \text{ cm} & \text{if} & \mathrm{K}_{\mathrm{I.D.}} = 1, \\
-220 \text{ cm} \leqslant y < -197 \text{ cm}, & -12 \text{ cm} \leqslant z < -6 \text{ cm} & \text{if} & \mathrm{K}_{\mathrm{I.D.}} = 2.
\end{array}
$$

Figure 5.8a and 5.8b show the impacts at the Čerenkov mirrors for $\mathrm{K}_{\mathrm{I.D.}} = 2$ and $\mathrm{K}_{\mathrm{I.D.}} = 1$ events respectively, in which the poor regions removed by the cuts are outlined[2]. Figure 5.8c shows the m^2_{Ehrl} distribution of data removed by the cuts. Evidence that the cuts should be applied as a function of $\mathrm{K}_{\mathrm{I.D.}}$ to avoid the unnecessary loss of good data is shown in figure 5.8d which contains the m^2_{Ehrl} distribution of the data that would be additionally removed by the cuts were they not $\mathrm{K}_{\mathrm{I.D.}}$ dependent. The $\mathrm{K}_{\mathrm{I.D.}} = 3$ data is found to have no hot-spots.

5.8 Čerenkov Efficiency

Once the localised inefficient regions of the Čerenkov detector have been removed, the global efficiency of the detector can be calculated. This is done by taking centrally produced $\pi^+\pi^-$ events and tracing them through the detector to find the sub-set which could have been misidentified as a $\mathrm{K}^+\mathrm{K}^-$ system if the Čerenkov system was not perfectly efficient, as this is the class of events which are contaminating the $\mathrm{K}^+\mathrm{K}^-$ data. These events have at least one track passing through Č1 and HY2 in the momentum range 7 GeV/$c < p <$ 25 GeV/c, and pass all of the cuts applied to the $\mathrm{K}^+\mathrm{K}^-$ data. Pions are then intentionally misidentified as kaons by applying a known inefficiency to Č1 which reproduces the observed amount of $\pi^+\pi^-$ contamination. Figure 5.9 shows the Ehrlich mass squared distribution for the $\mathrm{K}^+\mathrm{K}^-$

[2] These cuts might be expected *prima facie* to have strong effects on the angular distributions of the data. However, this aspect of the acceptances has been investigated, and it is found that the cuts cause only a minor bias to the angular distributions. The acceptances are discussed in chapter 6.

events (represented by the open histogram), with the Ehrlich mass squared distribution of the intentionally misidentified $\pi^+\pi^-$ events superimposed (represented by the shaded histogram). Using this method the efficiency of Č1 is found to be $(94 \pm 1)\%$.

This result is consistent with an independent calculation of the efficiency of Č1 by an alternative method. This calculation selected $\pi^+\pi^-$ data by taking events around the pion mass squared peak in the m^2_{Ehrl} distribution, and examined how frequently Čerenkov light was not seen when it was known that a pion was in the appropriate momentum range to have emitted light. This investigation found a compatible efficiency of $(95 \pm 1)\%$.

This results in a data set with very little $\pi^+\pi^-$ contamination under the K^+K^- events. It is shown in section 6.7 that the quantity of $\pi^+\pi^-$ contamination is small, and that the effect of this contamination on the angular distributions of the K^+K^- data is negligible.

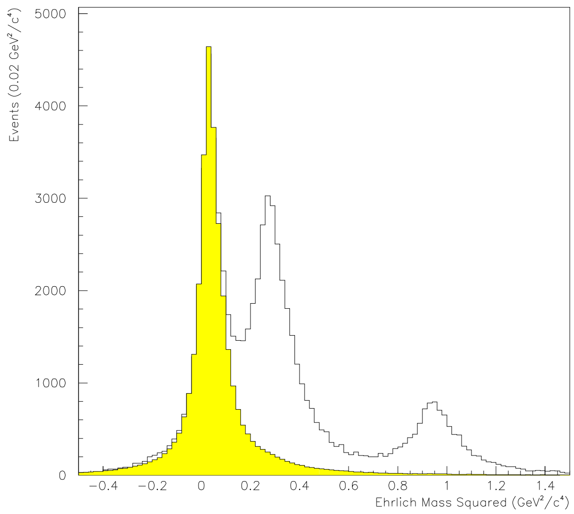

Figure 5.9: The m^2_{Ehrl} distribution for the K^+K^- data is represented by the open histogram. The shaded m^2_{Ehrl} histogram represents the intentionally misidentified $\pi^+\pi^-$ events.

5.9 Mass Spectra of the 1996 K^+K^- Data

The mass spectrum of the K^+K^- data with all of the described cuts applied is shown in figure 5.10a. The mass spectrum, after being acceptance corrected and renormalised to the original number of events, is shown in figure 5.10b. The proportions of the main features of the mass spectrum with masses of $m_{K^+K^-} > 1{\cdot}4$ GeV/c^2 are not greatly altered after acceptance correction. However, the mass spectrum below a mass of $1{\cdot}4$ GeV/c^2 has a progressively increasing weighting factor applied to it as the mass decreases towards threshold. This change in acceptance with mass is as a result of the Čerenkov system. To be able to identify K^+K^- systems it is required that an event must generate at least one medium momentum track of $p \geqslant 7$ GeV/c, and this becomes increasingly difficult to satisfy as the central system becomes lighter and tends towards threshold. The main features of the acceptance corrected K^+K^- mass spectrum are a large threshold enhancement, a peak in the $1{\cdot}5$ GeV/c^2 region, and a shoulder in the $1{\cdot}7$ GeV/c^2 region.

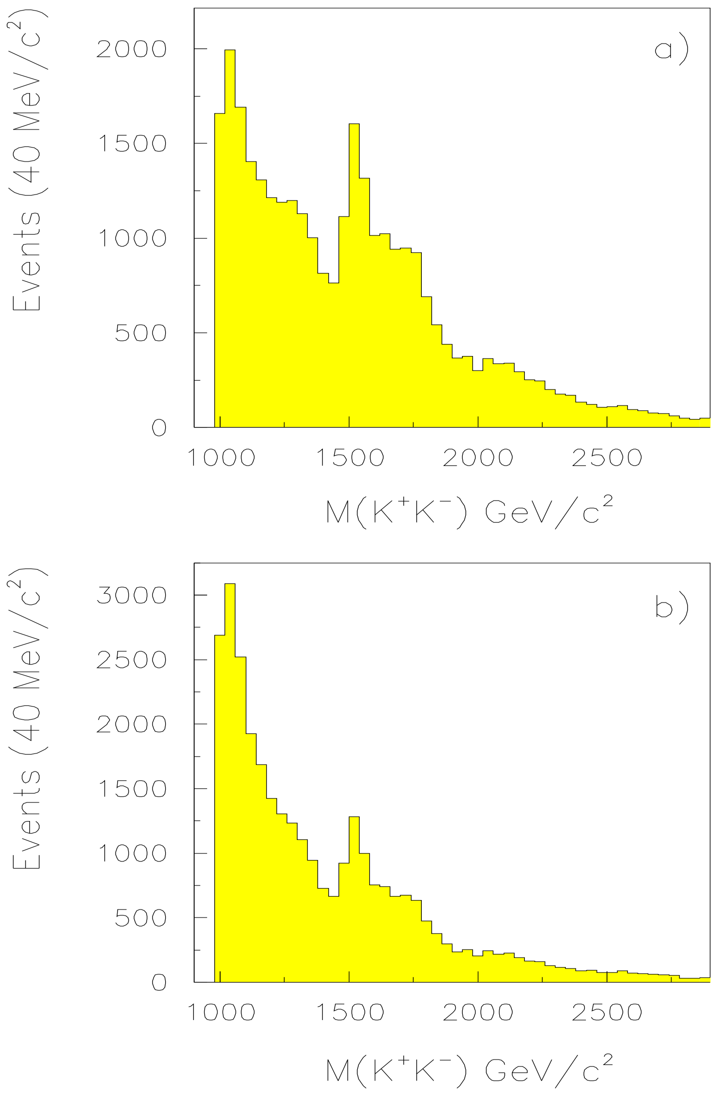

Figure 5.10: (a) The raw K^+K^- mass spectrum and (b) the acceptance corrected K^+K^- mass spectrum renormalised to the original number of events.

Chapter 6

Partial Wave Analysis

6.1 Introduction

This chapter comprises five main topics. (I) It begins by discussing the necessity for the *acceptance correction* of experimental data, it then describes how the acceptance correction is performed for this analysis, and shows the *acceptance tables* used. (II) The treatment of the angular distributions of the data using *moments* is then described, and the acceptance corrected experimental moments of the 1996 K^+K^- data are presented. (III) The *Partial Wave Analysis (PWA)* used is then outlined, and subsequently more fully discussed. (IV) The results of the Monte Carlo studies into the validity of the analysis are then presented, in which the results from PWAs on S-wave phase-space, D_0-wave phase-space, and S-wave phase-space containing resonances of different spins are shown. (V) Finally, the results of the PWA of the 1996 K^+K^- data are presented.

6.2 Acceptance Correction

A general feature of particle physics experiments is the need to simulate the experiment, so that the results obtained from it can be properly interpreted. The simulation, usually called the *Monte Carlo simulation*, is necessary so that biases in the resulting data due to features such as the geometrical acceptances of the detectors, efficiencies, and the specific decay mode under study, can be investigated and properly corrected for. These features can prevent all, or a proportion, of certain classes of events from being observed. The events which are lost have in general different kinematical and angular distributions from the sample which are detected, and so instead of the distributions from the entire set of interactions being recorded, an *acceptance affected* set of distributions are actually observed. In order to perform meaningful analyses on the data, they must first be *acceptance corrected* such that the distributions used in an analysis are those which would be found if the decay products of an event could be measured by an apparatus that did not introduce any biases. The required correction to the data is calculated using a Monte Carlo simulation, which recreates in software the physical experimental situation, and using this technique the proportion of unobserved events, and their characteristics, can be established. The *acceptance* is the ratio of observed events to all events (observed and unobserved), and is used to correct the experimental data. This description of acceptance is of a global scaling factor, but acceptance varies as a function of the parameters describing an interaction. To account for this the acceptance is calculated as a function of the parameters that are relevant to an analysis, such as mass and angular distributions for a mass dependent spin analysis. While it is important that the distributions of parameters not relevant to an analysis match the data as closely as possible, it has been found that it is not necessary to perform the acceptance correction as a function of them.

6.3 Event Generation

The function of a Monte Carlo generator is to create events which reproduce the kinematical distributions of the decay products from real interactions. The method by which this is achieved has been developed by the WA102 collaboration, and is as follows. The beam has a very precise momentum of 450 GeV/c with small, well-measured p_y and p_z distributions, and offsets in the $y-z$ plane at the main vertex position. The Monte Carlo beam is set up with respect to the Ω axes by reproducing the observed distributions and offsets, and by using the known total momentum. The target is represented by a stationary proton while the fast and slow tracks are set up such that after being projected through the spectrometer they reproduce the observed x_{F}, p_y, and p_z distributions of the real fast and slow tracks. The available energy and momentum remaining once the fast and slow tracks have been subtracted from the beam and target is then assigned to the central system, which is decayed isotropically in its rest frame to two particles, each with the mass of a kaon. Only events which possess a $\mathrm{K}^+\mathrm{K}^-$ system within the mass range being considered for the real data ($0{\cdot}9$ GeV/$c^2 < m_{\mathrm{K}^+\mathrm{K}^-} < 2{\cdot}9$ GeV/c^2) are used, and in this way an entire event is generated.

6.4 Geometrical Acceptance

An important component in the calculation of the acceptances is that of the *geometrical acceptance* of the apparatus, which is necessary to correct for biases which arise from the detector not having total spatial coverage. To calculate the geometrical acceptance of the WA102 apparatus, the outgoing particles from each Monte Carlo interaction are projected through the spectrometer to find out if they hit sufficient detectors such that they would be reconstructed. If all of the decay products hit enough detectors for them to be reconstructed, then the event as a whole is geometrically accepted.

A GEANT [82] simulation is performed using a limited data sample to model the spectrometer and investigate the experimental parameters of the apparatus. It is necessary to generate acceptance tables for the spin analysis in at least three dimensions so that the data can be acceptance corrected as a function of mass and two angles, and a large Monte Carlo input data sample is needed to produce these tables. For this large quantity of data a GEANT simulation has been found to require a prohibitively long computer processing time, and to overcome this problem a less computer intensive 'two-step' approach has been developed by the WA102 collaboration which is designed to reduce the number of times that the particularly CPU-intensive process of tracing a charged particle through the Ω magnetic field must be performed. By using this two-step method the number of tracing stages necessary for the 500 million Monte Carlo events to be generated is of the order of 10^6, whereas a full simulation would require some 10^9 tracing stages.

Firstly *look-up tables* are made for each particle that contain information about their individual geometrical acceptances. This is done for the slow proton, for example, by the following method. A slow proton is kinematically defined by its momentum, polar and azimuthal angles with respect to the Ω axes, and vertex position in the x-direction $(p_{\mathrm{S}}, \theta_{\mathrm{S}}, \phi_{\mathrm{S}}, v_x)$. A slow proton defined by this set of kinematical variables is traced out through the Ω magnetic field to ascertain whether or not it is geometrically accepted. One of the variables is then incremented to a new value and the process is repeated until all of the defined parameter space has been explored. In this way, a binary look-up table of 'yes/no' geometrical acceptance decisions is generated. The parameter space over which the tracing for each decay particle is performed can be reduced by setting the acceptance decision to 'no' for particles with kinematical parameters that can never be accepted, *e.g.* a slow proton emitted in the negative y-direction will never be accepted as a slow-left proton, and so the acceptance decision for this class of slow protons can immediately be set to 'no' when creating the slow-left look-up table. Similar methods are used for the fast, positive, and negative tracks, using the relevant kinematical variables in each case, and in this way look-up tables are generated for each outgoing particle.

The look-up tables are cross-checked by passing data from real events through them to ensure that data which has already been accepted by the experiment will be re-accepted by the look-up tables. Due to small approximations introduced by the finite binning of the kinematical variables describing a track, and the fact that not every kinematical parameter which describes a track is included, not all real data are accepted. The width of the bins and the number of kinematical variables used for the look-up tables are defined such that ~99% of the experimental data associated with any given track will be re-accepted by the look-up table for that track. The data that is rejected is lost from the edges of the relevant particle detectors.

6.5 Definition of the Moments

Moments are experimentally determinable quantities which are defined as the expectation values of the Wigner $\mathcal{D}$-functions $\mathcal{D}^{\mathrm{L}}_{\mathrm{M0}}(\Omega)$ [83], where Ω represents the scattering angles θ and ϕ of the central system,

$$\sqrt{4\pi}\,\mathrm{t}(\mathrm{LM}) \;\equiv\; \langle \mathcal{D}^{\mathrm{L}}_{\mathrm{M0}}(\Omega) \rangle \;=\; \int \mathrm{d}\Omega\, \mathrm{I}(\Omega)\, \mathcal{D}^{\mathrm{L}}_{\mathrm{M0}}(\Omega).$$

The axes with respect to which the scattering angles are defined are akin to the Gottfried-Jackson axes [84] defined for peripheral interactions. In the peripheral interaction,

$$\pi^- \mathrm{p} \;\longrightarrow \mathrm{nK}^+\mathrm{K}^-,$$

shown in figure 6.1a, the Gottfried-Jackson axes are defined such that the z-axis is taken to be along the beam direction in the $\mathrm{K}^+\mathrm{K}^-$ rest frame, the y-axis is taken to be along the production normal in the overall centre-of-mass frame, and the x-axis is the cross-product $y \times z$. Central production can be thought of in very similar terms, as represented in figure 6.1b, and if the Pomeron from either the fast or slow vertex in central production is considered in place of the π^- beam in the peripheral interaction, then the axis definition translates directly from one process to the other. Using the Pomeron from either the fast vertex or the slow vertex produces the same results, and this analysis uses the Pomeron from the fast vertex. In the case of central production the z-axis is taken to be along the direction of the exchanged particle from the fast proton in the rest frame of the central system, the y-axis is taken to be along the production normal in the overall centre-of-mass frame, and the x-axis is defined to be the cross-product $y \times z$. These axes are used to define the polar scattering angle θ and the azimuthal scattering angle ϕ, as depicted in figure 6.1c.

6.6 Acceptance Tables

Monte Carlo data are generated and passed through a detector simulation program which applies the effects due to geometrical acceptance and other factors, including each of the previously discussed cuts that have been applied to the real data. The mass of each event and its angular distributions are recorded both before and after being passed through the detector simulation package. The acceptance tables are then produced by dividing the output distributions by the input distributions, and are calculated as a function of K^+K^- mass in bins of 100 MeV/c^2, and of the spin analysis angles[1] $\cos\theta$ in bins of 0·2, and ϕ in bins of $\frac{2\pi}{20}$ radians. The acceptance tables resulting from 500 million generated events are displayed in figures 6.2 and 6.3, where it can be seen that the acceptances vary smoothly.

The generation of the acceptance tables is indispensable for the spin analysis, and it also provides an opportunity to observe the effects of different cuts upon the data, and to see in which way, and to what extent, they may bias the data. Although the biases which have been introduced to the real data are removed by the acceptance

[1] The spin analysis angles, and the axes which they are defined with respect to, are described in section 6.5.

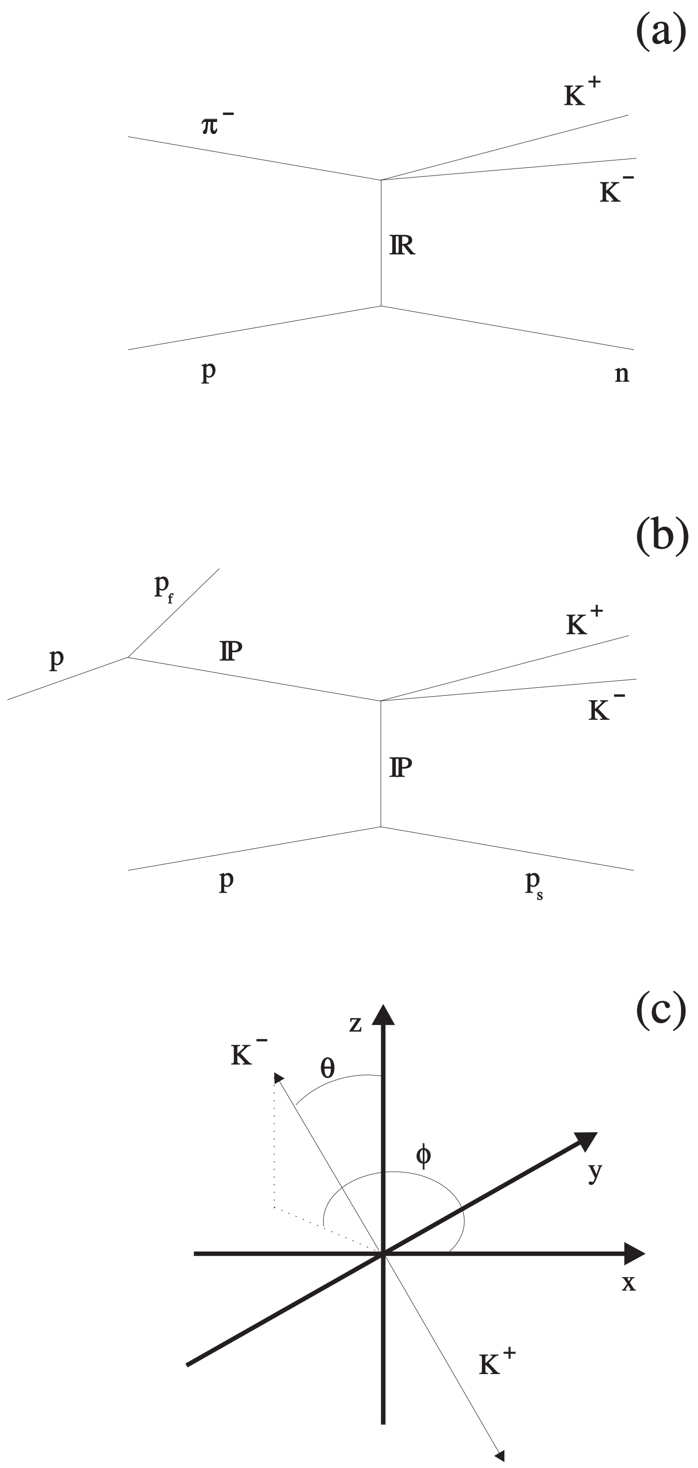

Figure 6.1: Gottfried-Jackson axes defined (a) for peripheral interactions and (b) for central production interactions. (c) The polar (θ) and azimuthal (ϕ) scattering angles of the K^+K^- system.

correction, this investigation is useful as it is undesirable to introduce large biases to the data through the application of cuts. The cuts which cause the greatest effects on the acceptance tables are the pπ mass cuts introduced to remove contamination from diffractive events. The $m_{\mathrm{pf}\pi^+}$ cuts of $m_{\mathrm{pf}\pi^+} < 1{\cdot}5$ GeV/c^2 (for all data), and $m_{\mathrm{pf}\pi^+} < 2{\cdot}0$ GeV/c^2 (for $\mathrm{K_{I.D.}}$=2 data) cause a reduced acceptance at $\cos\theta{\sim}-1$ which becomes more apparent at higher $\mathrm{K^+K^-}$ masses. Conversely, the $m_{\mathrm{pf}\pi^-}$ cut of $m_{\mathrm{pf}\pi^-} < 2{\cdot}0$ GeV/c^2 (for $\mathrm{K_{I.D.}}$=1 data) causes a reduction in the acceptance at $\cos\theta{\sim}+1$, which also becomes more apparent at higher $\mathrm{K^+K^-}$ masses. Other cuts have smaller effects upon the final acceptance tables. Notably, the $\mathrm{K_{I.D.}}$ dependent cuts in the $y-z$ plane at the Čerenkov mirrors, which could appear *prima facie* to be strongly correlated with the spin analysis angles $\cos\theta$ and ϕ, have only a minor effect on the angular distributions of the acceptance tables, and hence apply only a minor bias to the angular distributions of the real data. If the overall acceptance as a function of the angular distributions is considered, then it may be noted that the greatest difference in the acceptance of $\cos\theta$ in a single mass-bin (while integrating over the acceptance in ϕ) is a factor of ~2, and the greatest difference in the acceptance of ϕ in a single mass-bin (while integrating over the acceptance in $\cos\theta$) is a factor of ~4.

To investigate the validity of the acceptance tables, Monte Carlo data have been generated with various initial conditions, passed through a detector simulation package, and then acceptance corrected using the same acceptance tables as those applied to the real data. The resulting data are then examined to discover if they have been properly restored to their original angular distributions. The results from this investigation show that the angular distributions of the Monte Carlo data are properly corrected with some small errors introduced. This can be seen by studying the acceptance corrected *moments*. The investigation also shows that the *partial waves* contributing to a mass spectrum can be correctly extracted, again with some error introduced, which is seen from the results of *partial wave analysis* on the Monte Carlo data. The results of this investigation are shown in section 6.12 after the moments and partial wave analysis have been discussed.

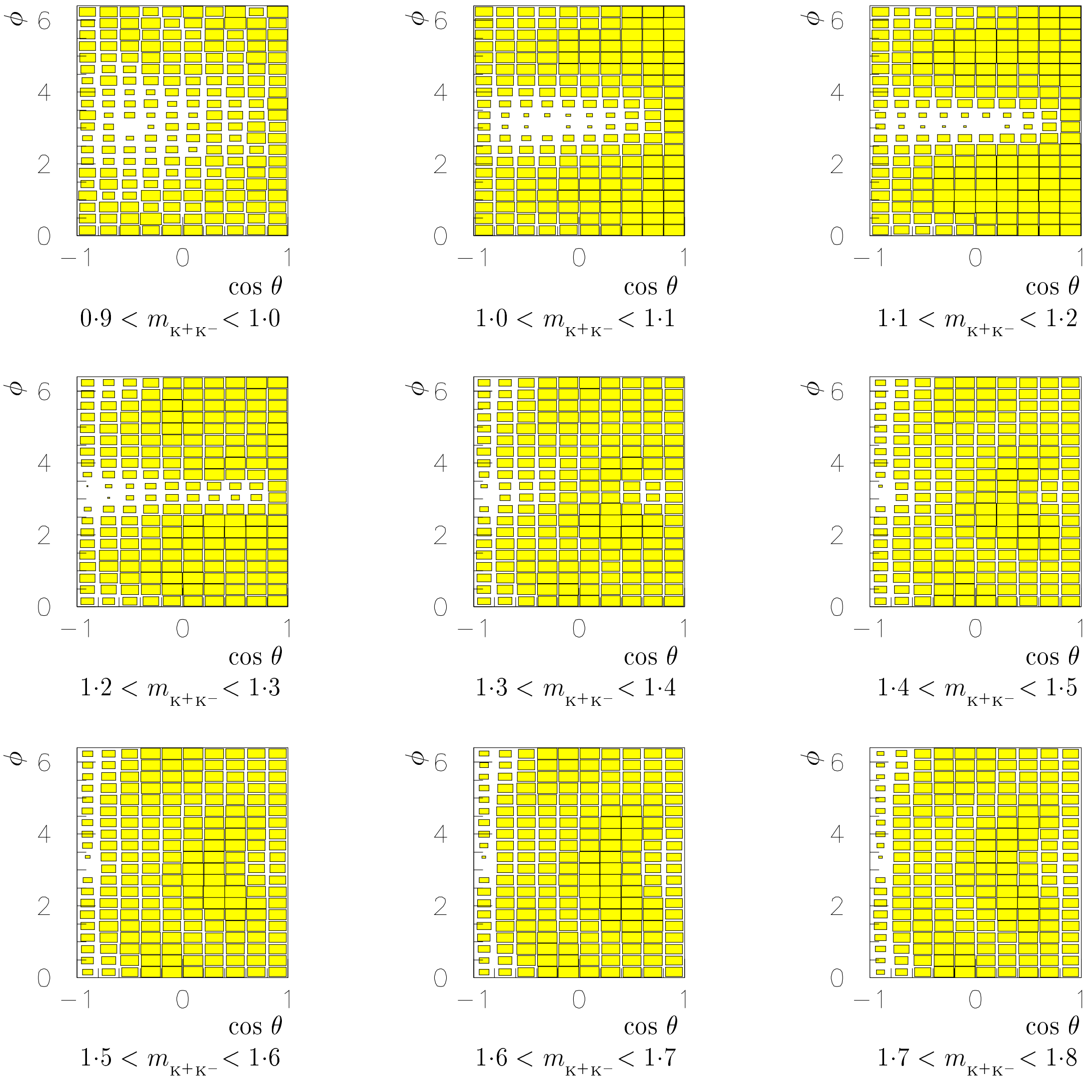

Figure 6.2: Acceptance tables for $\cos\theta$ and ϕ as a function of K^+K^- mass in GeV/c^2.

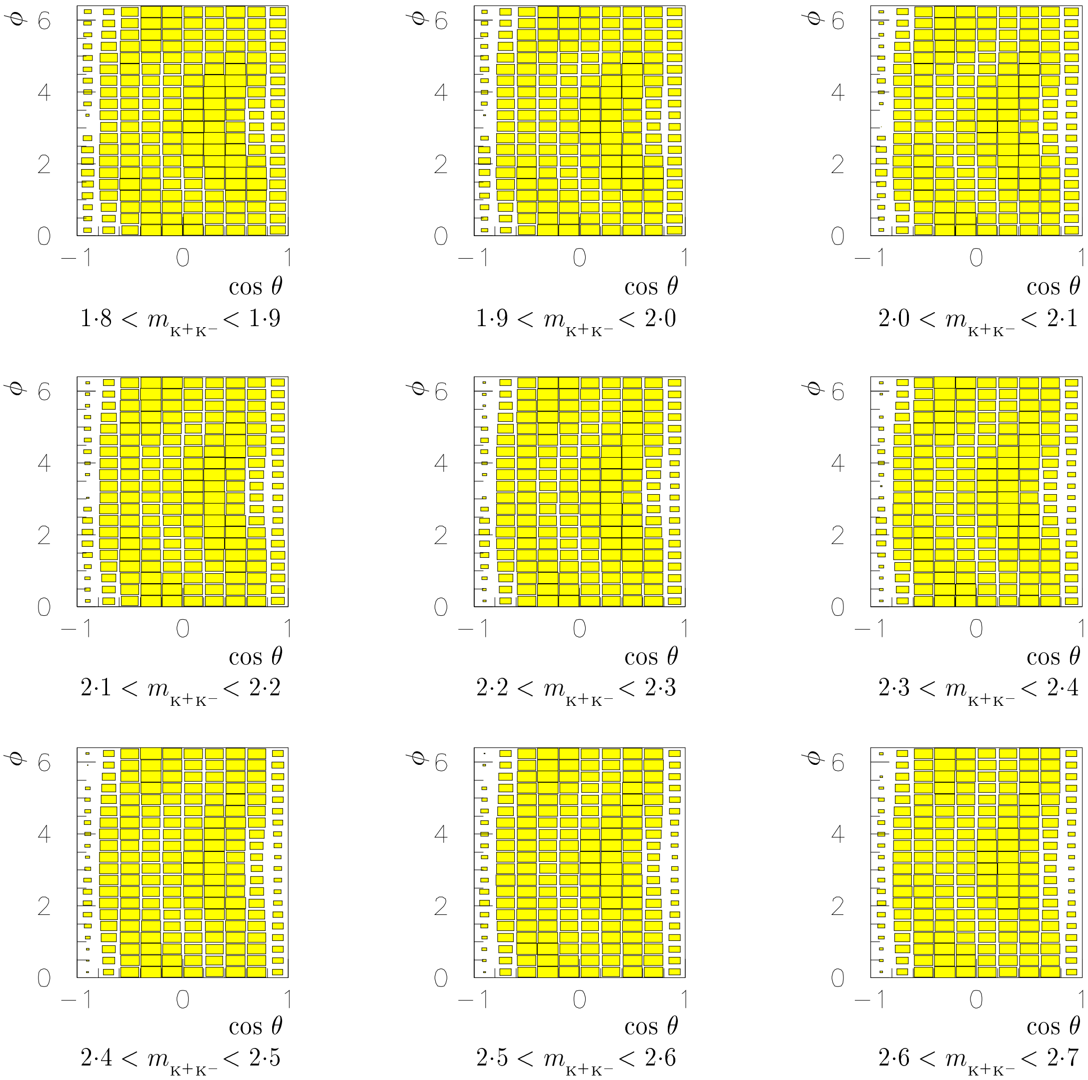

Figure 6.3: Acceptance tables for $\cos\theta$ and ϕ as a function of K^+K^- mass in GeV/c^2.

6.7 Moments of the 1996 K^+K^- Data

The acceptance corrected moments of the K^+K^- data are shown in figures 6.4 and 6.5 where the K^+K^- data are represented by the symbol $\diamond$. The $\pi^+\pi^-$ contamination calculated from the investigation described in section 5.8 is also shown and is represented by the symbol $\bullet$. The figures containing the moments have abscissa representing the mass of the K^+K^- system in units of MeV/c^2. This convention is generally used for the subsequent figures containing the moments and partial waves. The effect of the $\pi^+\pi^-$ contamination is small or negligible in all moments, with the exception of the t(21) moment. Although the activity in this moment is clearly due to the contamination, the total level of activity is only small. The effect of subtracting the $\pi^+\pi^-$ contamination from the K^+K^- moments has been investigated, and the difference made to the following angular analysis is found to be negligible. The t(00) moment reproduces the mass spectrum as it should, and t(20) is the only other moment displaying appreciable activity. Higher moments with $L > 4$ and/or $M > 2$ are shown in figure 6.6, they display little or no structure or activity, and are consistent with zero within errors. Still higher moments in L and M (not shown) are also consistent with zero within errors.

6.8 Description of the Partial Wave Analysis

The Partial Wave Analysis (PWA) may be outlined as follows. In order to extract the partial waves composing the K^+K^- mass spectrum a PWA is performed on the angular distributions of the acceptance corrected experimental data. A set of partial waves corresponds to a set of moments, and the initial objective of the PWA is to calculate the set of partial waves which correspond to moments that best describe the experimental moments. This is done by using an iterative process which minimises the difference between the two sets of moments, a process which is performed independently for each mass-bin. The PWA, however, inherently contains math-

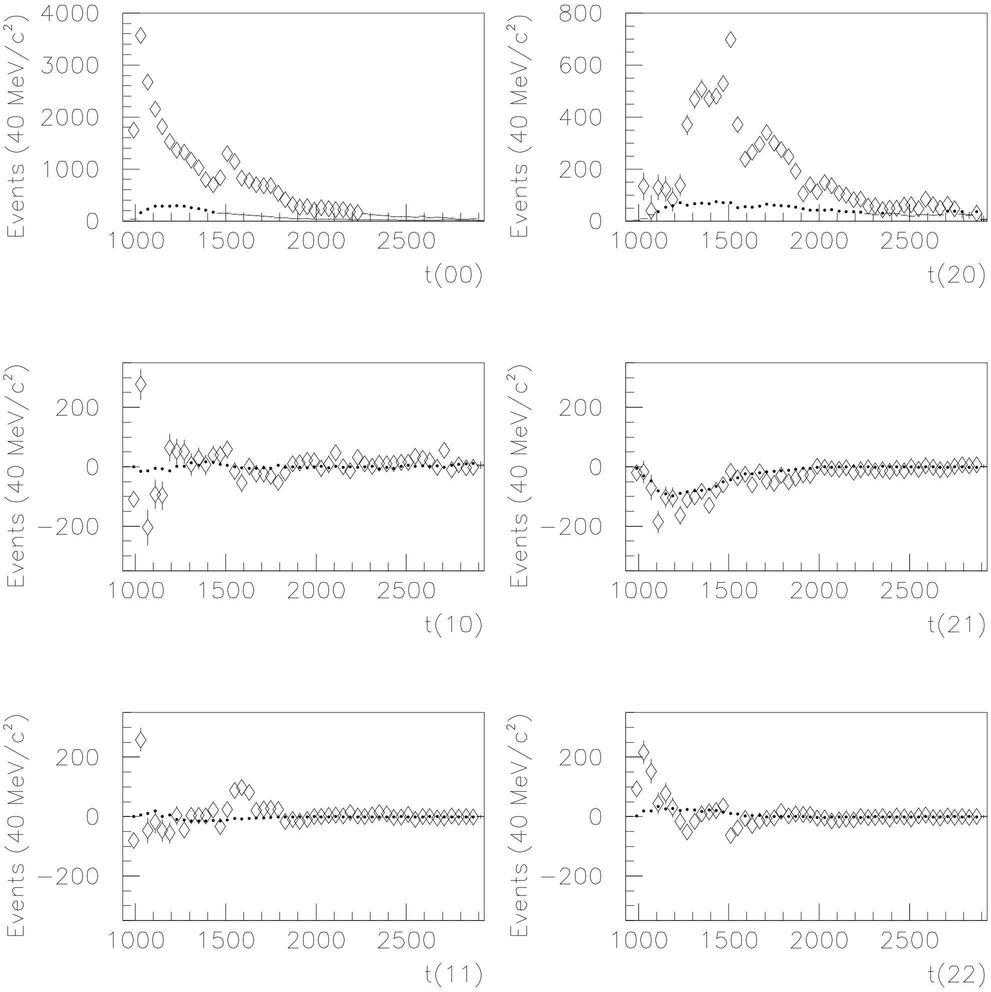

Figure 6.4: Acceptance corrected experimental moments for 1996 K^+K^- data ($\diamond$), with contamination from $\pi^+\pi^-$ systems ($\bullet$) shown.

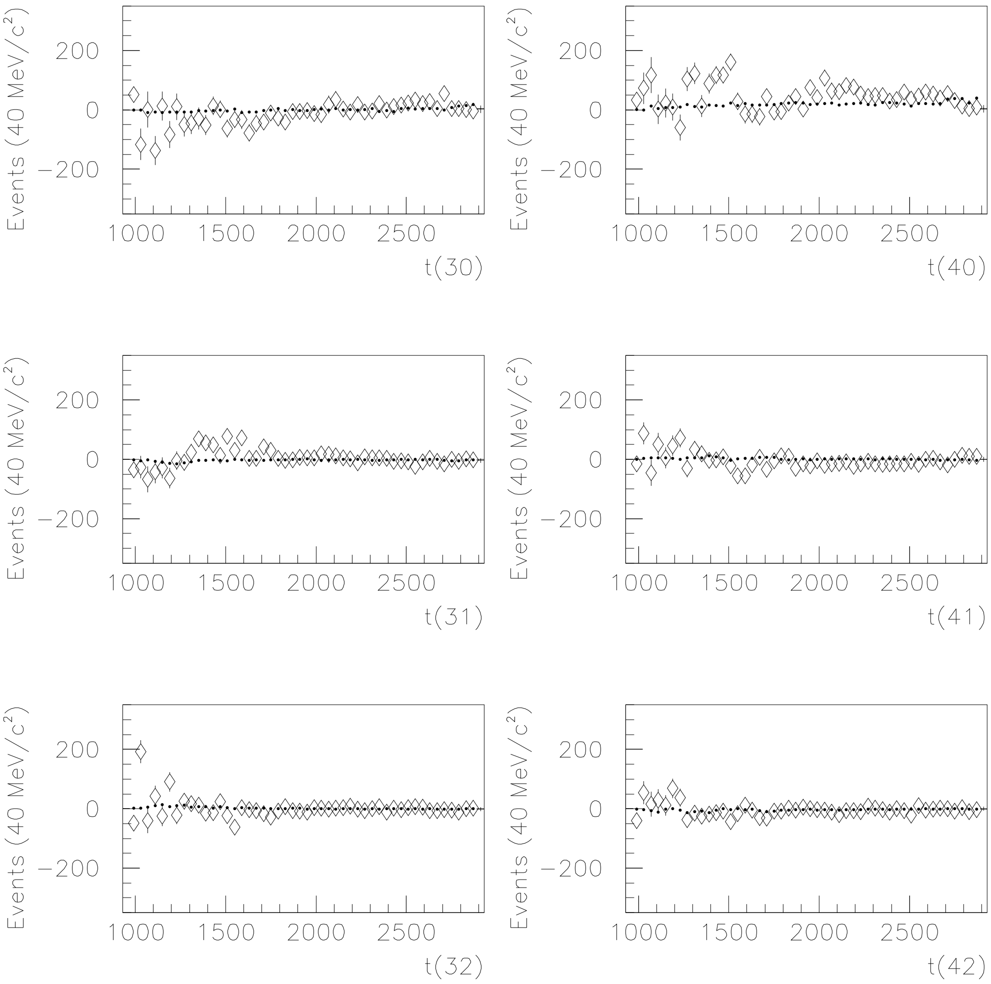

Figure 6.5: Acceptance corrected experimental moments for 1996 K^+K^- data ($\diamond$), with contamination from $\pi^+\pi^-$ systems ($\bullet$) shown.

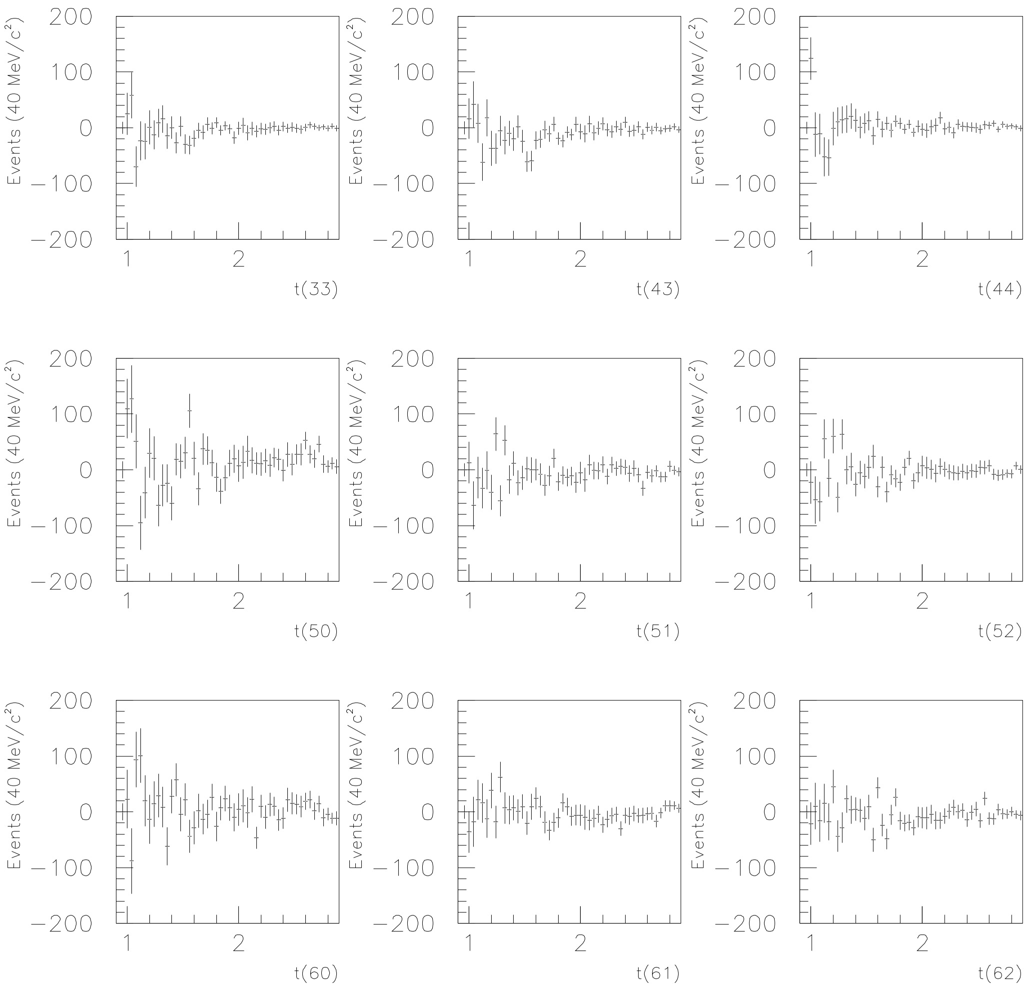

Figure 6.6: Acceptance corrected moments with L > 4 and/or M > 2 show little activity and are consistent within errors with zero.

ematically ambiguous solutions of partial waves, of which there are eight in this analysis. The solution resulting from the minimisation is dubbed the 'nominal' solution, and the ambiguous solutions are generated from the nominal solution. Once generated, the eight solutions must also be properly linked together from mass-bin to mass-bin, as it is not known *a priori* which solution in any given mass-bin should follow a particular solution in the previous mass-bin. This is achieved by linking together the roots of a complex polynomial equation governing the ambiguities, and applying the same linking to the eight sets of partial wave solutions to obtain eight sets of properly linked ambiguous solutions. The ambiguous sets of partial waves correspond to the same set of moments, and therefore provide identical descriptions of the data from which the genuine set is mathematically indeterminable. This problem is dealt with by applying physical constraints to identify the genuine solution.

This section continues by describing the fitting of the experimental moments, section 6.9 then describes the origin of the ambiguities and section 6.10 describes their calculation for this analysis. The linking of the solutions is discussed in section 6.11, and the application of the physical constraints to select the genuine solution is demonstrated in section 6.12 where the results of Monte Carlo simulations that have been used to investigate the validity of the analysis are presented.

As it has been shown that the experimental moments with M > 2 and/or L > 4 are consistent with zero, it is known that only S, P, and D-waves with helicities of $|m| \leqslant 1$ contribute to the K^+K^- mass spectrum. With these considerations incorporated into the PWA there are twelve potentially non-zero moments, the set $\{t(LM)\}$ being,

$$\begin{array}{c} t(00),\ t(20),\ t(30),\ t(40), \\ t(10),\ t(21),\ t(31),\ t(41), \\ t(11),\ t(22),\ t(32),\ t(42). \end{array}$$

Parity conservation in the strong interaction allows the waves of the PWA to be defined within the reflectivity basis [85]. In this basis the waves are given by the sum of two non-interfering terms corresponding to positive and negative values of reflectivity. Waves with helicities of $|m| = 1$ may be of either positive or negative reflectivity, whereas waves with $m = 0$ may only be of negative reflectivity. This yields the two sets of waves below.

Negative Reflectivity ($\epsilon = -$):		S_0 P_0 P_- D_0 D_-
Positive Reflectivity ($\epsilon = +$):		P_+ D_+

The waves are complex and so correspond to fourteen parameters. For both reflectivities the phase of one wave in the set is fixed to zero as a reference, the waves used are S_0 and P_+, which reduces the number of free parameters to twelve. Equations 6.1 give the relations between the moments and partial waves [86, 87] from which the twelve parameters describing the waves can be found by simultaneously solving for a given set of moments $\{\mathrm{t(LM)}\}$. The waves represented in 6.1 are complex variables, and the notation used is such that $\mathrm{S}_0^2 = \mathrm{S}_0\mathrm{S}_0^\star$, and $\mathrm{S}_0\mathrm{P}_0 = \mathcal{R}e\,\{\mathrm{S}_0\mathrm{P}_0^\star\}$.

$$
\begin{aligned}
\sqrt{4\pi}\,\mathrm{t}(00) &= \mathrm{S}_0^2 + \mathrm{P}_0^2 + \mathrm{P}_-^2 + \mathrm{D}_0^2 + \mathrm{D}_-^2 + \mathrm{P}_+^2 + \mathrm{D}_+^2 \\
\sqrt{4\pi}\,\mathrm{t}(10) &= 2\mathrm{S}_0\mathrm{P}_0 + \frac{4}{\sqrt{5}}\mathrm{P}_0\mathrm{D}_0 + 2\sqrt{\frac{3}{5}}(\mathrm{P}_-\mathrm{D}_- + \mathrm{P}_+\mathrm{D}_+) \\
\sqrt{4\pi}\,\mathrm{t}(11) &= \sqrt{2}\mathrm{S}_0\mathrm{P}_- + 2\sqrt{\frac{3}{10}}\mathrm{P}_0\mathrm{D}_- - \frac{2}{\sqrt{10}}\mathrm{P}_-\mathrm{D}_0 \\
\sqrt{4\pi}\,\mathrm{t}(20) &= 2\mathrm{S}_0\mathrm{D}_0 + \frac{2}{\sqrt{5}}\mathrm{P}_0^2 - \frac{1}{\sqrt{5}}(\mathrm{P}_-^2 + \mathrm{P}_+^2) + \frac{2}{7}\sqrt{5}\mathrm{D}_0^2 + \frac{\sqrt{5}}{7}(\mathrm{D}_-^2 + \mathrm{D}_+^2) \\
\sqrt{4\pi}\,\mathrm{t}(21) &= \sqrt{2}\mathrm{S}_0\mathrm{D}_- + 2\sqrt{\frac{3}{10}}\mathrm{P}_0\mathrm{P}_- + \frac{\sqrt{10}}{7}\mathrm{D}_0\mathrm{D}_- \\
\sqrt{4\pi}\,\mathrm{t}(22) &= \sqrt{\frac{3}{10}}(\mathrm{P}_-^2 - \mathrm{P}_+^2) + \frac{1}{7}\sqrt{\frac{15}{2}}(\mathrm{D}_-^2 - \mathrm{D}_+^2) \qquad (6.1) \\
\sqrt{4\pi}\,\mathrm{t}(30) &= \frac{6}{\sqrt{35}}(\sqrt{3}\mathrm{P}_0\mathrm{D}_0 - \mathrm{P}_-\mathrm{D}_- - \mathrm{P}_+\mathrm{D}_+) \\
\sqrt{4\pi}\,\mathrm{t}(31) &= 2\sqrt{\frac{3}{35}}(2\mathrm{P}_0\mathrm{D}_- + \sqrt{3}\mathrm{P}_-\mathrm{D}_0)
\end{aligned}
$$

$$\sqrt{4\pi}\,\mathrm{t}(32) \;=\; 2\sqrt{\frac{3}{14}}(\mathrm{P_-D_-} \;-\; \mathrm{P_+D_+})$$

$$\sqrt{4\pi}\,\mathrm{t}(40) \;=\; \frac{6}{7}\mathrm{D}_0^2 \;-\; \frac{12}{21}(\mathrm{D}_-^2 \;+\; \mathrm{D}_+^2)$$

$$\sqrt{4\pi}\,\mathrm{t}(41) \;=\; \frac{6}{7}\sqrt{\frac{5}{3}}\mathrm{D_0D_-}$$

$$\sqrt{4\pi}\,\mathrm{t}(42) \;=\; \frac{\sqrt{10}}{7}(\mathrm{D}_-^2 \;-\; \mathrm{D}_+^2)$$

The relations show that the t(4M) moments have contributions from D-wave only, and this is an early indication that the $\mathrm{K^+K^-}$ mass spectrum contains only a limited quantity of D-wave as the experimental t(4M) moments are generally very small. This is true even in the 1·5 GeV/c^2 region where the greatest amount of activity in the t(4M) moments is seen. It is particularly noteworthy that the t(4M) moments are all consistent with zero in the 1·7 GeV/c^2 region. The method used to extract the set of partial waves which best describe the data involves choosing an initial set of partial waves, calculating the moments that the set of waves correspond to, and comparing these moments with the experimental moments. The set of moments that most closely describes the experimental moments is arrived at by altering the set of partial waves iteratively such that $-\ln\mathcal{L}$ in equation 6.2 is minimised, the minimisation is executed using the CERN minimisation package MINUIT [88].

$$-\ln\mathcal{L} = -\sum_{i=1}^{N}\ln \mathrm{I}(\Omega_i) + \sum_{\mathrm{LM}}\mathrm{t(LM)\,acc.} \qquad [89,\ 90] \qquad (6.2)$$

N is the number of experimental events in a given mass-bin, I(Ω) is the angular distribution where $\Omega = \{\cos\theta, \phi\}$, and acc. is the acceptance for a given $m_{\mathrm{K^+K^-}}$ and Ω. The minimisation is performed on an event-by-event basis, and is applied to each 40 MeV/c^2 mass-bin independently.

In this way the partial waves that provide the best fit to the data are found. However, the waves resulting from the best fit to the experimental moments are not unique, and do not yet provide a physical solution to the data. The mathematical ambiguities of the solution are an inherent part of the analysis, and stem from the fact that more than one set of partial waves can generate the same set of moments.

6.9 Origin of Ambiguities in the Partial Waves

The angular distribution of a set of data ($I(\Omega)$) may be written [85] in terms of the f-functions, $f_{\mathrm{M}}(\theta)$.

$$I(\Omega) = \frac{1}{4\pi}[f_0(\theta) + 2f_1(\theta)\cos\phi + 2f_2(\theta)\cos(2\phi)] \tag{6.3}$$

The f-functions are experimentally measurable quantities, and are completely defined by a given set of moments $\{\mathrm{t(LM)}\}$. The angular distribution may also be expressed in terms of the squares of the overall amplitude of the interaction ($^{(\epsilon)}U(\Omega)$) in the reflectivity basis.

$$I(\Omega) = |^{(-)}U(\Omega)|^2 + |^{(+)}U(\Omega)|^2 \tag{6.4}$$

The overall amplitudes are defined by the h-functions, $h_\epsilon(\theta)$, and are given by,

$$\begin{aligned} ^{(-)}U(\Omega) &= \frac{1}{\sqrt{4\pi}}[h_0(\theta) + \sqrt{2}h_-(\theta)\cos\phi], \\ ^{(+)}U(\Omega) &= \frac{1}{\sqrt{4\pi}}[\sqrt{2}h_+(\theta)\sin\phi]. \end{aligned} \tag{6.5}$$

The h-functions contain the partial waves to be measured. By comparing the two expressions for the angular distributions the equalities 6.6 can be formed.

$$\begin{aligned} f_0(\theta) &= |h_0(\theta)|^2 + |h_-(\theta)|^2 + |h_+(\theta)|^2, \\ f_1(\theta) &= \sqrt{2}\mathcal{R}e\{h_0(\theta)h_-^\star(\theta)\}, \end{aligned} \tag{6.6}$$

$$f_2(\theta) = \frac{1}{2}\{|h_-(\theta)|^2 - |h_+(\theta)|^2\}.$$

The waves of positive reflectivity may then be eliminated by combining $f_0(\theta)$ and $f_2(\theta)$, and modifying $f_1(\theta)$, which yields,

$$f_a(\theta) \equiv f_0(\theta) + 2f_2(\theta) = |h_0(\theta)|^2 + |\sqrt{2}h_-(\theta)|^2, \tag{6.7}$$
$$f_b(\theta) \equiv 2f_1(\theta) = 2\mathrm{Re}\{h_0(\theta)\sqrt{2}h_-^\star(\theta)\}.$$

If $g(\theta)$ is defined such that,

$$g(\theta) = \frac{1}{\sqrt{2}}[h_0(\theta) + \sqrt{2}h_-(\theta)], \tag{6.8}$$
$$g(-\theta) = \frac{1}{\sqrt{2}}[h_0(\theta) - \sqrt{2}h_-(\theta)],$$

then the functions $f_a(\theta)$ and $f_b(\theta)$ can be defined such that,

$$f_a(\theta) = |g(\theta)|^2 + |g(-\theta)|^2, \tag{6.9}$$
$$f_b(\theta) = |g(\theta)|^2 - |g(-\theta)|^2.$$

For convenience in the ambiguity analysis, reference [85] expresses the functions in terms of the variable u, where $u = \tan(\frac{1}{2}\theta)$, and writes that the function $g(u)$ is a polynomial in u of the order $2l_m$, where l_m is the maximum value of l. This means that there are $2l_m$ roots of the function $G(u)$ containing the partial waves, where

$$G(u) = (1+u^2)^{l_m} g(u) = a_4 \prod_{k=1}^{2l_m}(u - u_k). \tag{6.10}$$

The quantity a_4 is a complex constant and u_k are the complex roots of $G(u)$, known as the *Barrelet Zeros* [91]. Equations 6.9 and 6.10 encapsulate the origin of the ambiguities. The functions f_a and f_b are experimentally determinable from a set of moments $\{\mathrm{t(LM)}\}$, and the g-functions contain the partial waves to be calculated. As the polynomial g-functions enter as absolute squares into the expression for the f-functions, the complex conjugate of some or all of the roots u_k give equally valid solutions, *i.e.* the resulting f-functions, and hence the moments, are not affected.

Waves of $l_m \leqslant 2$ contribute to the $\mathrm{K^+K^-}$ mass spectrum as has been discussed, and so for the $\mathrm{K^+K^-}$ analysis $G(u)$ is a fourth-order complex polynomial and can be expressed as,

$$G(u) = a_4(u-u_1)(u-u_2)(u-u_3)(u-u_4), \tag{6.11}$$

where $\{u_1, u_2, u_3, u_4\}$ are the four roots of the equation. Eight configurations of roots may then be arrived at *via* complex conjugation, these are,

$$\begin{array}{ll} \{u_1^\star, u_2, u_3, u_4\}, & \{u_1, u_2, u_3, u_4\}, \\ \{u_1, u_2^\star, u_3, u_4\}, & \{u_1^\star, u_2^\star, u_3, u_4\}, \\ \{u_1, u_2, u_3^\star, u_4\}, & \{u_1^\star, u_2, u_3^\star, u_4\}, \\ \{u_1, u_2, u_3, u_4^\star\}, & \{u_1^\star, u_2, u_3, u_4^\star\}, \end{array} \tag{6.12}$$

and each associated $g(u)$-function produces a new set of partial waves, which are found using 6.8,

$$\begin{aligned} h_0(\theta) &= \frac{1}{\sqrt{2}}[g(\theta) + g(-\theta)], \\ h_-(\theta) &= \frac{1}{\sqrt{2}}[g(\theta) - g(-\theta)]. \end{aligned} \tag{6.13}$$

This results in eight sets of partial waves in the $\mathrm{K^+K^-}$ analysis that generate identical sets of moments, and which consequently give identical fits to the experimental data. The waves resulting from the fit are dubbed the 'nominal' solution and from this original set all eight sets may be produced.

6.10 Calculation of the Ambiguous Solutions

The calculation of the ambiguous solutions is carried out as follows. The complex polynomial $G(u)$ may be represented in the form,

$$G(u) = a_4 u^4 - a_3 u^3 + a_2 u^2 - a_1 u + a_0, \tag{6.14}$$

where $\{a_0, a_1, a_2, a_3, a_4\}$ are the complex constants defining the polynomial. Once the experimental moments have been fitted and the partial waves of the nominal solution have been found, the set of equations 6.15 can be used to calculate the complex constants.

$$\begin{aligned}
a_4 &= \mathrm{S}_0 - \sqrt{3}\mathrm{P}_0 + \sqrt{5}\mathrm{D}_0 \\
a_3 &= 2\sqrt{3}(\mathrm{P}_- - \sqrt{5}\mathrm{D}_-) \\
a_2 &= 2\mathrm{S}_0 - 4\sqrt{5}\mathrm{D}_0 \\
a_1 &= 2\sqrt{3}(\mathrm{P}_- + \sqrt{5}\mathrm{D}_-) \\
a_0 &= \mathrm{S}_0 + \sqrt{3}\mathrm{P}_0 + \sqrt{5}\mathrm{D}_0
\end{aligned} \tag{6.15}$$

Once the constants have been calculated the roots of the polynomial $\{u_1, u_2, u_3, u_4\}$ can be found using the CERN library routine for calculating the roots of a complex polynomial, WPOLYZ [92]. Each of the eight configurations of the roots listed in 6.12 are then used to generate a new set of partial waves. This is achieved by using the relations,

$$\begin{aligned}
6\mathrm{S}_0 &= a_4(2u_1u_2u_3u_4 + u_1u_2 + u_1u_3 + u_1u_4 + u_2u_3 + u_2u_4 + u_3u_4 + 2), \\
2\sqrt{3}\mathrm{P}_0 &= a_4(u_1u_2u_3u_4 - 1), \\
6\sqrt{5}\mathrm{D}_0 &= a_4(u_1u_2u_3u_4 - u_1u_2 - u_1u_3 - u_1u_4 - u_2u_3 - u_2u_4 - u_3u_4 + 1),
\end{aligned} \tag{6.16}$$

$$4\sqrt{3}\mathrm{P}_- = a_4(u_1u_2u_3 + u_2u_3u_4 + u_3u_4u_1 + u_4u_1u_2 + u_1 + u_2 + u_3 + u_4),$$
$$4\sqrt{15}\mathrm{D}_- = a_4(u_1u_2u_3 + u_2u_3u_4 + u_3u_4u_1 + u_4u_1u_2 - u_1 - u_2 - u_3 - u_4),$$

to produce the ambiguous partial waves with negative reflectivity[2]. The partial waves with positive reflectivity are then found from equations 6.1 using,

$$\begin{aligned}
|\mathrm{D}_+|^2 &= |\mathrm{D}_-|^2 - \frac{7}{\sqrt{10}}\,[\sqrt{4\pi}\,\mathrm{t}(42)],\\
|\mathrm{P}_+|^2 &= |\mathrm{P}_-|^2 + \frac{\sqrt{10}}{2}\,[\sqrt{4\pi}\,\mathrm{t}(42)] - \sqrt{\frac{10}{3}}\,[\sqrt{4\pi}\,\mathrm{t}(22)],\\
\mathcal{R}e\{\mathrm{P}_+\mathrm{D}_+^\star\} &= \mathcal{R}\mathrm{e}\{\mathrm{P}_-\mathrm{D}_-^\star\} - \frac{1}{2}\sqrt{\frac{14}{3}}\,[\sqrt{4\pi}\,\mathrm{t}(32)].
\end{aligned} \tag{6.17}$$

In this way eight complete sets of partial waves are found.

6.11 Linking of the Ambiguous Solutions

Although the eight solutions for each mass-bin can now be generated, it is not known *a priori* which of the solutions 1–8 in mass-bin 2 should follow each of the eight solutions in mass-bin 1. The solutions need to be correctly linked across the mass spectrum, and this is done by linking the roots of the complex polynomial $G(u)$ to establish the order of the solutions. The best continuity of the real and imaginary parts of the roots is found by measuring, and minimising, two quantities simultaneously. One quantity is the difference between a root in a mass-bin (n), and a root in a previous mass-bin $(n-1)$. The second quantity is the difference between the gradient of the slope between two roots in mass-bins (n) and $(n-1)$, and the gradient of the slope between two roots in mass-bins $(n-1)$ and $(n-2)$. These two

[2]The S_0-wave generally becomes complex during this process, but is subsequently set to be real again. The other waves of negative reflectivity are also divided by the phase of the S_0-wave to maintain consistency within the set.

quantities are calculated for the real and imaginary parts of the roots, and combined to form the quantity $\mathcal{F}$. Each permutation of the ordering of the roots is examined such that the minimum value of $\mathcal{F}$ may be found for a mass-bin (n) based upon the information from the previously linked roots. The algorithm used is of the form,

$$\mathcal{R}e\ \mathcal{F} = \alpha \sum_{k=1}^{4} \left(\begin{array}{l} \text{The difference between the real component of a root } (k) \text{ in a} \\ \text{mass-bin } (n)\text{, and the real component of a root } (k) \\ \text{in the previous mass-bin } (n-1)\text{, weighted by the errors on the roots.} \end{array} \right)$$

$$+ (1-\alpha) \sum_{k=1}^{4} \left(\begin{array}{l} \text{The difference between the gradient of the slope between the real} \\ \text{components of two roots in mass-bins } (n-1) \text{ and } (n)\text{, and} \\ \text{the gradient of the slope between the real components of two roots} \\ \text{in mass-bins } (n-1) \text{ and } (n-2)\text{, weighted by the errors on} \\ \text{the roots.} \end{array} \right),$$

where the number of the root is given by k, and α is a factor used to alter the relative importance of the displacements and differentials in the linking process. The factor α may take values in the range of $0 \leqslant \alpha \leqslant 1$, and it has been found from Monte Carlo studies that $\alpha = 0{\cdot}5$ is a good choice, although the linking is relatively insensitive to α in the range $0{\cdot}4 \leqslant \alpha \leqslant 0{\cdot}6$. More precisely, the linking algorithm is given by,

$$\mathcal{R}e\ \mathcal{F} = \alpha \sum_{k=1}^{4} \left[\frac{(\mathcal{R}e\ u_n^k - \mathcal{R}e\ u_{n-1}^k)^2}{(\mathcal{R}e\ \Delta u_n^k)^2 + (\mathcal{R}e\ \Delta u_{n-1}^k)^2} \right]$$

$$+ (1-\alpha) \sum_{k=1}^{4} \left[\frac{[(\mathcal{R}e\ u_n^k - \mathcal{R}e\ u_{n-1}^k) - (\mathcal{R}e\ u_{n-1}^k - \mathcal{R}e\ u_{n-2}^k)]^2}{(\mathcal{R}e\ \Delta u_n^k)^2 + (\mathcal{R}e\ 2\Delta u_{n-1}^k)^2 + (\mathcal{R}e\ \Delta u_{n-2}^k)^2} \right], \qquad (6.18)$$

where Δu is the error on a root. The quantity $\mathcal{R}e\ \mathcal{F}$ is calculated using equation 6.18, and the same process is applied to the imaginary parts to calculate the complimentary quantity $\mathcal{I}m\ \mathcal{F}$. The linking is then governed by the minimisation of the function $\mathcal{F}$, where $\mathcal{F} = \mathcal{R}e\ \mathcal{F} + \mathcal{I}m\ \mathcal{F}$. The algorithm is applied to each mass-bin from threshold upwards, and when the optimum ordering of the roots is found for each mass-bin it is fixed. The linking process in the next mass-bin then uses this information in performing its own linking, until the final mass-bin is reached. *N.B.* The roots in the first mass-bin are used in the order in which they naturally occur, and the roots in the second mass-bin are linked using only the difference in distances between the roots, as information about the change in gradient is not available at that point.

6.12 Monte Carlo Investigations

The validity of the analysis performed on the real data has been investigated by applying the same procedures to Monte Carlo data. Both Monte Carlo data before and after it has been passed through the detector simulation package has been examined. The former and latter data sets will henceforth be called *Monte Carlo input data* and *Monte Carlo output data* respectively. The Monte Carlo program has been modified to generate mass spectra in S, P, and D-waves. In addition to this, resonances of chosen masses, widths and amplitudes, in either S, P or D-waves can be included in the mass spectrum. The spin analysis methods are checked by generating the moments and extracting the partial waves from the Monte Carlo data, and by checking that the known input distributions have been properly reproduced.

6.12.1 Monte Carlo Input Data

Monte Carlo input data can be produced with high statistics relatively quickly, and so the angular distributions of these data have small statistical errors and are of a high quality. This provides data sets with which the spin analysis methods can be checked, to see if they are valid in theory, *i.e.* without approximations and/or errors introduced by the acceptance correction process. It has been found that the moments and extracted partial waves from various configurations of Monte Carlo input data consistently display the expected distributions, and that fluctuations were within statistical errors. This has been tested for pure S, P, and D-wave mass spectra, and mass spectra of different spins containing a varying number of resonances of different spins.

6.12.2 Monte Carlo Output Data

The angular distributions of the Monte Carlo input data are known, and hence it is known what angular distributions the Monte Carlo output data should be restored to when corrected for acceptance effects. This provides an opportunity to see the effects of any approximations and/or inaccuracies introduced by the acceptance correction process, the level of which can be assessed from the level of the inaccuracies in the acceptance corrected angular distributions. This can be achieved by comparing the moments from the input data, and the moments from the acceptance corrected data. By then extracting the partial waves, and comparing them with the known input waves it can be established if the partial wave analysis is able to correctly determine the spin of the Monte Carlo data after acceptance correction, and again, to assess the level of error (or *feed-through* from one partial wave to another) introduced by imperfections in the acceptance correction process.

Moments from S-wave and D_0-wave Mass Spectra

Shown in figures 6.7 and 6.8 are the moments of an S-wave mass spectrum. The Monte Carlo input data ($\bullet$) and acceptance corrected output data ($\diamond$) are shown together. It can be seen that the moments of the acceptance corrected output data have been restored such that they are consistent with the input data. Figures 6.9 and 6.10 show the moments for a D_0-wave mass spectrum in the same format, where it can be seen that the majority of the moments have been acceptance corrected well and are consistent with the distributions of the input data. It is also true that the

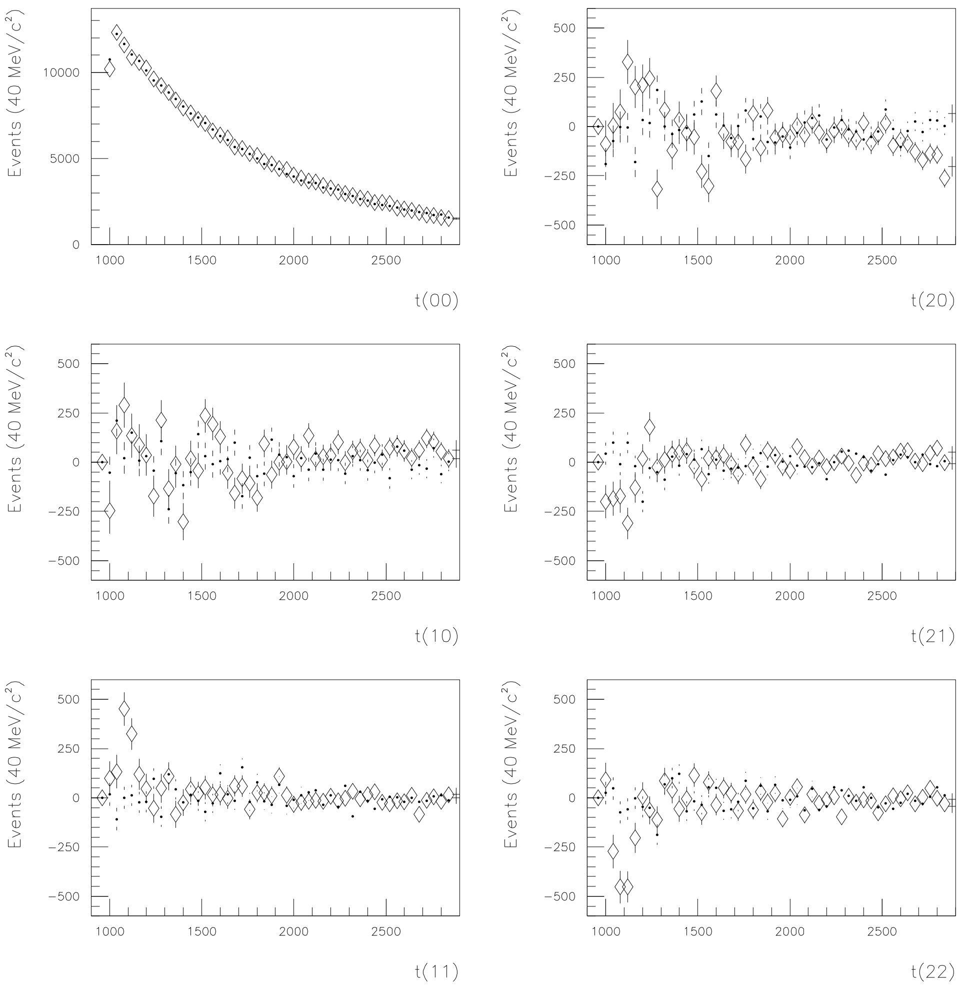

Figure 6.7: Moments of Monte Carlo input (•) and acceptance corrected (⋄) S-wave data.

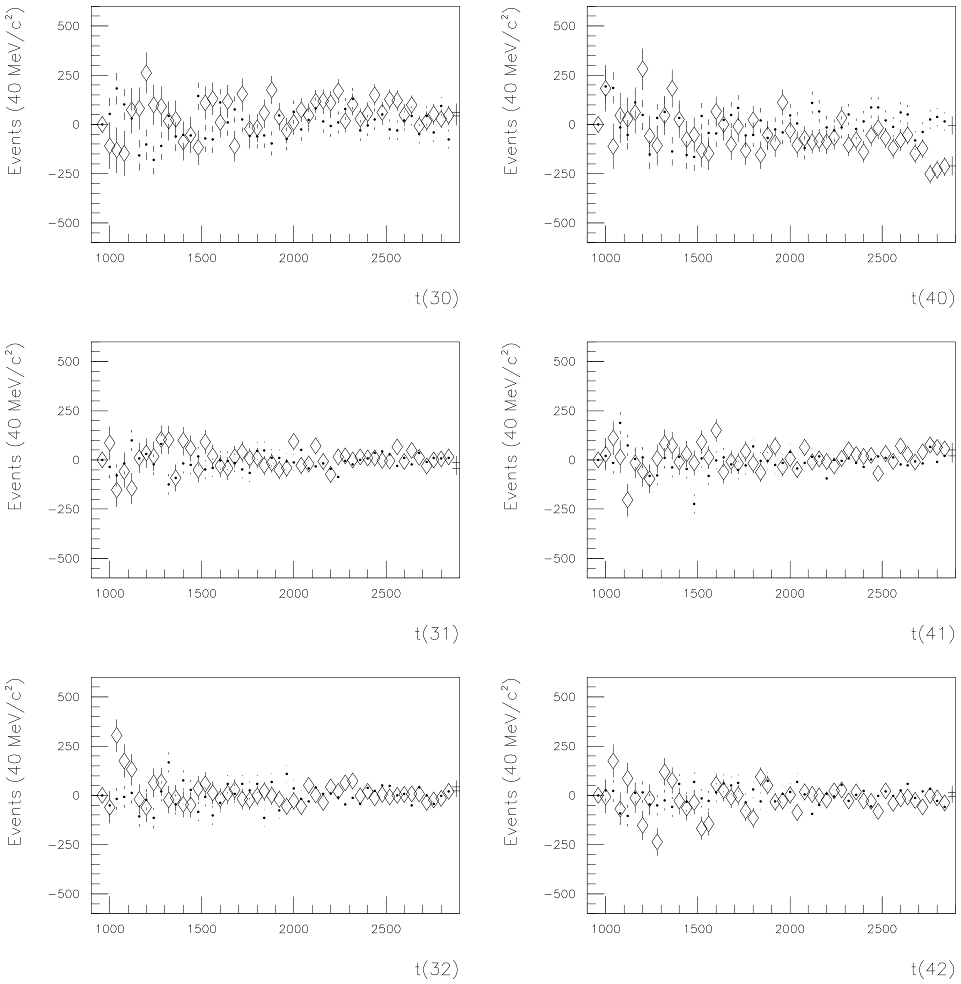

Figure 6.8: Moments of Monte Carlo input (•) and acceptance corrected (⋄) S-wave data.

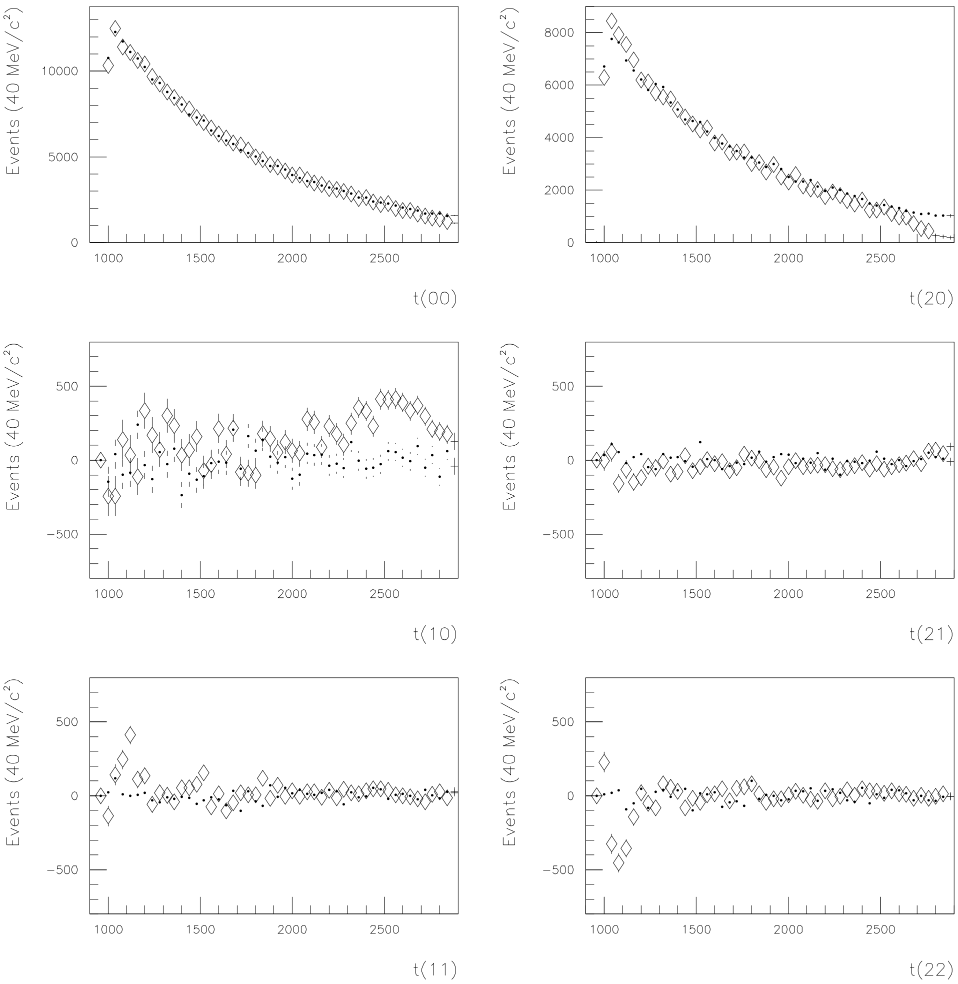

Figure 6.9: Moments of Monte Carlo input (•) and acceptance corrected (⋄) D_0-wave data.

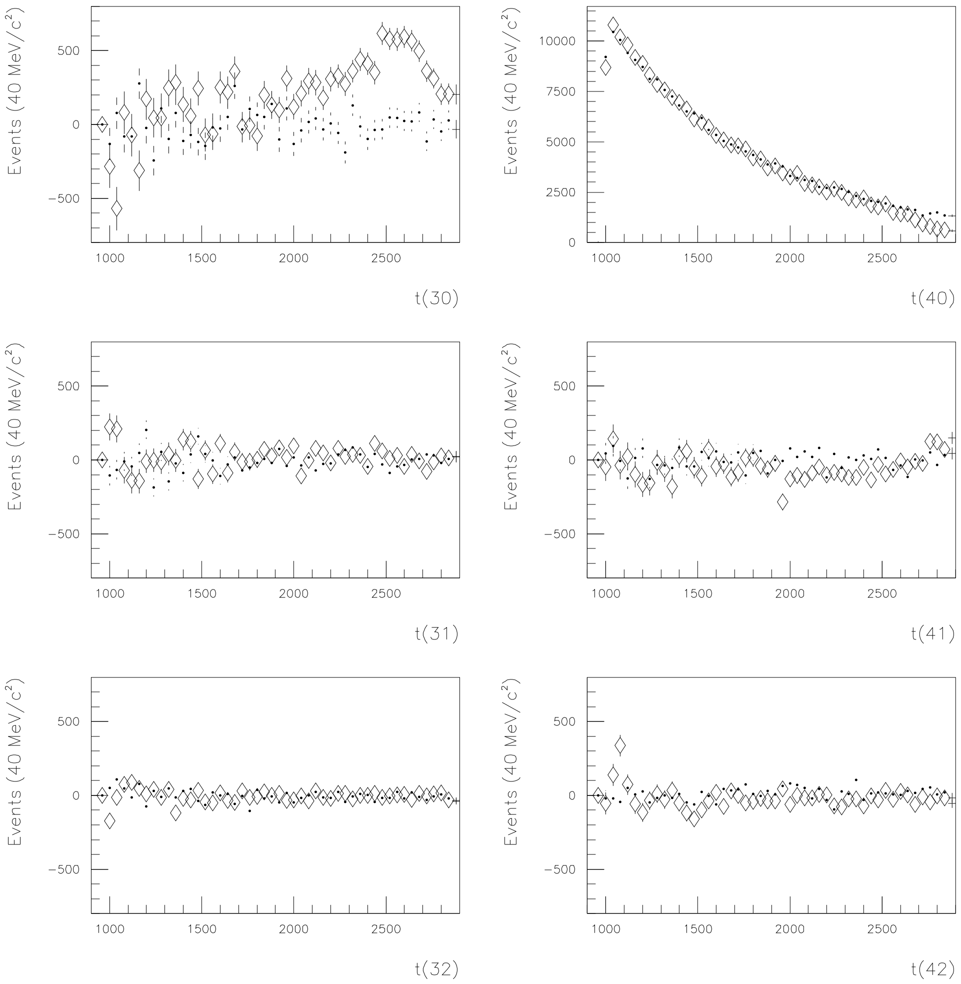

Figure 6.10: Moments of Monte Carlo input (•) and acceptance corrected (⋄) D_0-wave data.

moments t(10) and t(30), which should display no activity and should be consistent with zero for pure D_0-wave, deviate from the correct distributions and contain non-negligible activity at masses of $m_{K^+K^-} > 2{\cdot}4$ GeV/c^2. This shows a reduced quality of acceptance correction in this high mass region, the cause of which is almost certainly contributed to by the low statistics in this region of the acceptance tables, where the phase-space of the mass spectrum tails off to its lowest number of events. This deviation is not detrimental to the analysis of the real data as it is above the important K^+K^- mass range, in a region where there are few statistics. It is interesting to note that this deviation at high mass does not affect the quality of the partial waves extracted from the acceptance corrected D_0-wave (the reason for which is explained on page 125). On page 128 it is explained why it is expected that if an area of reduced quality of acceptance correction does affect the real data anywhere in the mass spectrum, then this would be a detectable effect.

Partial Waves from S-wave and D_0-wave Mass Spectra

The partial waves from the S-wave and D_0-wave mass spectra have been extracted using the same PWA method as applied to the real data. As discussed in section 6.9 there are eight ambiguous solutions for the partial waves. For the real data, physical constraints will be applied to select the physical solution, and to investigate their effectiveness the same constraints are applied to the Monte Carlo S-wave partial waves. The argument used is that at, and close to threshold (in the absence of a non-spin-zero resonance) the physical K^+K^- mass spectrum should be dominated by S-wave, and using this criterion seven of the solutions can be discounted as they have at least as much P-waves and/or D-waves as S-wave at, and close to threshold. The physical solution for the acceptance corrected S-wave data is shown in figure 6.11, where it can be seen that the S-wave mass spectrum is reproduced well, and that contributions from other waves are small, the main feed-through from one wave to another being from the S-wave into the D_0-wave. The seven solutions rejected as being unphysical are shown in figures B.1 to B.7 in appendix B.1.

The partial waves for the D_0-wave are shown in figure 6.12, in the case of D_0-wave all eight ambiguous solutions are identical. The reason for this can be understood by considering the nature of the ambiguous solutions. The set of moments resulting from an S-wave angular distribution may be produced by S-wave, by a combination of P_0, P_- and P_+ waves, by a combination of S, P_0, P_- and P_+ waves, *etc.* However, the set of moments resulting from D_0-wave angular distributions can only be produced by one combination of waves, *i.e.* pure D_0-wave, hence all eight D_0-wave solutions are identical. This is a noteworthy facet of the analysis, as it means that D_0-wave in a mass spectrum cannot migrate to other partial waves as a result of the existence of the ambiguous solutions as is seen occurring in the unphysical S-wave solutions. This is true even if the linking of the roots is poor, incorrect, or even not applied at all.

The PWA for the D_0-wave data has produced the correct result, with no activity in partial waves other than the D_0-wave. This has occurred in spite of the fact that the acceptance corrected moments for the D_0-wave in the mass region of $m_{K^+K^-} > 2{\cdot}4$ GeV/c^2 had developed activity in the moments t(10) and t(30), which should be inactive for pure D_0-wave. The reason for the correct result is that the acceptance corrected set of moments could not be fitted simultaneously by equations 6.1, because the set of moments had been altered into a *self-inconsistent set*, *i.e.* a set which creates inconsistencies in the equations, as the acceptance corrected moments could not be created from the angular distributions of spin-zero, spin-one, and spin-two particles. The inability to fit the regions of the moments that have suffered from a lower quality of acceptance correction is shown in figures 6.13 and 6.14, where the moments of the D_0-wave acceptance corrected data ($\bullet$) are compared with the reconstructed moments from the PWA fit ($\diamond$).

If data have been distorted such that the moments produced from it are a self-inconsistent set, then for a fit to be made to these data during the PWA, the fitted moments are forced into the nearest self-consistent set. In the case of the D_0-wave, as might be expected in other cases if the distortions are small, the moments were forced

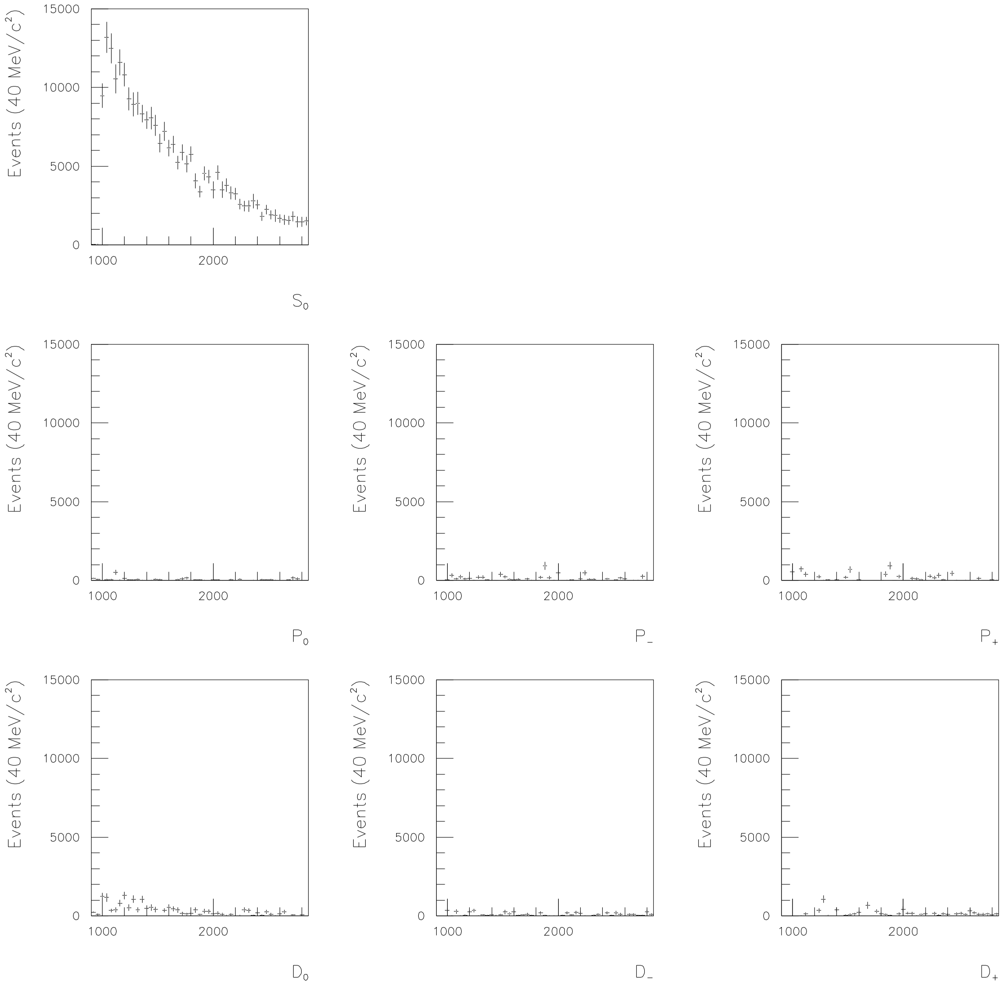

Figure 6.11: Solution selected by imposing a physical criterion, from the PWA of an S-wave phase-space.

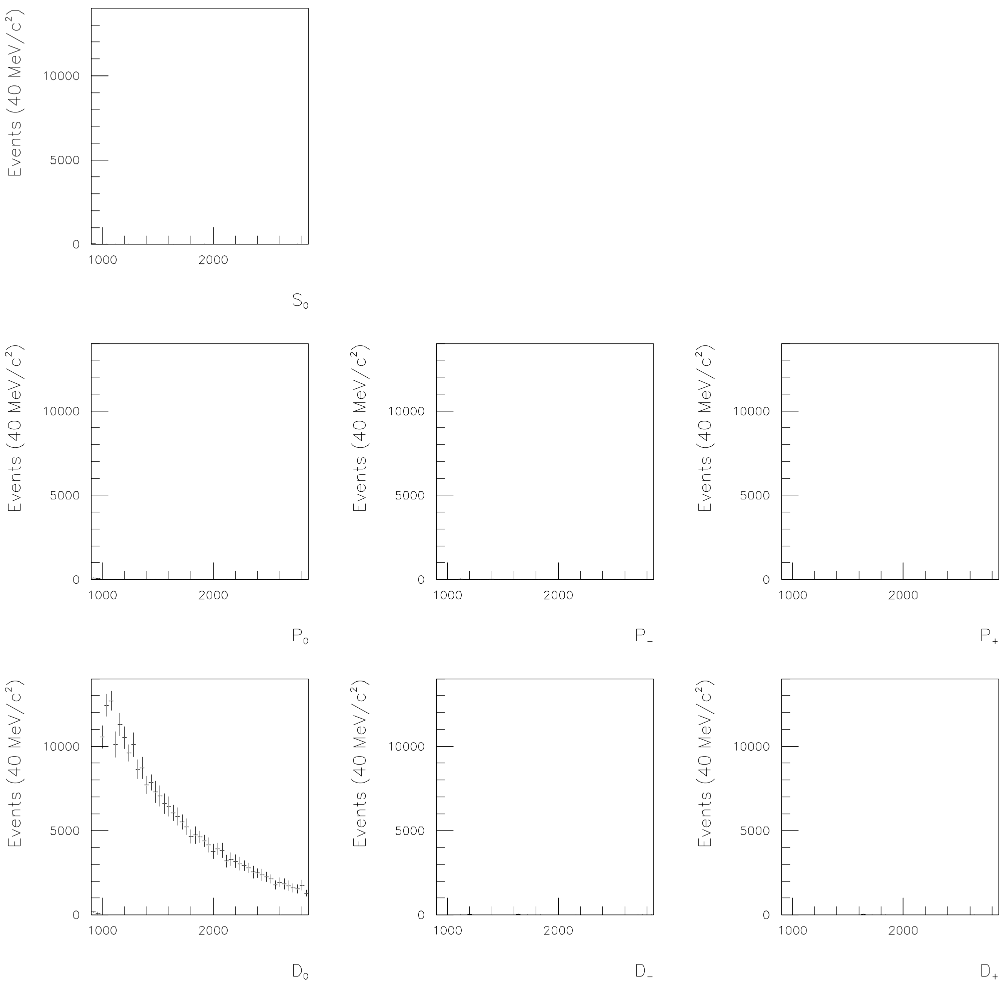

Figure 6.12: Solution selected by imposing a physical criterion, from the PWA of a D_0-wave phase-space.

back to their original self-consistent distributions. Should data suffer from a reduced quality of acceptance correction, then the moments from that data will develop self-inconsistencies[3] at some level. Regions of the moments that are of a poor quality are evident, as the moments from the fit compare poorly with the moments from the data. This demonstrates that a good fit to the data requires a self-consistent set of experimental moments, indicating that the moments have not been improperly distorted by the acceptance correction process. Although the rather unphysical situation of a pure D_0-wave mass spectrum does have small problems introduced into it from the acceptance correction at masses of $m_{K^+K^-} > 2{\cdot}4$ GeV/c^2, the S-wave mass spectrum does not have the same problem and its moments are mainly fitted well. Most significantly, the moments from the real data are fitted well, as shown in section 6.13 in figures 6.19 and 6.20, and hence must be a self-consistent set of moments, consistent with a good quality acceptance corrected data set.

Partial Waves from S-wave Phase-Space with Resonances

A key motivation for the partial wave analysis of the K^+K^- mass spectrum is to measure the spin of the $\theta/f_J(1710)$, and it is also important to do the same for the resonance in the $1{\cdot}5$ GeV/c^2 region. The resonance in the $1{\cdot}5$ GeV/c^2 region has previously been identified as the $f_2'(1525)$ by the WA76 collaboration [68]. However, in the E690 collaboration's $K^0_S K^0_S$ mass spectrum which is very similar to the K^+K^- mass spectrum of this analysis, it is found that the peak in the $1{\cdot}5$ GeV/c^2 region is predominantly S-wave [59]. The $\theta/f_J(1710)$ can be spin-zero or spin-two and while results for both have been put forward, the answer remains contentious. For these reasons it is important to establish whether the spin analysis methods described in this thesis can distinguish between two nearby resonances in practice, when either of which could be spin-zero or spin-two. To investigate this question, two overlapping

[3]Except for the situation in which each of the appropriate moments in the set of twelve has been altered in such a way, and by the required quantities, that a new self-consistent set of moments are formed.

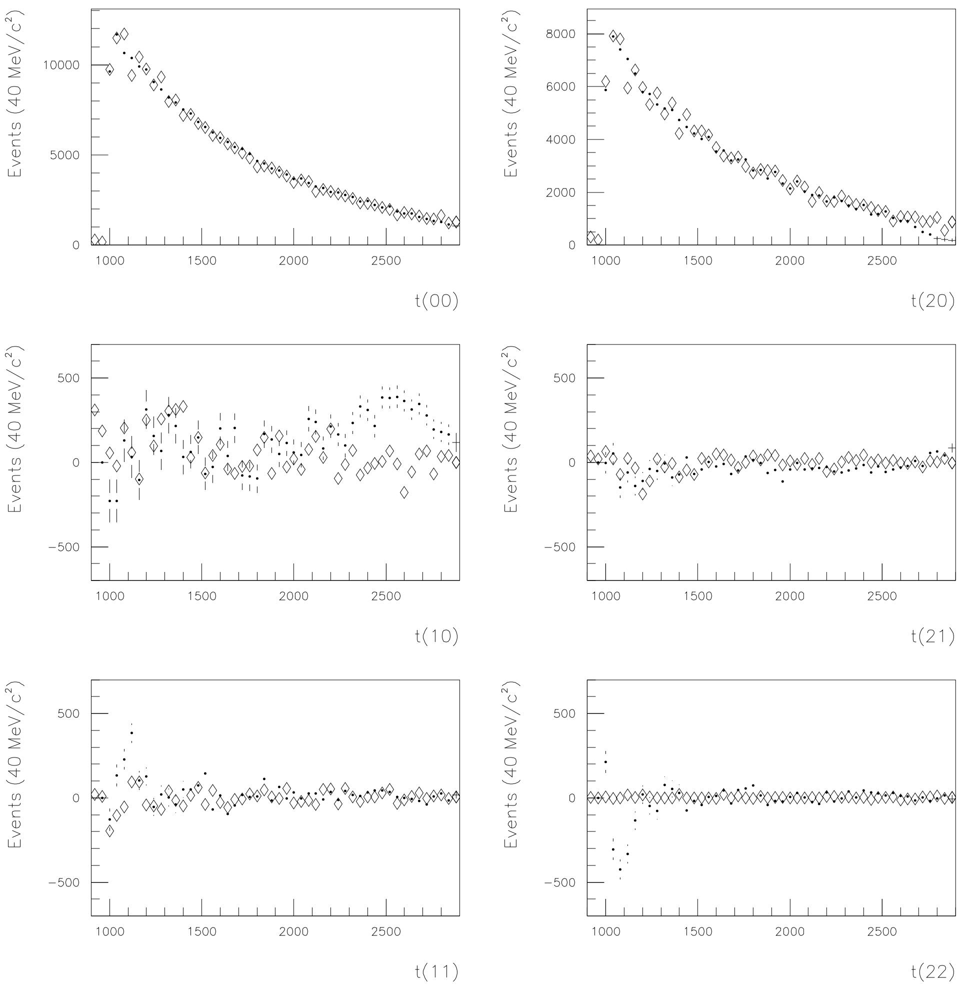

Figure 6.13: Moments of Monte Carlo acceptance corrected D_0-wave data ($\bullet$), and the data after being forced into the nearest self-consistent configuration by the PWA fitting procedure ($\diamond$).

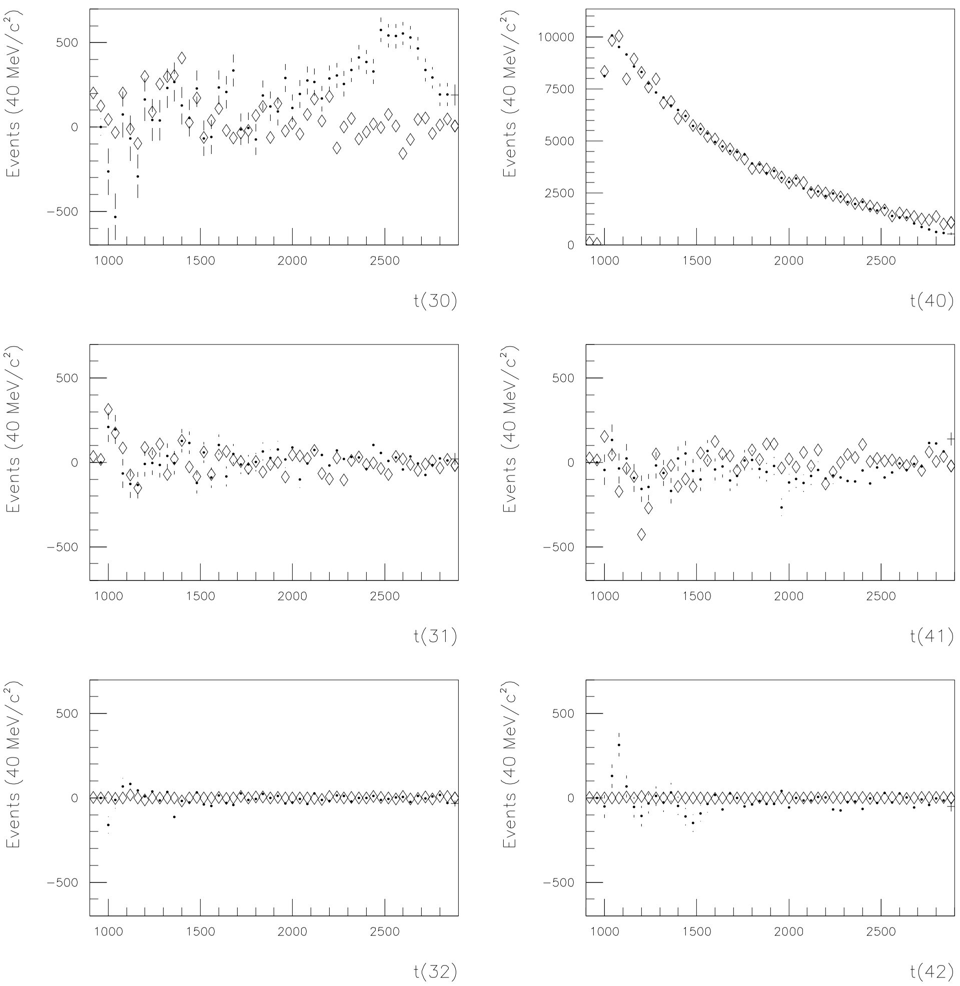

Figure 6.14: Moments of Monte Carlo acceptance corrected D_0-wave data ($\bullet$), and the data after being forced into the nearest self-consistent configuration by the PWA fitting procedure ($\diamond$).

Breit-Wigner resonances on an S-wave phase-space were created using the Monte Carlo generator, thereby creating a similar situation to that which exists in the K^+K^- data. The two resonances were made in combinations of S-wave and D_0-wave producing the four situations which may plausibly exist. A partial wave analysis was then performed on each data set to discover whether the spins of the resonances, and of the phase-space, could be reliably extracted.

Shown in figures 6.15, 6.16, 6.17 and 6.18 are the physical solutions for the mass spectra containing an $f_{J=0}(1500)$ and $f_{J=0}(1710)$, an $f_{J=0}(1500)$ and $f_{J=2}(1710)$, an $f_{J=2}(1500)$ and $f_{J=0}(1710)$, and an $f_{J=2}(1500)$ and $f_{J=2}(1710)$ respectively, where the solutions rejected as being unphysical are excluded using the same criterion as before. The behaviour of the S-wave components of the ambiguous solutions display the same characteristics as for the pure S-wave phase-space ambiguous solutions. However, the behaviour of the D_0-wave components of the ambiguous solutions of the mass spectra behave quite differently. These ambiguous solutions were all identical, and correctly found in the D_0-wave. This is another example of the characteristics of the eight pure D_0-wave partial wave solutions and demonstrates again, with resonances, that although S-wave and P-waves have ambiguous solutions that can misrepresent their true nature, it has been found that D_0-wave does not migrate into other waves, as its ambiguous solutions are all identical. This is a significant feature and, although it is by no means crucial to the analysis, it is encouraging to know that if D_0-wave is present in the mass spectrum, then it cannot be disguised by the ambiguities inherent in the analysis. It can be seen from the physical solutions that in all four cases the spins of the resonances, and the spin of the phase-space are correctly extracted. The activity in the P_0, P_-, P_+, D_-, and D_+ waves are small, and consistent with zero as they should be. There is some feed through from the S-wave into the D_0-wave, which can be seen from figure 6.15 is worse at lower masses ($\lesssim 1{\cdot}4$ GeV/c^2) but which improves towards higher masses. This is due to a lower quality of acceptance correction in this region that creates some structure in the angular distributions which is then interpreted as non-spin-zero wave contributions.

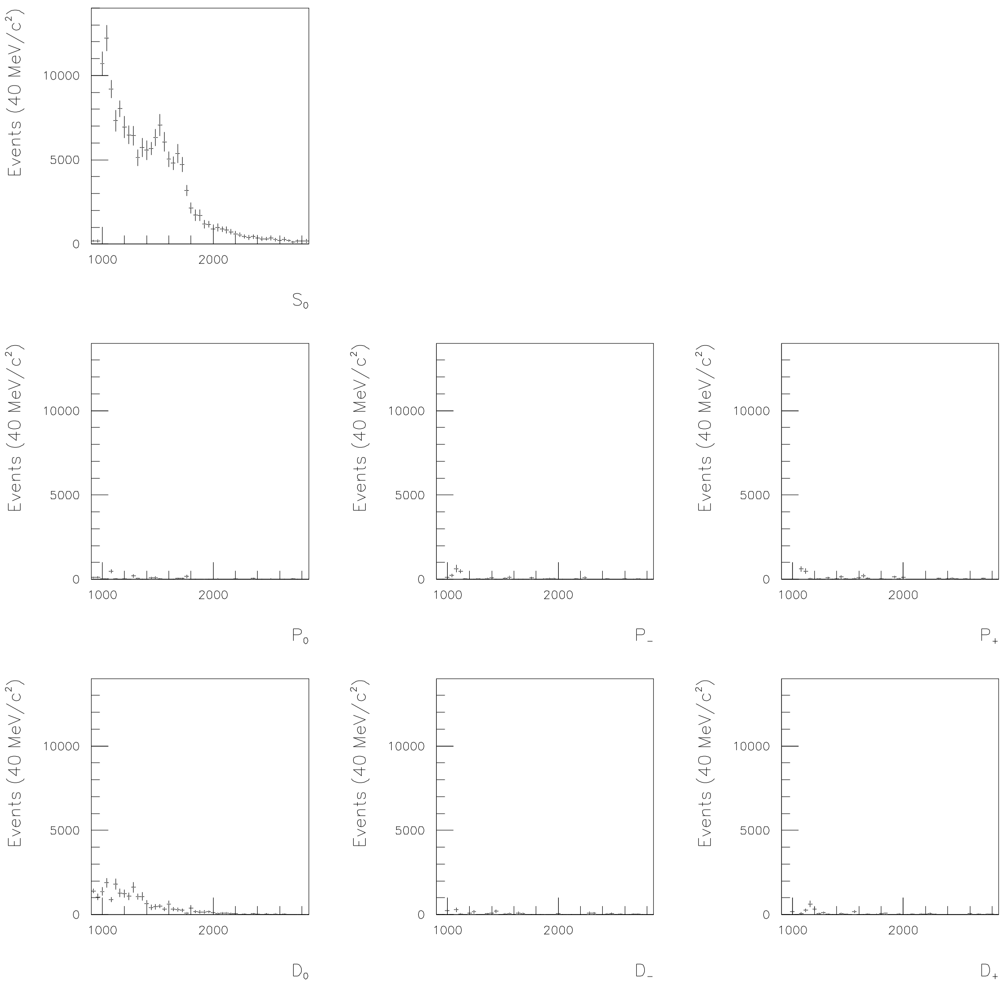

Figure 6.15: Solution selected by imposing a physical criterion, from the PWA of an S-wave phase-space with resonances representing an $f_{J=0}(1500)$ and an $f_{J=0}(1710)$.

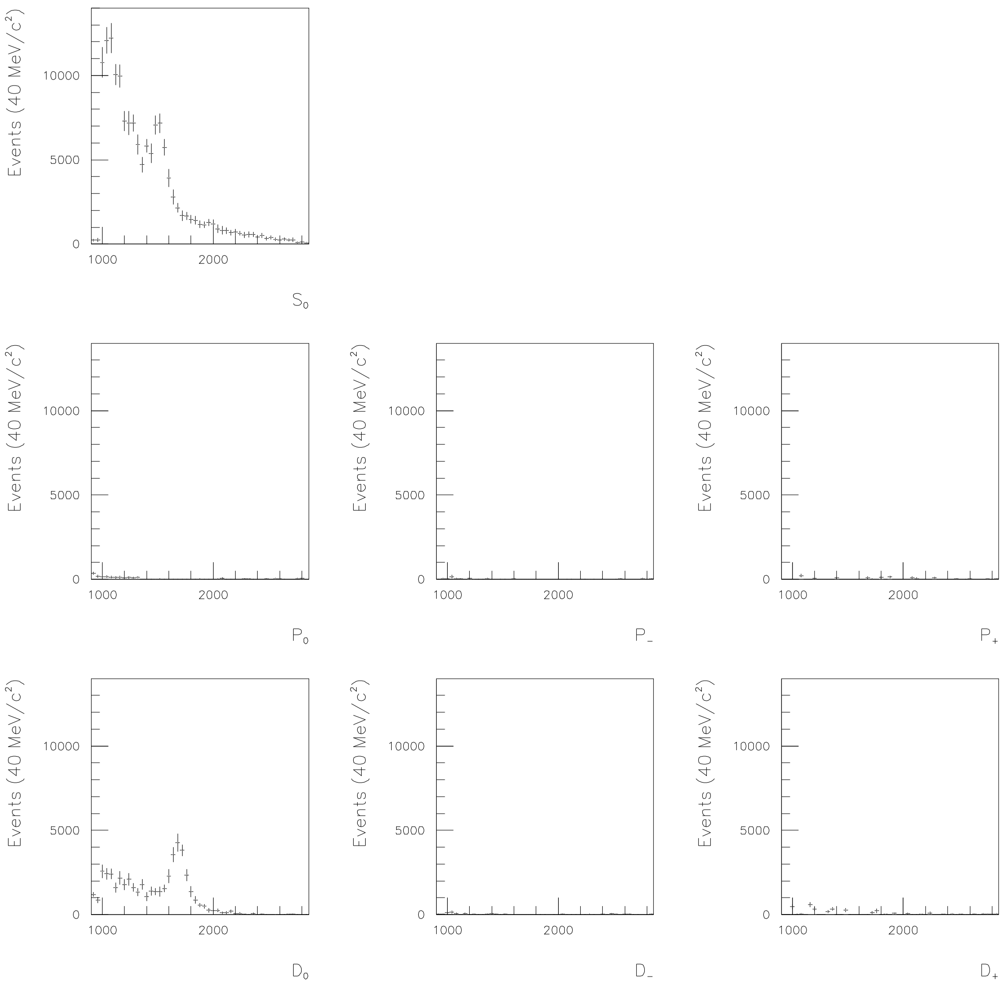

Figure 6.16: Solution selected by imposing a physical criterion, from the PWA of an S-wave phase-space with resonances representing an $f_{J=0}(1500)$ and an $f_{J=2}(1710)$.

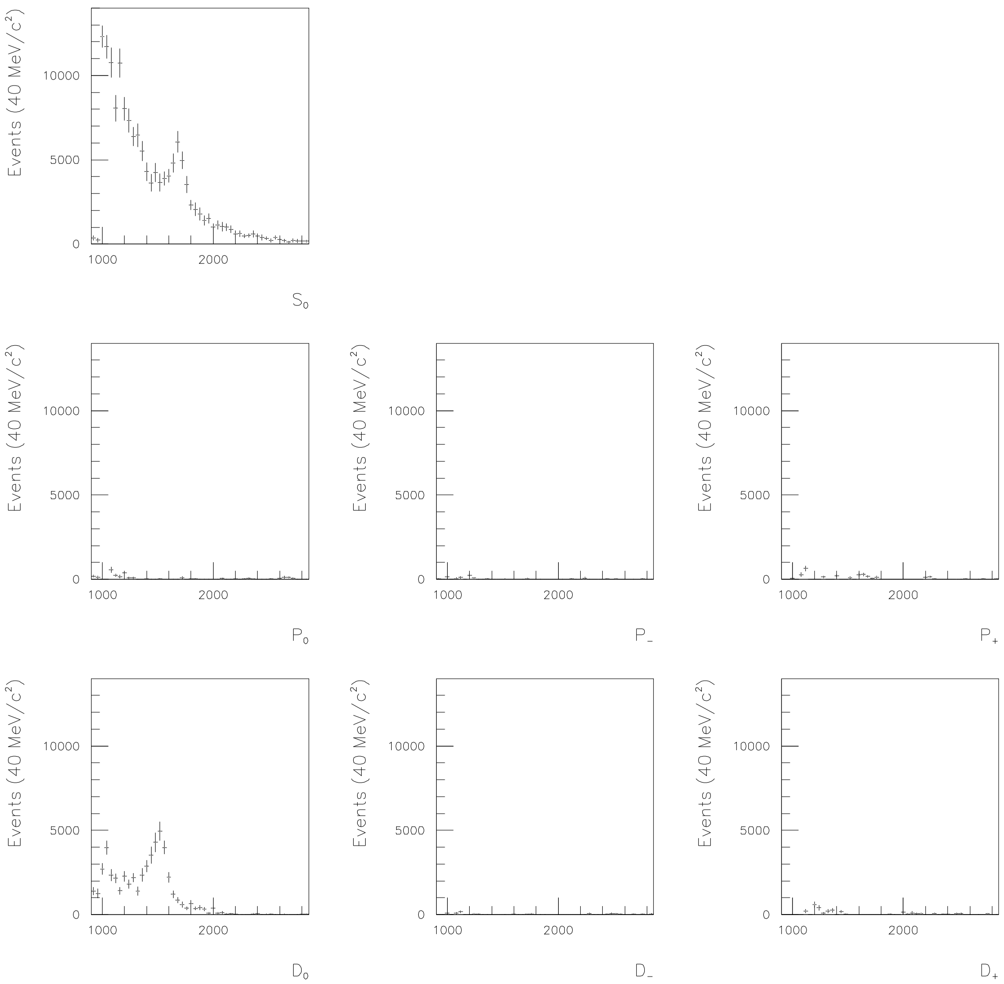

Figure 6.17: Solution selected by imposing a physical criterion, from the PWA of an S-wave phase-space with resonances representing an $f_{J=2}(1500)$ and an $f_{J=0}(1710)$.

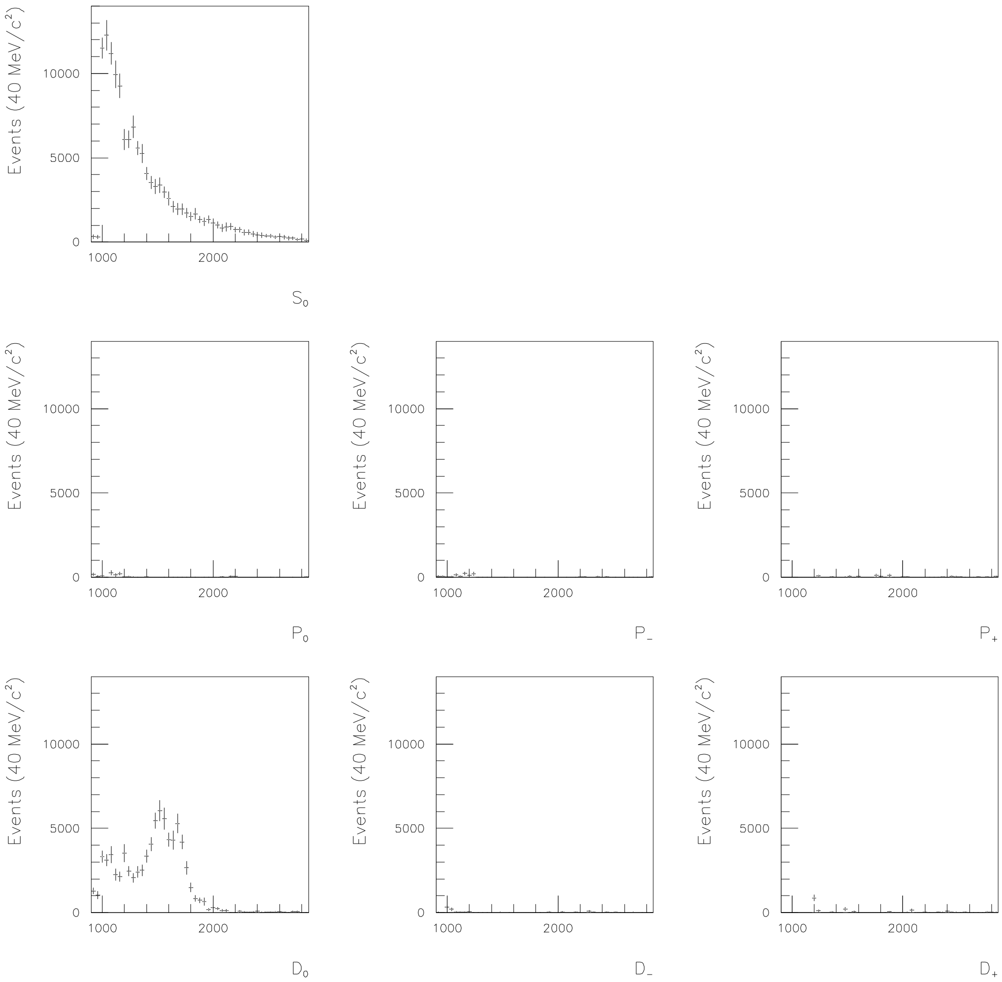

Figure 6.18: Solution selected by imposing a physical criterion, from the PWA of an S-wave phase-space with resonances representing an $f_{J=2}(1500)$ and an $f_{J=2}(1710)$.

To summarise the Monte Carlo investigations, the problem of feed-through is common to all spin analyses, and it is shown from the PWAs of the Monte Carlo mass spectra containing resonances that the level of feed-through present in this spin analysis does not disrupt reliable spin measurements. This has been investigated with specific attention paid to the spin measurements of a spin-zero or spin-two resonance at 1·5 GeV/c^2, and of a spin-zero or spin-two resonance at 1·7 GeV/c^2. In particular, it has been found during the Monte Carlo studies that the S-wave can incorrectly feed into the D_0-wave, but that the D_0-wave is readily identifiable, even in the situation where it has been somewhat distorted by approximations in the acceptance correction, and has never been found to feed incorrectly into waves of a lower spin.

6.13 Partial Wave Analysis of 1996 K^+K^- Data

The partial wave analysis, described and tested with Monte Carlo data in earlier sections, was applied using the same methods to the 1996 K^+K^- data. The PWA fitting procedure produces a good quality fit to the data as is shown in figures 6.19 and 6.20 where it can be seen that the experimental data are fitted well throughout the moments, and across the whole mass spectrum. As previously discussed, this not only shows that a good description of the data has been produced, but it also shows that the moments are a self-consistent set after acceptance correction.

As has been described in section 6.11 the eight ambiguous solutions need to be linked together across the mass range, and this is achieved by linking the real and imaginary parts of the roots of the complex polynomial equation 6.11 using the algorithm 6.18. The linked roots are shown in figure 6.21 where the roots u_1, u_2, u_3, and u_4 are represented by an open star, filled star, diamond, and bullet respectively. It can be seen that while the imaginary components show little structure, the real components display discernibly separate trajectories that indicate the appropriate linking of the solutions.

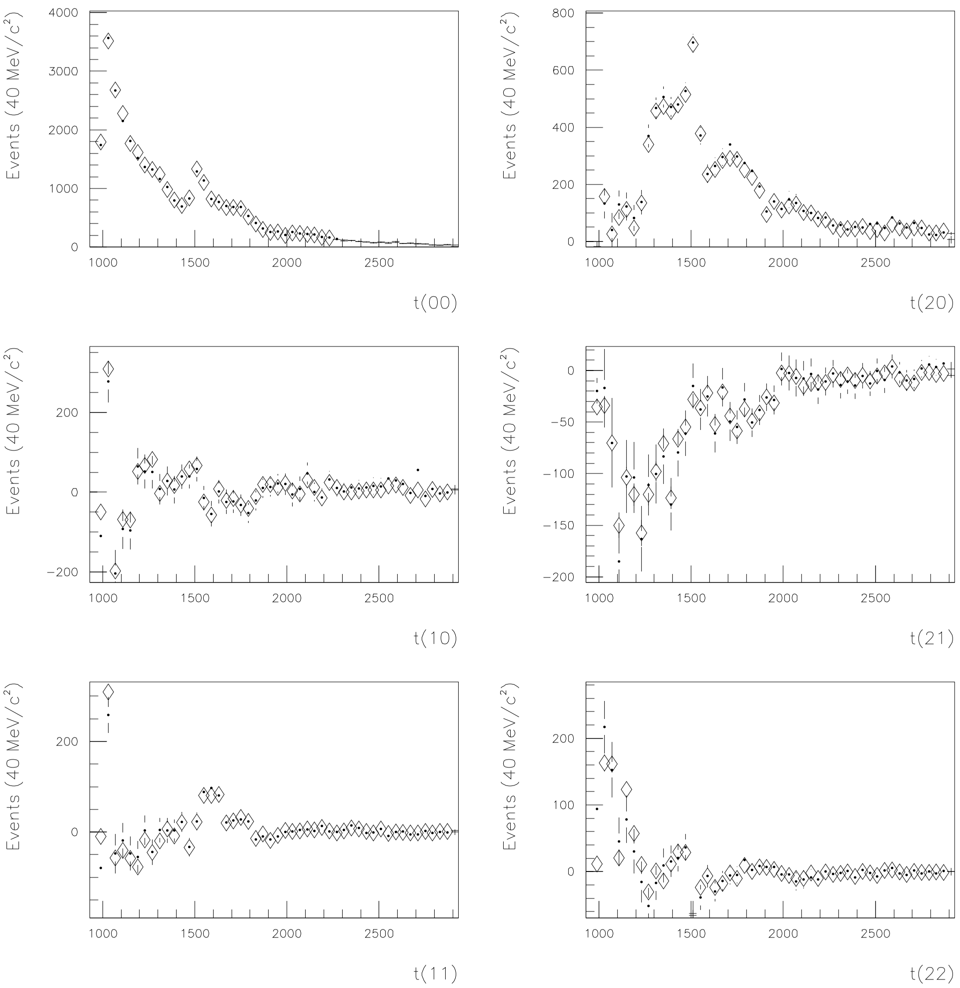

Figure 6.19: Moments of the K^+K^- data ($\bullet$), and of the data after the PWA fitting procedure ($\diamond$). The data are fitted well.

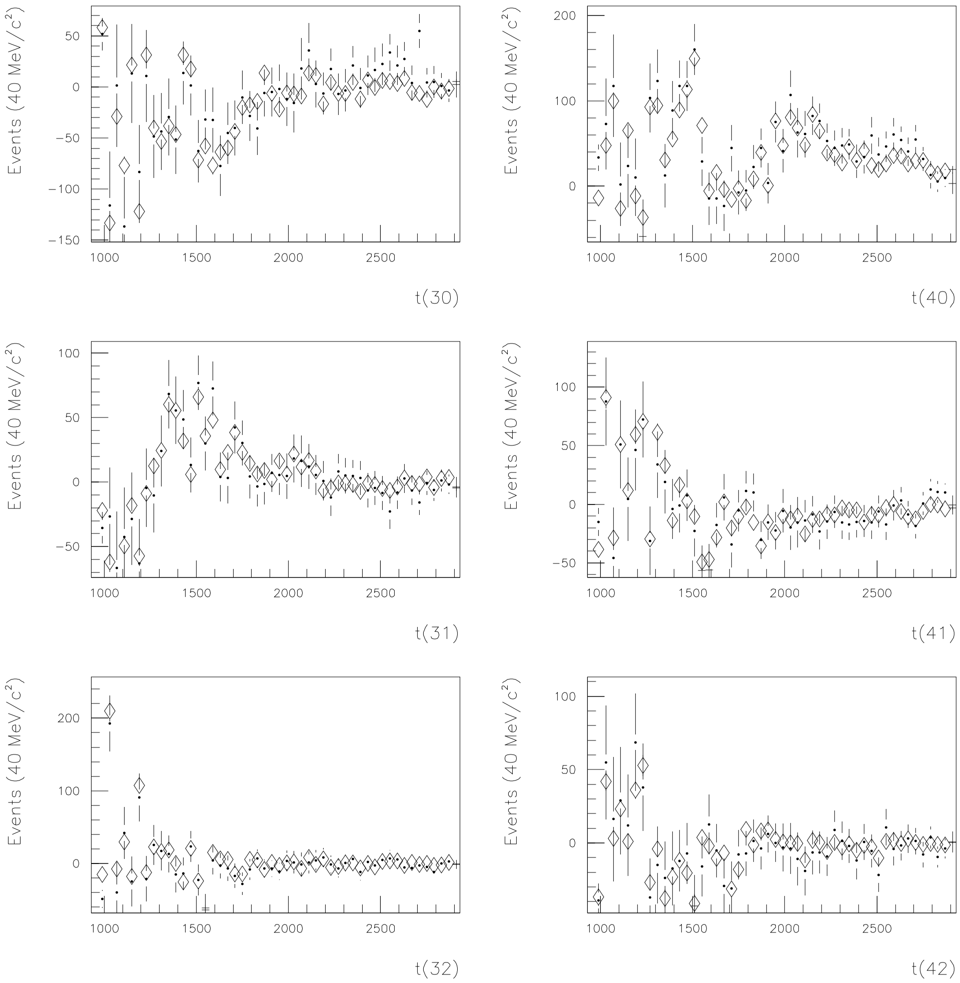

Figure 6.20: Moments of the K^+K^- data (•), and of the data after the PWA fitting procedure (⋄). The data are fitted well.

Once the eight solutions have been linked, physical constraints may be applied to select the physical solution that describes the experimental data. The criterion used is that at, and close to threshold (in the absence of a non-spin-zero resonance) the mass spectrum should be dominated by S-wave, and by using this argument seven of the eight solutions may be rejected as being unphysical. The unphysical solutions are shown in figures B.8 to B.14 in appendix B.2. Unphysical solution 1 (figure B.8) has been rejected on the basis that there is a greater quantity of D-waves at, and close to threshold than S-wave, while unphysical solution 2 (figure B.9) has primarily more P-waves, and also more D-waves, than S-wave at, and close to threshold. Unphysical solutions 3 – 7 (figures B.10 – B.14) all have the same unphysical traits of there being a greater quantity of P-waves at threshold and close to threshold than S-wave.

Only one solution passes the criterion imposed, and this physical solution is shown in figure 6.22. It is found that the K^+K^- mass spectrum is dominated by S-wave, which accounts for $\sim$80% of the data. The main characteristics of the S-wave are a large threshold enhancement, and peaks in the 1·5 GeV/c^2 and 1·7 GeV/c^2 regions. There are no significant structures in the 1·7 GeV/c^2 region in any of the other waves. The wave containing the second largest amount of activity is the D_0-wave, which accounts for $\sim$10% of the data. Although the statistics are lower, it can be seen that the important characteristics appear to be peaks in the 1·3 GeV/c^2 and 1·5 GeV/c^2 regions, and a broad peak in the 2·15 GeV/c^2 region. The remaining five waves contain only $\sim$10% of the experimental data among them, and are not considered statistically significant.

A fuller discussion of the physical solution is presented in chapter 7. This includes a simple fit to the partial waves and an interpretation of the resonances they contain. This analysis is to be printed in *Physics Letters* [93].

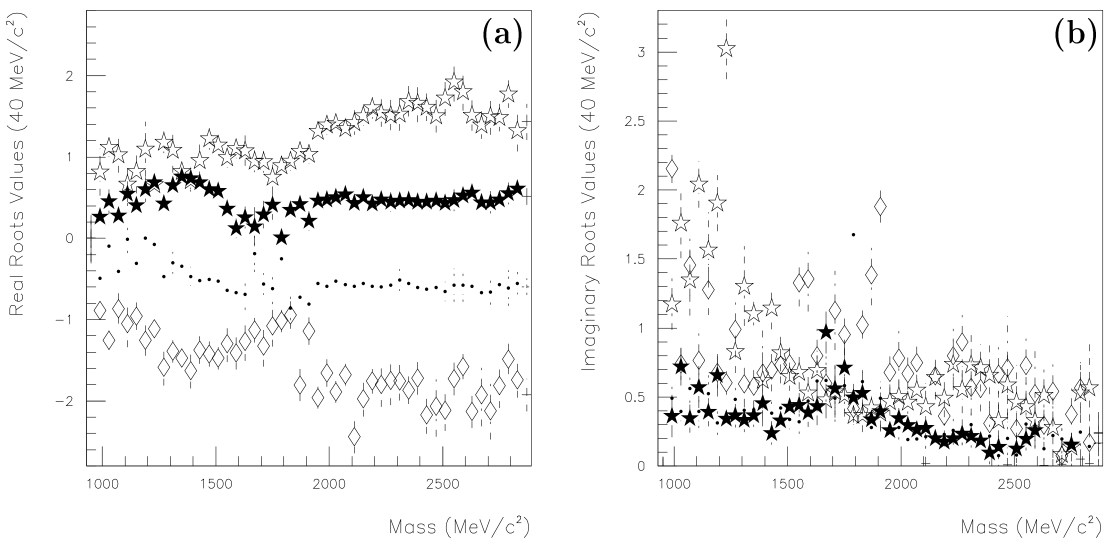

Figure 6.21: The (a) four real parts, and (b) four imaginary parts of the complex roots after the linking procedure.

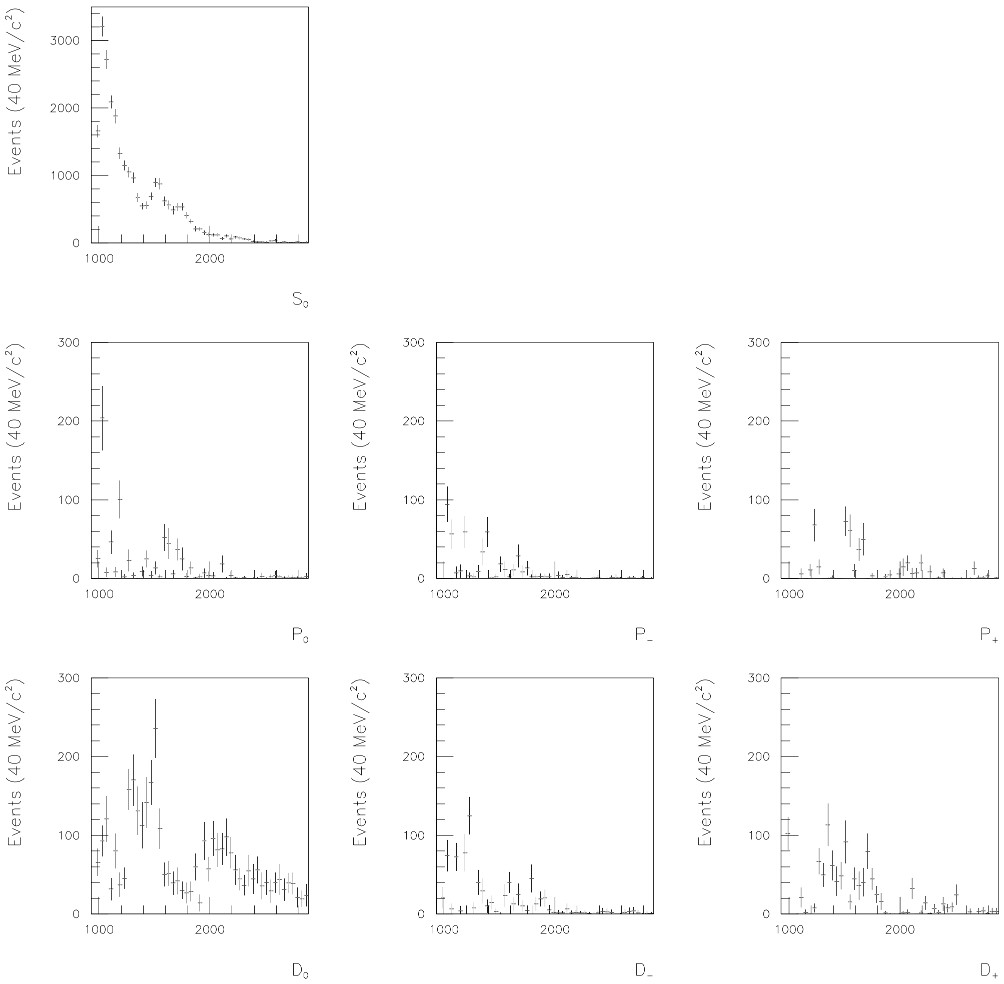

Figure 6.22: Solution selected by imposing a physical criterion, from the PWA of the acceptance corrected 1996 K^+K^- data.

Chapter 7

Discussion of PWA Results

7.1 Interpretation of the Partial Waves

The S-wave contains the majority ($\sim$80%) of the activity of the K^+K^- data. Its main features are a threshold enhancement, a peak in the $\sim$1·5 GeV/c^2 region, and a peak in the $\sim$1·7 GeV/c^2 region. These are interpreted as the $f_0(980)$, $f_0(1500)$, and a spin-zero $\theta/f_J(1710)$ respectively. The S-wave has been fitted from threshold to 2·7 GeV/c^2 using spin-zero relativistic Breit-Wigners [94] to describe the $f_0(1500)$ and $\theta/f_J(1710)$ and a Flatté function ($F_{K\overline{K}}(m)$) [95] to describe the $f_0(980)$. The mass of the $f_0(980)$ is close to the $K\overline{K}$ threshold, and it couples strongly to both the $K\overline{K}$ and $\pi^+\pi^-$ channels; for these reasons it is not appropriate to attempt to describe it using a standard Breit-Wigner, and so a coupled channel formalism must be used [95]. The function $F_{K\overline{K}}(m)$ is defined as,

$$F_{K\overline{K}}(m) = \frac{m_R\sqrt{\Gamma_o\Gamma_{K\overline{K}}}}{m_R^2 - m^2 - im_R(\Gamma_{\pi^+\pi^-} + \Gamma_{K\overline{K}})},$$

where $\Gamma_{\pi^+\pi^-}$ and $\Gamma_{K\overline{K}}$ are the $f_0(980)$ partial decay widths to the $\pi^+\pi^-$ and $K\overline{K}$ channels respectively, m_R is the mass of the $f_0(980)$, m is the mass of the central system, and Γ_o is the (unknown) coupling of the exchange particles to the central system. In addition to two Breit-Wigners and the Flatté function, a polynomial background of the form,

$$\mathrm{B.G.}(m) = a(m - m_{\mathrm{th}})^b \exp^{(-cm-dm^2)}, \tag{7.1}$$

is also incorporated to describe the S-wave, where m is the $\mathrm{K^+K^-}$ mass, m_{th} is the $\mathrm{K^+K^-}$ threshold mass, and a, b, c, d are fit parameters. The resonances and background comprising the S-wave are all permitted to interfere, and the S-wave is given by,

$$\begin{aligned} \frac{\mathrm{d}N}{\mathrm{d}m} = | \ \mathrm{B.G.}(m) &+ A_{\mathrm{f_0(980)}} \quad F_{\mathrm{K\overline{K}}}(m) \quad \exp^{i\delta_1} \\ &+ A_{\mathrm{f_0(1500)}} \quad \mathrm{BW}_{\mathrm{f_0(1500)}}(m) \quad \exp^{i\delta_2} \\ &+ A_{\theta/\mathrm{f_J(1710)}} \quad \mathrm{BW}_{\theta/\mathrm{f_J(1710)}}(m) \quad \exp^{i\delta_3} \ |^2. \end{aligned}$$

where A_i and BW_i are the normalisations and amplitudes of the Breit-Wigner functions used to describe the resonances, and δ_i are the phase angles describing the interference between the resonances and the background. The resulting fit is shown in figure 7.1a, the fit parameters yielded are consistent with the PDG [72] values for these resonances, and are given in table 7.1.

The $\mathrm{D_0}$-wave contains the second greatest activity (~10%) of the $\mathrm{K^+K^-}$ data and a fit has been performed to this wave in the mass range of 1·2 GeV/c^2 to 2·7 GeV/c^2 using three incoherent Breit-Wigners to describe the $\mathrm{f_2}$(1270)/$\mathrm{a_2}$(1320), $\mathrm{f_2'}$(1525) and a broad structure at ~2·15 GeV/c^2, in addition to a background of the form given by equation 7.1. The parameters for the peak at 1·3 GeV/c^2 fall between the PDG values for the $\mathrm{f_2}$(1270) and $\mathrm{a_2}$(1320), the values for the $\mathrm{f_2'}$(1525) are compatible with the PDG values, and those for the broad peak at 2·15 GeV/c^2 are compatible with those of the $\mathrm{f_2}$(2150).

The resulting fit is shown in figure 7.1b, the parameters from which are also given in table 7.1. There is some activity at masses of $m_{\mathrm{K^+K^-}} < 1{\cdot}2$ GeV/c^2, but this

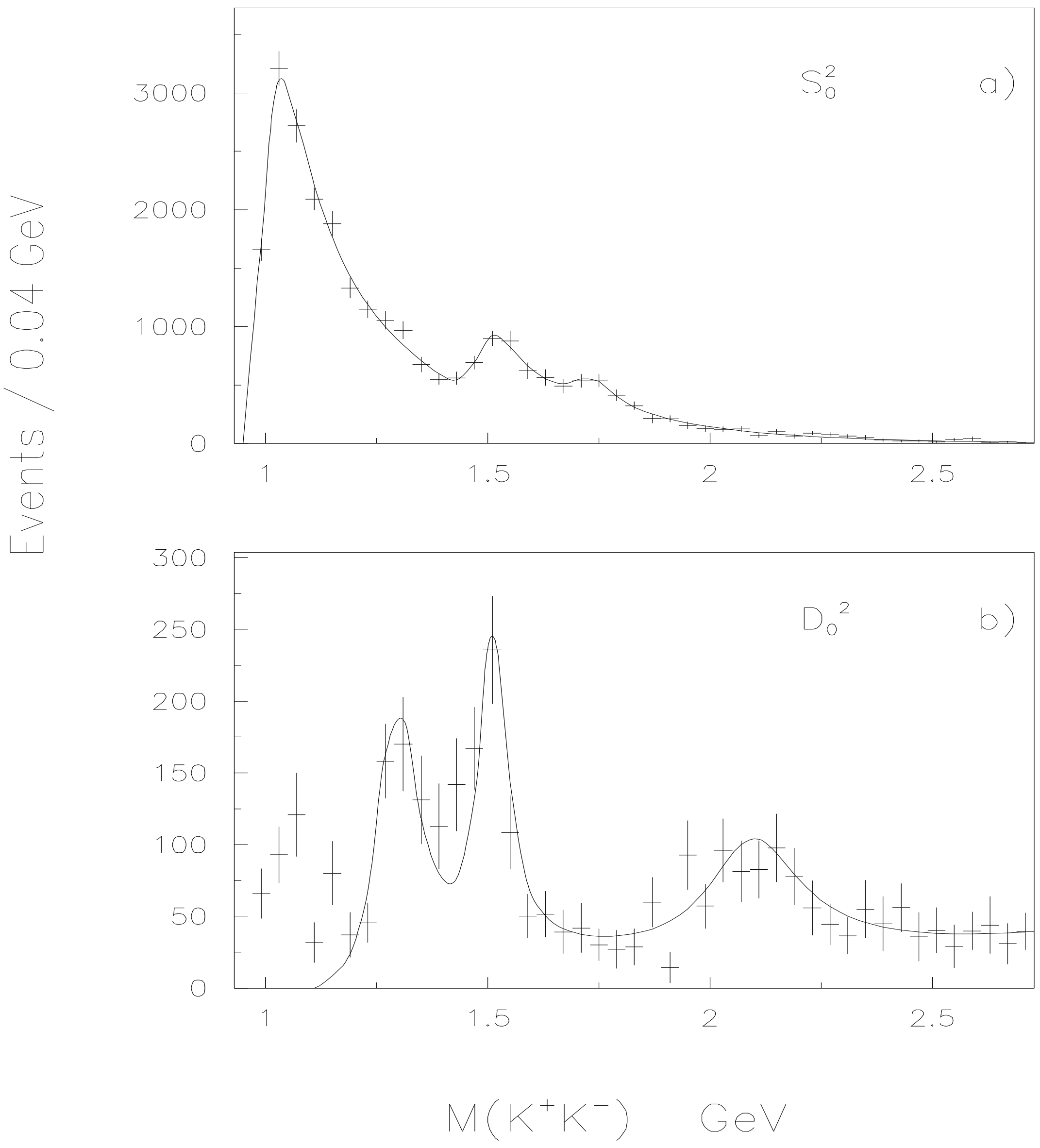

Figure 7.1: Fits to the (a) S-wave and (b) D_0-wave.

is somewhat erratic, and when considering its origin it should be borne in mind that this is too low in mass to be a D-wave resonance, and it is also very unlikely to be D-wave phase-space as it is near threshold where the central system would have a small breakup momentum. In addition to this, Monte Carlo studies have consistently shown that S-wave feeds through to a small degree to the D_0-wave throughout the mass spectrum, and that this feed-through increases in quantity to a maximum at threshold. This effect is due to the acceptance correction quality deteriorating somewhat near threshold, and it appears likely that this is the source of the small quantity of activity in the D_0-wave at $m_{K^+K^-} < 1{\cdot}2$ GeV/c^2.

Table 7.1: Masses and widths of the resonances contained in the K^+K^- mass spectrum, resulting from a simple fit to the partial waves.

Resonances	Mass (MeV/c^2)	Γ (MeV/c^2)
$f_0(980)$	985 ± 10	65 ± 20
$f_0(1500)$	1497 ± 10	104 ± 25
$f_0(1710)$	1730 ± 15	100 ± 25
$f_2(1270)/a_2(1320)$	1305 ± 20	132 ± 25
$f_2'(1525)$	1515 ± 15	70 ± 25
$f_2(2150)$	2130 ± 35	270 ± 50

The waves P_0, P_-, P_+, D_-, and D_+ contain only ∼10% of the total mass spectrum among them, and contain little information that is statistically meaningful. The P-waves display little activity, and that which there is generally fluctuates from mass-bin to mass-bin, which is consistent with the small level of structureless feed-through from the S-wave observed in Monte Carlo studies. An exception may be in the P_0-wave where the bin containing the greatest number of events appears to be consistent with a small signature of $\phi(1020)$ production, as has been observed previously in K^+K^- mass spectra published by the WA76 collaboration [68]. However, the bin is not statistically significant and comments on its origin are merely conjecture. The D_- and D_+-waves both contain some activity, but which is statistically limited, and cannot be easily ascribed to either resonances, feed-through, or phase-space because of this limitation. For these reasons nothing is gained from fitting the P_0, P_-, P_+, D_- or D_+-waves, and so only the S-wave and D_0-wave which contain ~90% of the K^+K^- data between them are fitted.

In summary, it has been shown that the K^+K^- mass spectrum is dominated by S-wave phase-space and resonances, with the only other significant activity being in the D_0-wave. Other waves contain small levels of activity which are not statistically significant, and that are consistent with feed-through from the S-wave. The S-wave resonances are identified with the $f_0(980)$, $f_0(1500)$, and a spin-zero $\theta/f_J(1710)$. The $\theta/f_J(1710)$ is clearly present in the S-wave and is absent in the D-waves at the statistical level of the data. This conclusively demonstrates that the $\theta/f_J(1710)$ is a spin-zero resonance. The D_0-wave resonances are identified with the $f_2(1270)/a_2(1320)$, $f_2'(1525)$, and $f_2(2150)$.

7.2 Review of Main Components of PWA

This section summarises the key points when considering the quality of the analysis with particular emphasis placed on the ability of the analysis methods to determine an S-wave resonance. It also covers the key areas in the analysis where errors may be introduced, and of the effect of these errors.

7.2.1 Studies in Fitting the Moments

The acceptance correction has been examined with Monte Carlo studies and has been found to be generally of a high quality, as discussed in section 6.12. It has also been found that regions tending towards a lower quality of acceptance correction, such as that for a pure D_0-wave phase-space above 2·4 GeV/c^2 are detectable, as demonstrated in section 6.12.2. This localised lower quality region has been found to not affect the analysis of the real data, as can be seen from the close comparison between the reproduced moments from the fit and the experimental moments, shown in section 6.13.

Even with a good quality acceptance correction process, adverse effects originating from essential simplifications and approximations during the calculation of the acceptance tables, do corrupt the acceptance corrected data to some degree. It has been found from Monte Carlo studies that the effect of imperfect acceptance tables is manifested as feed-through from the S-wave into the D_0-wave. It has also been observed during Monte Carlo studies that the D_0-wave has never been found to feed through to other waves. The reason for the feed-through having been found to only travel in the direction of higher spin waves can be illustrated by an example. If a flat S-wave angular distribution is corrupted by an imperfect acceptance correction, then the corrupted distribution can be interpreted as a combination of other, higher waves; however, it has been found that a corrupted D_0-wave distribution cannot easily be described by combinations of waves of lower spins. Although it is probable that waves of higher spins could form combinations to describe the corrupted D_0-wave distribution, there are none available in this analysis as is justified by the experimental moments.

This has the effect, at the stage of fitting the moments, of resisting the feeding-through of D_0-waves into waves of a lower spin, such that the S-wave has never been found to be mistakenly assigned events from higher spin waves.

7.2.2 Fitting the 1996 K^+K^- Experimental Moments

The experimental moments have been fitted well throughout the mass spectrum. The fact that the data have been so well matched augments the belief that the experimental data has been generally acceptance corrected well, as it has been shown from Monte Carlo studies that regions of moments that have been acceptance corrected poorly are not usually able to be fitted well, as they are generally distorted into a self-inconsistent set.

7.2.3 Linking the Ambiguous Solutions

As can be seen from figure 6.21a the real parts of the roots of the complex polynomial equation 6.11 have been linked well, whereas the imaginary parts have proven to be less significant in the linking process as they hold much less information about the appropriate linking. The linked roots of the real data are a typical example of a set of correctly linked roots as observed during Monte Carlo investigations, *i.e.* the real parts are smooth, as opposed to having discontinuous trajectories from mass-bin to mass-bin; and the imaginary parts contain little information.

Using Monte Carlo investigations it has been found that if phase-space or resonances are spin-two, then their eight solutions are identical. This is another manifestation of the fact that a D_0-wave angular distribution cannot be constructed from combinations of lower waves, and it has the consequence that if an incorrect ambiguous solution of genuine S-wave events were chosen, then it could be mistaken as D_0-wave, but if an incorrect ambiguous solution of genuine D_0-wave events were chosen then it could not be mistaken for S-wave, as the ambiguous solutions in this case are identical and correct. This is the case even if there is a poor linking of the roots, or even no linking at all.

The chosen solution is the only candidate which passes the physical constraints imposed.

7.2.4 Summary

The topics in this section have reviewed the key areas of the partial wave analysis. It has put forward reasons for confidence in their execution, and explained the way in which known sources of errors and/or inaccuracies have been found to affect the results.

Although not necessary to the analysis, it is advantageous to have found that in the two major areas of the analysis in which limited quantities of errors are known to be introduced (namely the fitting of the moments, and the linking of the roots) it has been found that during Monte Carlo studies D_0-wave contributions to a mass spectrum have never fed-through to waves of a lower spin. Thus D_0-wave resonances and/or phase-space in the experimental data will not be misidentified as S-wave as a result of the known sources of errors.

7.3 Comparison with Other Experiments

It must initially be commented upon that the WA76 collaboration have published a spin-analysis of the K^+K^- channel which finds contradictory results to this analysis. However, there are several reasons why the results from the current analysis can safely be considered to supersede the WA76 result, and these reasons are put forward. This is followed by other results that are compatible with the findings of this analysis.

7.3.1 The WA76 Collaboration

The WA76 collaboration have published [68] a spin-analysis of 4079 K^+K^- events from the central production interaction,

$$\mathrm{pp} \longrightarrow \mathrm{p_f}(\mathrm{K^+K^-})\mathrm{p_s},$$

the mass spectrum from which is shown in figure 3.9 on page 51. The analysis finds that the structure in the 1·5 GeV/c^2 region is spin-two and therefore should be identified with the $f_2'(1525)$. It also finds that the structure in the 1·7 GeV/c^2

region, identified with the $\theta/\mathrm{f_J}(1710)$, was favoured to be spin-two based upon the $\cos\theta$ distributions obtained.

Although the author of this thesis was not involved in the WA76 publication, and so cannot comment directly upon the quality of the analysis, there are several significant reasons why the current analysis can be considered to be superior, and hence supersede the WA76 result.

Experimental:

The K^+K^- data obtained by the 1996 run of the WA102 experiment represents over a factor of five increase in statistics compared with the WA76 data.

Theoretical:

It is essential for a meaningful analysis to use an appropriate method to deal with the inherent ambiguities in the partial wave analysis. However, the issue of ambiguities was not addressed in the WA76 analysis.

Analytical:

A major limitation of the WA76 analysis is that it was not performed using small mass intervals, but that only two mass-slices were taken, one around the 1·5 GeV/c^2 region, and one around the 1·7 GeV/c^2 region. This prevents an effective acceptance correction as it is known that the $\{\cos\theta, \phi\}$ acceptance correction distributions vary as a function of mass. Although the $\{\cos\theta, \phi\}$ distributions vary smoothly and slowly from mass-bin to mass-bin in 40 MeV/c^2 intervals, it is also true that the acceptance correction needs to be accurate from mass-bin to mass-bin and cross-checked using Monte Carlo studies to investigate the level of feed-through from one wave to another, and particularly from the S-wave to the $\mathrm{D_0}$-wave. This may be particularly significant as it has been found during the Monte Carlo studies for this analysis that the level of feed-through into the D_0-wave becomes an increasing problem as the quality of the acceptance correction reduces.

Other aspects of the analysis which may have contributed to the difference in the two results are that the Monte Carlo simulation used by the WA102 collaboration has undergone substantial investigation and improvements since the WA76 result was published. In addition to this, the available computational processing power has greatly increased, which allows the generation of acceptance tables with far greater statistics, and enables the processor-intensive Monte Carlo investigations presented in this thesis to be performed. A further consideration is the selection of the K^+K^- channel; for example, the removal of diffractive contamination which is evident as 'hotspots' at the mirrors of the Čerenkov detector has been found to be essential for this analysis, but was not reported on with reference to the corresponding WA76 analysis.

7.3.2 The E690 Collaboration

The E690 collaboration have published [59] an analysis of the $K^0_S K^0_S$ channel from the central production interaction,

$$\mathrm{pp} \longrightarrow \mathrm{p_f}(K^0_S K^0_S)\mathrm{p_s},$$

the mass spectrum from which is shown in figure 3.6 on page 46. As can be seen the mass spectrum is very similar to that of the K^+K^- mass spectrum used in this analysis (shown in figure 5.10b on page 94). The E690 collaboration have performed a partial wave analysis on the 11182 events from threshold to 2 GeV/c^2 and obtained two ambiguous solutions, as expected when only S and D-waves can be present. One of the solutions is mostly S-wave while the other is mostly D-wave, and so the solution with very small S-wave at threshold can be eliminated. The structure in the 1·5 GeV/c^2 region is thus found to be spin-zero, and so is identified with the $f_0(1500)$. There is, however, a problem with the identification of the spin of the $\theta/f_J(1710)$, as the complex roots of the polynomial equation governing the ambiguities cross the real axis at 1·58 GeV/c^2 causing a *bifurcation*. The solution dominated by S-wave at threshold bifurcates at 1·58 GeV/c^2 into two solutions, one of which has a large S-wave contribution, and the other of which has large D-wave contributions. For this reason the E690 analysis is able to identify the $f_0(1500)$, but is not able to determine the spin of the $\theta/f_J(1710)$.

It can be seen from figure 6.21b on page 140 that the imaginary roots do not go below zero. This demonstrates that the roots from this analysis do not cross the real axis, and so the problem of bifurcation is not encountered.

7.3.3 The WA102 Collaboration's $K^0_S K^0_S$ Channel

The WA102 collaboration's $K^0_S K^0_S$ channel is of lower statistics than the K^+K^- channel and as a result has been analysed in wider (80 MeV/c^2) mass intervals. Two ambiguous solutions are found, one of which is dominated by D-waves at threshold and low masses, and which therefore can be eliminated. The S, D_0, D_-, and D_+-waves from the physical solution are shown in figure 7.2. Although statistically limited it can be seen that as in the case of the K^+K^- physical solution the S-wave contains a threshold enhancement and structures in the ∼1·5 GeV/c^2 and ∼1·7 GeV/c^2 regions. A fit using the resonance parameters resulting from the fit to the higher statistics K^+K^- S-wave is superimposed on the $K^0_S K^0_S$ S-wave in figure 7.2a, and demonstrates the compatibility of the K^+K^- and $K^0_S K^0_S$ S-waves.

7.3.4 The MARK III Collaboration

The MARK III collaboration have published [67] an analysis of the K^+K^- and $K^0_S K^0_S$ channels from the decays,

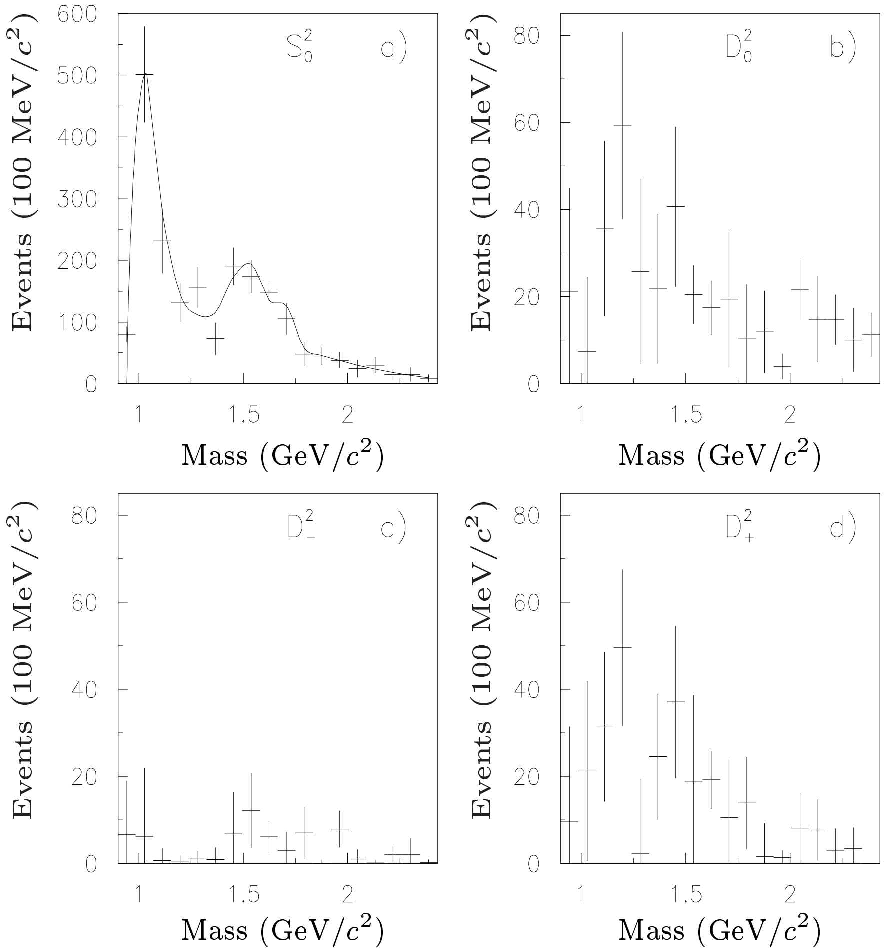

Figure 7.2: The physical solution from the PWA of the WA102 $K_S^0K_S^0$ data. Superimposed on the S-wave is a fit that uses the resonance parameters resulting from the fit to the higher statistics WA102 K^+K^- data.

$$J/\Psi \longrightarrow \gamma(K^+K^-) \qquad \text{and} \qquad J/\Psi \longrightarrow \gamma(K^0_S K^0_S).$$

The angular analyses of the 1755 K^+K^- events and 582 $K^0_S K^0_S$ events give very similar results. The combined $K\overline{K}$ mass spectrum shows peaks in the 1·5 GeV/c^2 and 1·7 GeV/c^2 regions, from which an angular analysis of the data finds large S-wave contributions at ∼1·7 GeV/c^2. The D-wave distributions show clear signals corresponding to the $f_2'(1525)$, while there is no evidence for significant structure in the D-waves in the vicinity of 1·7 GeV/c^2. However, it is noted that within the present uncertainties the existence of small contributions cannot be excluded.

7.4 dP_T Dependence of the K^+K^- Mass Spectrum

The recently discovered phenomenon of a glueball/$q\overline{q}$ filter based upon the production dependence of a state on the kinematical variable dP_T (see page 23) makes the dP_T dependence of the K^+K^- mass spectrum an interesting quantity when considering the possible gluonic nature of resonances within that mass spectrum. The three dP_T ranges $dP_T < 0{\cdot}3$ GeV/c, 0·3 GeV/c<dP_T< 0·5 GeV/c, and dP_T> 0·5 GeV/c are shown in figures 7.3a, 7.3b, and 7.3c respectively.

The $f_0(980)$ is enhanced in the low dP_T range, and suppressed in the high dP_T range. Although this is consistent with the behaviour found for glueballs and the $f_0(980)$ is not considered to be a glueball candidate, it has been observed that the $f_0(980)$ possesses a dP_T dependence akin to the glueball candidates[1]. The peak in the 1·5 GeV/c^2 region is prominent in the low dP_T region, as is expected for a glueball candidate, and yet is enhanced in the high dP_T region as is expected for a conventional $q\overline{q}$ meson. As the PWA results reveal that there are both the glueball candidate $f_0(1500)$ and established $q\overline{q}$ meson $f_2'(1525)$ in this mass region, the simplest interpretation of the observed dP_T dependence of the 1·5 GeV/c^2 mass

[1]The reason for this is not yet fully understood. However, the $f_0(980)$ is not considered to be a conventional $q\overline{q}$ meson, and it seems likely that this is not a coincidence.

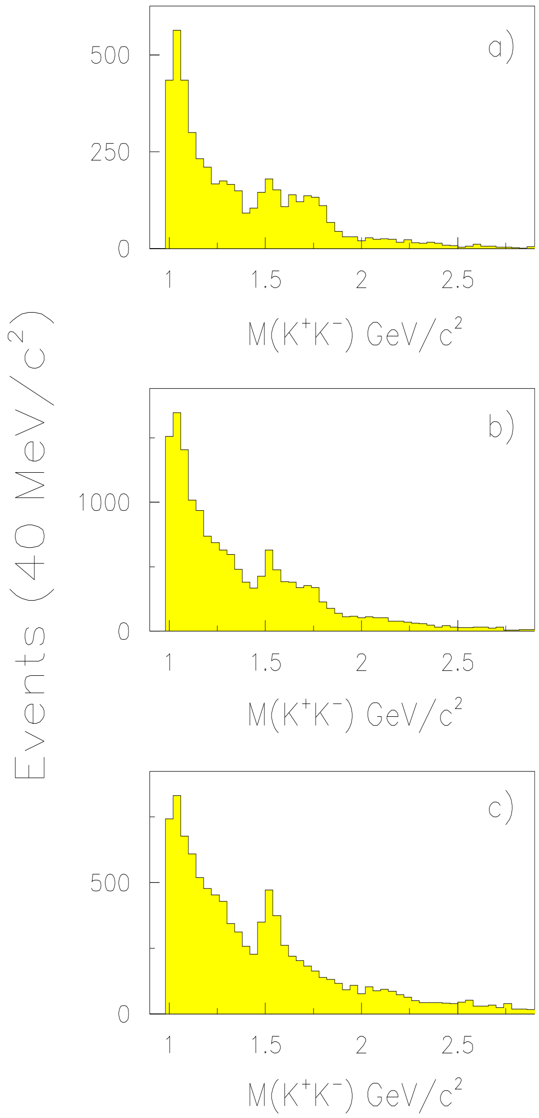

Figure 7.3: The K^+K^- mass spectrum in three dP_T regions of (a) $dP_T < 0{\cdot}3$ GeV/c, (b) $0{\cdot}3$ GeV/c<dP_T< $0{\cdot}5$ GeV/c, and (c) dP_T> $0{\cdot}5$ GeV/c.

region based upon present knowledge is that the $f_0(1500)$ is dominating the mass spectrum at low dP_T, and the $f_2'(1525)$ is dominating the mass spectrum at high dP_T. The actual situation, however, can only be clarified by a PWA applied to the individual dP_T regions. The peak in the 1·7 GeV/c^2 region is prominent in the low dP_T region and absent in the high dP_T region. It is therefore consistent with being a glueball candidate and inconsistent with being a $q\overline{q}$ meson. The $f_2(2150)$ is not observed in the low dP_T sample, but is found to be produced in the high dP_T sample, which is consistent with it being a $q\overline{q}$ meson.

Chapter 8

Conclusion

8.1 Summary of Analysis

A full partial wave analysis, including the appropriate ambiguity analysis, has been performed on the comparatively high statistics sample of 30868 centrally produced K^+K^- events from the 1996 run of the WA102 experiment. The primary objective of the analysis was to identify the spin of the $\theta/f_J(1710)$.

Monte Carlo studies have been used to thoroughly investigate the behaviour and applicability of the acceptance correction methods, moments, and partial wave analysis — comprising the fitting of the data, the treatment of ambiguities, and the linking of the ambiguous solutions — and have shown that the analysis is valid. Monte Carlo studies have also been used to investigate the sources, and effects of, errors which may be incorporated into the analysis, and have shown that the limited errors introduced do not prevent a reliable spin extraction from being performed. In addition to this, an interesting aspect of the analysis was discovered which further increases confidence that there are no peaks in the S-wave extracted by the partial wave analysis that are due to feed-through from higher waves. The reason for this is that in two key areas where it has been found that small errors can be incorporated into the analysis, namely the fitting of the moments and the linking of the ambiguous solutions, it has been found that although S-wave can incorrectly feed through into waves of higher spin, the feeding-through of D_0-wave data into waves of a lower spin has never been observed during the Monte Carlo investigations.

8.2 Summary of Results

A partial wave analysis has been used to extract the partial waves comprising the K^+K^- mass spectrum, and a simple fit has been applied. The partial wave analysis shows that the K^+K^- mass spectrum is dominated by S-wave resonances and phase-space, and the D_0-wave is the only other wave with statistically significant activity. The remaining waves contain only low-level activity, consistent with the feed-through from other waves known to exist from Monte Carlo studies. The S-wave is dominated at threshold by production of the $f_0(980)$, while the structures in the 1·5 GeV/c^2 and 1·7 GeV/c^2 regions represent the most significant results of the analysis. The structure in the 1·5 GeV/c^2 region appears clearly in the S-wave and is identified with the scalar glueball candidate, the $f_0(1500)$. The primary objective of this analysis was to measure the spin of the $\theta/f_J(1710)$ which it is known can be either spin-zero or spin-two. The $\theta/f_J(1710)$ appears clearly in the S-wave, while there is no statistically significant activity in the 1·7 GeV/c^2 region in the D-waves. These results demonstrate that the $\theta/f_J(1710)$ is unambiguously an S-wave particle. The D_0-wave contains evidence for $f_2(1270)/a_2(1320)$, $f_2'(1525)$ and $f_2(2150)$.

8.3 Consequences of the Spin-Zero $\theta/f_J(1710)$

The S-wave $f_0(1710)$ has significant implications in the search for glueballs. Its presence means that there are now three confirmed isoscalar scalar states in the mass region of the ground-state scalar nonet, namely the $f_0(1370)$, $f_0(1500)$ and $f_0(1710)$.

The quark model can accommodate only two of these particles, and this represents firm evidence that physics beyond the quark model is necessary. The only plausible explanation is the presence of a scalar glueball. Although the glueball has long been predicted by QCD, it is only now, with firm evidence of the three scalars in this region that the glueball is *definitely required* as an explanation of the experimentally observed situation.

There are now considered to be two good candidates for the scalar glueball for reasons given in section 3.3, which include their production in glue-rich production mechanisms, compatibility with the mass range predicted by lattice QCD calculations, decay widths in radiative J/Ψ decays, and dP_T dependences. The candidates are the $f_0(1500)$ and the $f_0(1710)$, while no other states are compatible with the set of characteristics predicted for the scalar glueball.

Further evidence for the gluonic nature of the $f_0(1710)$ has been presented in section 7.4, as the production of the $f_0(1710)$ is dominantly at small dP_T ($< 0{\cdot}3$ GeV/c) and negligible at high dP_T ($> 0{\cdot}5$ GeV/c). This is consistent with the behaviour exhibited by glueball candidates, and inconsistent with the behaviour exhibited by established $q\overline{q}$ states[1], as discussed in section 2.5.2. It is also interesting to note that the two results — the measured spin of the $f_0(1710)$, and its dP_T dependence — are consistent with the prediction based upon radiative J/Ψ decays [22] that a spin-two $\theta/f_J(1710)$ would be consistent with being a $q\overline{q}$ state, whereas a spin-zero $\theta/f_J(1710)$ is consistent with being a glueball, or a mixed $q\overline{q}$-glueball that has a large glueball component.

It also must be remembered that the question of which glueball candidate is the scalar glueball is complicated by the expectation that mixing will occur between the

[1] A quantitative measure of the dP_T dependence of the $f_0(1710)$ would require a PWA of separate dP_T regions. However, in the $1{\cdot}7$ GeV/c^2 region the dP_T dependence of the whole mass spectrum can be expected to be very similar to the dP_T dependence of the S-wave, as it has been shown from the PWA that there is no significant activity in partial waves other than the S-wave in this mass region.

three isoscalar scalars, as discussed in section 3.7. Amsler and Close propose a possible scenario for the mixing in which the bare glueball lies between the $\frac{1}{\sqrt{2}}(u\overline{u} + d\overline{d})$ and the $s\overline{s}$ members of the nonet in mass, leading to an approximately equal sharing of the wavefunction of the glueball between the observed $f_0(1500)$ and the $f_0(1710)$ states. Weingarten proposes an alternative scenario for the mixing, in which the bare glueball lies above both the $\frac{1}{\sqrt{2}}(u\overline{u} + d\overline{d})$ and $s\overline{s}$ members of the nonet in mass, leading to the glueball being dominantly embodied in the observed $f_0(1710)$.

8.4 Potential Future Developments

The ground state scalar glueball is definitely required to explain the experimentally observed situation in the scalar sector. There are two candidates for the scalar glueball, but with the near-complete decline of meson spectroscopy, is it too late to determine the distribution of the bare glueball among the physical states, and hence the physical manifestation of the glueball? An imminent possibility is a partial wave analysis of the WA102 collaboration's K^+K^- data in separate dP_T regions, which could provide valuable information on this subject, as its properties as a glueball filter may be able to differentiate between the strengths of the glueball component in the two glueball candidates. A second likely source of information is from the active field of lattice QCD, from which regular improvements in techniques frequently produce predictions about the scalar glueball with ever increasing accuracy. Less immediate sources of information include results from $\gamma\gamma$ fusion experiments and radiative J/Ψ decays.

Although, in the main, the dedicated glueball searches have now completed their data taking, there is still potential for further new and exciting developments. A study of Double Pomeron Exchange (DPE) interactions has been proposed [96] using the ALICE detector at the LHC which, if accepted, would provide the opportunity to study glueballs at higher centre-of-mass energies. This would allow studies beyond the present limits on the mass of the glueball, currently at $\sim 2{\cdot}5$ GeV/c^2, while providing a purer gluonic environment than is presently available due to the $\sqrt{s}$ dependence of the DPE interaction cross-section. If the proposal is successful, then the experiment could make discoveries of some of the many glueballs from the rich glueball spectrum that is predicted. The opportunity to discover further glueballs is entwined with the opportunity to learn more about the dP_T glueball/$q\overline{q}$ filter, as the dP_T phenomenon is known to be able to distinguish between glueball and $q\overline{q}$ states, so newly discovered glueballs will yield more information about the dP_T mechanism, aiding attempts to properly understand this unexpected facet of QCD.

Appendix A

Ehrlich Mass Squared

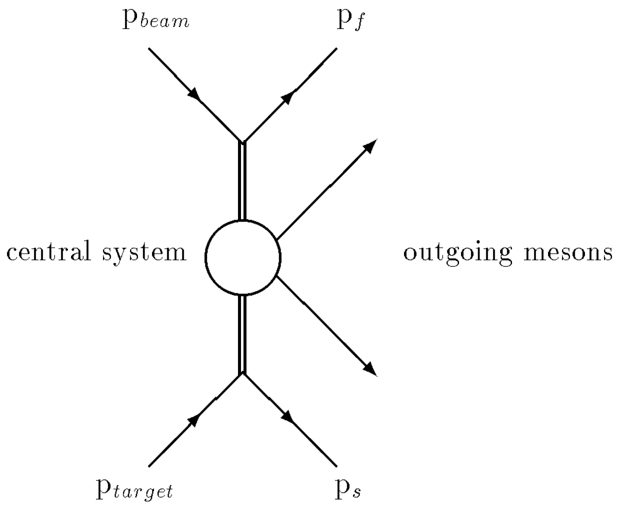

Figure A.1: The central production mechanism in the centre-of-mass frame.

The Ehrlich mass squared [80] for the reaction shown in figure A.1 is defined in the following way. Let E_{b}, E_{t}, E_{f}, E_{s}, E_+ and E_- refer to the energies of the beam, target, fast, slow, positive central and negative central particles respectively, and p_{b}, p_{t}, p_{f}, p_{s}, p_+ and p_- refer to their respective momenta. Then by conservation of energy,

$$E_{\mathrm{b}} \;+\; \mathrm{m_p} \;=\; E_{\mathrm{f}} \;+\; E_{\mathrm{s}} \;+\; E_{+} \;+\; E_{-},$$

where $\mathrm{m_p}$ is the mass of the proton. Therefore,

$$\begin{aligned}(E_{\mathrm{b}} - E_{\mathrm{f}} - E_{\mathrm{s}} + \mathrm{m_p})^2 &= (E_{+} + E_{-})^2, \\ &= E_{+}^2 + E_{-}^2 + 2E_{+}E_{-}, \\ &= \mathrm{m}_{+}^2 + p_{+}^2 + \mathrm{m}_{-}^2 + p_{-}^2 + 2(\mathrm{m}_{+}^2\mathrm{m}_{-}^2 + \mathrm{m}_{+}^2 p_{-}^2 + \mathrm{m}_{-}^2 p_{+}^2 + p_{+}^2 p_{-}^2)^{\frac{1}{2}}.\end{aligned}$$

Now suppose that the positive and negative particles have identical masses (called the Ehrlich mass), the Ehrlich mass squared can then be calculated using the energies and momenta of the particles involved in the interaction.

$$(E_{\mathrm{b}} - E_{\mathrm{f}} - E_{\mathrm{s}} + \mathrm{m_p})^2 = 2m_{_{\mathrm{Ehrl}}}^2 + p_{+}^2 + p_{-}^2 + 2(m_{_{\mathrm{Ehrl}}}^4 + m_{_{\mathrm{Ehrl}}}^2(p_{-}^2 + p_{+}^2) + p_{+}^2 p_{-}^2)^{\frac{1}{2}}.$$

Then,

$$\begin{aligned}&[(E_{\mathrm{b}} - E_{\mathrm{f}} - E_{\mathrm{s}} + \mathrm{m_p})^2 - p_{+}^2 - p_{-}^2]^2 = \\ &\qquad 4[m_{_{\mathrm{Ehrl}}}^4 + 2m_{_{\mathrm{Ehrl}}}^2(m_{_{\mathrm{Ehrl}}}^4 + m_{_{\mathrm{Ehrl}}}^2(p_{-}^2 + p_{+}^2) + p_{+}^2 p_{-}^2)^{\frac{1}{2}} \\ &\qquad + m_{_{\mathrm{Ehrl}}}^4 + m_{_{\mathrm{Ehrl}}}^2(p_{-}^2 + p_{+}^2) + p_{+}^2 p_{-}^2)],\end{aligned}$$

and hence,

$$\begin{aligned}&[(E_{\mathrm{b}} - E_{\mathrm{f}} - E_{\mathrm{s}} + \mathrm{m_p})^2 - p_{+}^2 - p_{-}^2]^2 - [2p_{+}p_{-}]^2 = \\ &\qquad 4m_{_{\mathrm{Ehrl}}}^2[2m_{_{\mathrm{Ehrl}}}^2 + 2(m_{_{\mathrm{Ehrl}}}^4 + m_{_{\mathrm{Ehrl}}}^2(p_{-}^2 + p_{+}^2) + p_{+}^2 p_{-}^2)^{\frac{1}{2}} + p_{+}^2 + p_{-}^2)].\end{aligned}$$

Using,

$$(E_{+} + E_{-})^2 = 2m_{_{\mathrm{Ehrl}}}^2 + p_{+}^2 + p_{-}^2 + 2(p_{+}^2 p_{-}^2 + m_{_{\mathrm{Ehrl}}}^2(p_{+}^2 + p_{-}^2) + m_{_{\mathrm{Ehrl}}}^4)^{\frac{1}{2}},$$

gives,

$$[(E_\mathrm{b} - E_\mathrm{f} - E_\mathrm{s} + \mathrm{m_p})^2 - p_+^2 - p_-^2]^2 - [2p_+p_-]^2 = 4m_{\mathrm{Ehrl}}^2(E_+ + E_-)^2,$$
$$= 4m_{\mathrm{Ehrl}}^2(E_\mathrm{b} - E_\mathrm{f} - E_\mathrm{s})^2,$$

and therefore the Ehrlich mass squared is given by,

$$m_{\mathrm{Ehrl}}^2 = \frac{[(E_\mathrm{b} - E_\mathrm{f} - E_\mathrm{s})^2 - p_+^2 - p_-^2]^2 - [2p_+p_-]^2}{4[E_\mathrm{b} - E_\mathrm{f} - E_\mathrm{s}]^2}.$$

A plot of m_{Ehrl}^2 for all events of the type shown in figure A.1 will thus show peaks at the square of the mass of the central particles, and therefore allow different central systems, such as $\pi^+\pi^-$, $\mathrm{K^+K^-}$, and $\mathrm{p\overline{p}}$, to be separated. Using this method results in events with large momentum errors being distributed further from their central peak than the same central system with small momentum errors, which allows the worst measured events to be eliminated using an m_{Ehrl}^2 cut. It also provides an estimate of the experimental mass resolution.

Appendix B

Unphysical Ambiguous Solutions

Due to the nature of the partial wave analysis, eight mathematically equivalent ambiguous sets of solutions for the partial waves arise. When investigating real data, or data that is similar to real data in that it is dominated by S-wave at or near threshold, it has always proven possible to reject seven of these solutions based upon physical arguments. The criterion used is that at, and close to threshold (in the absence of a non-spin-zero resonance) the mass spectrum should be dominated by S-wave. This appendix contains the sets of partial waves which have been rejected as being unphysical. Section B.1 contains the unphysical solutions from the PWA of pure S-wave generated by Monte Carlo, and section B.2 contains the unphysical solutions from the PWA of the 1996 K^+K^- experimental data.

B.1 Unphysical Solutions: S-wave Phase-Space

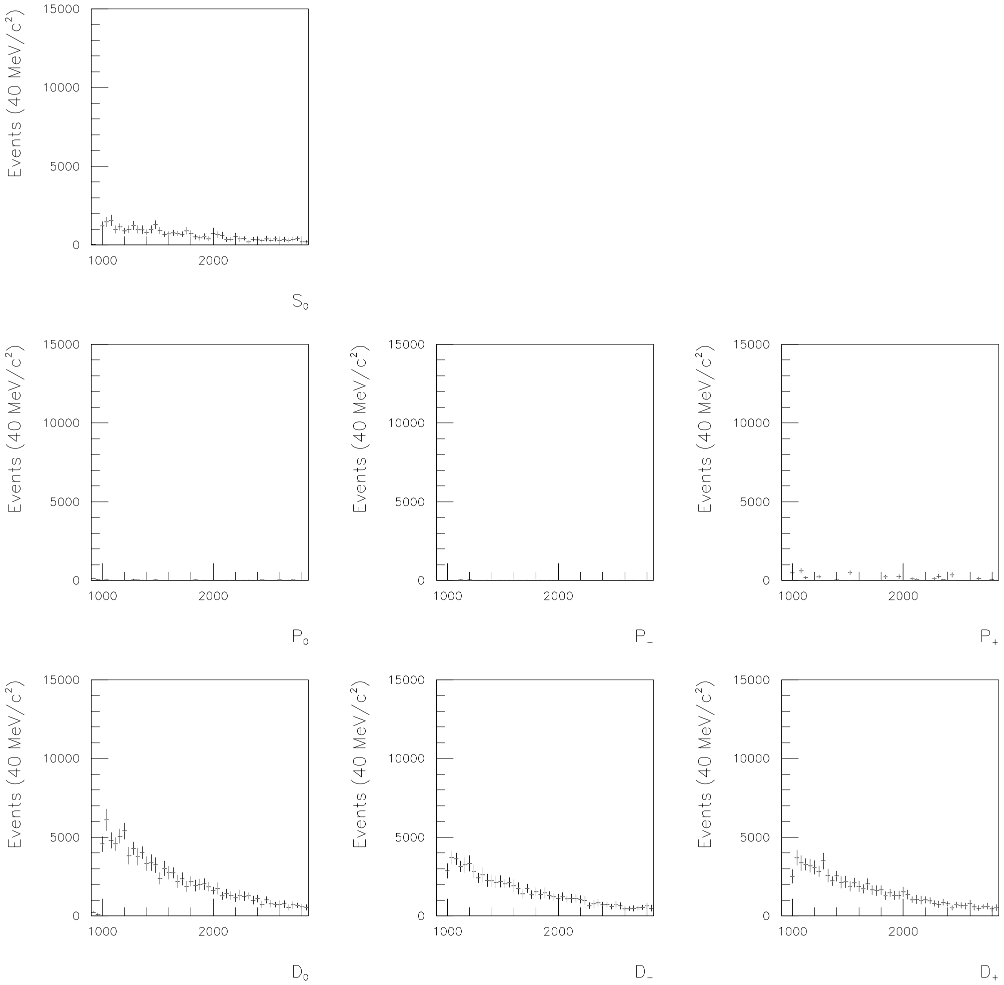

Figure B.1: Solution 1 rejected as being unphysical, from the PWA of an S-wave phase-space.

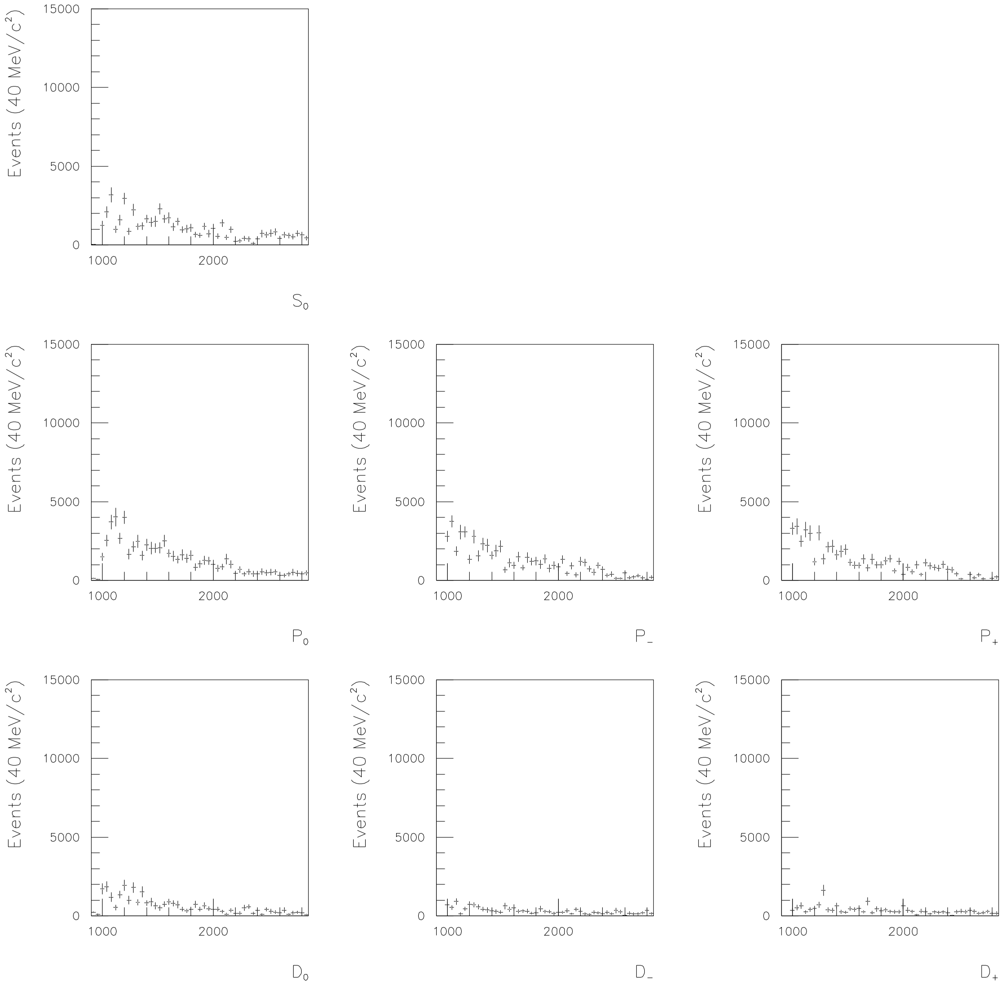

Figure B.2: Solution 2 rejected as being unphysical, from the PWA of an S-wave phase-space.

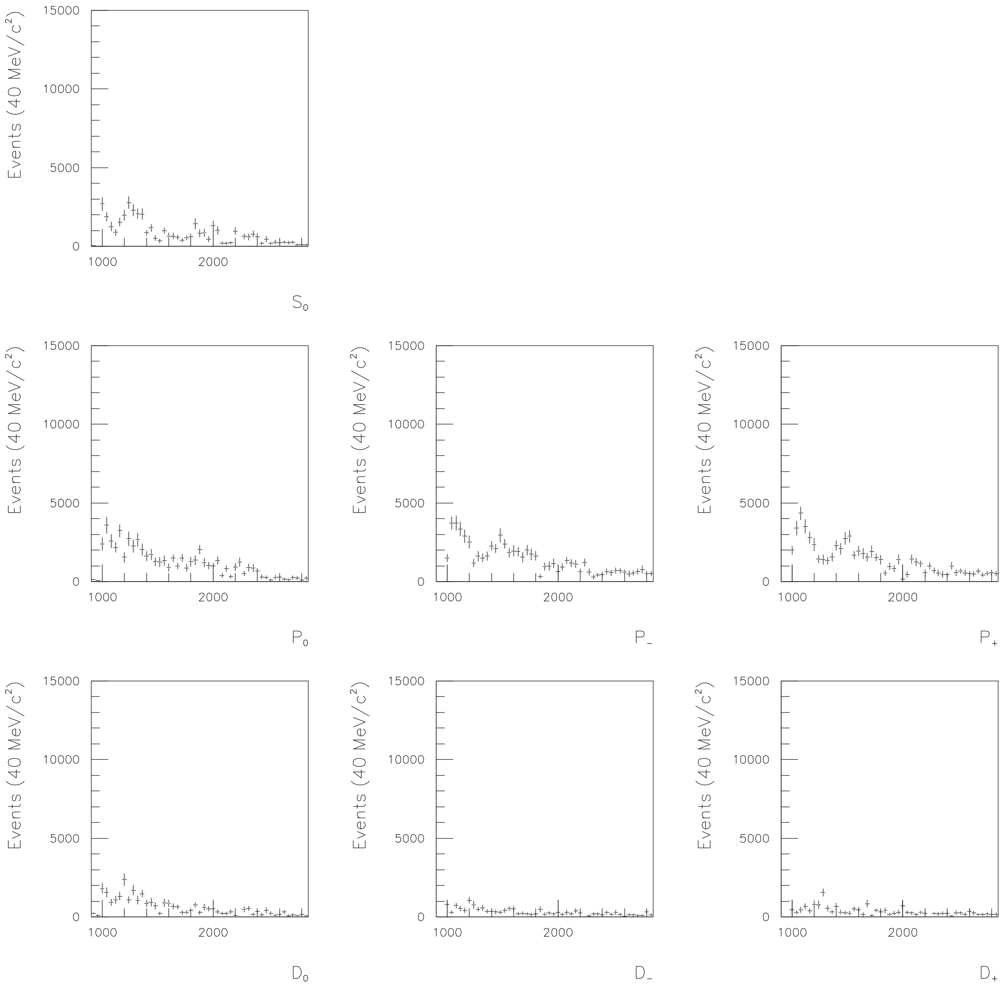

Figure B.3: Solution 3 rejected as being unphysical, from the PWA of an S-wave phase-space.

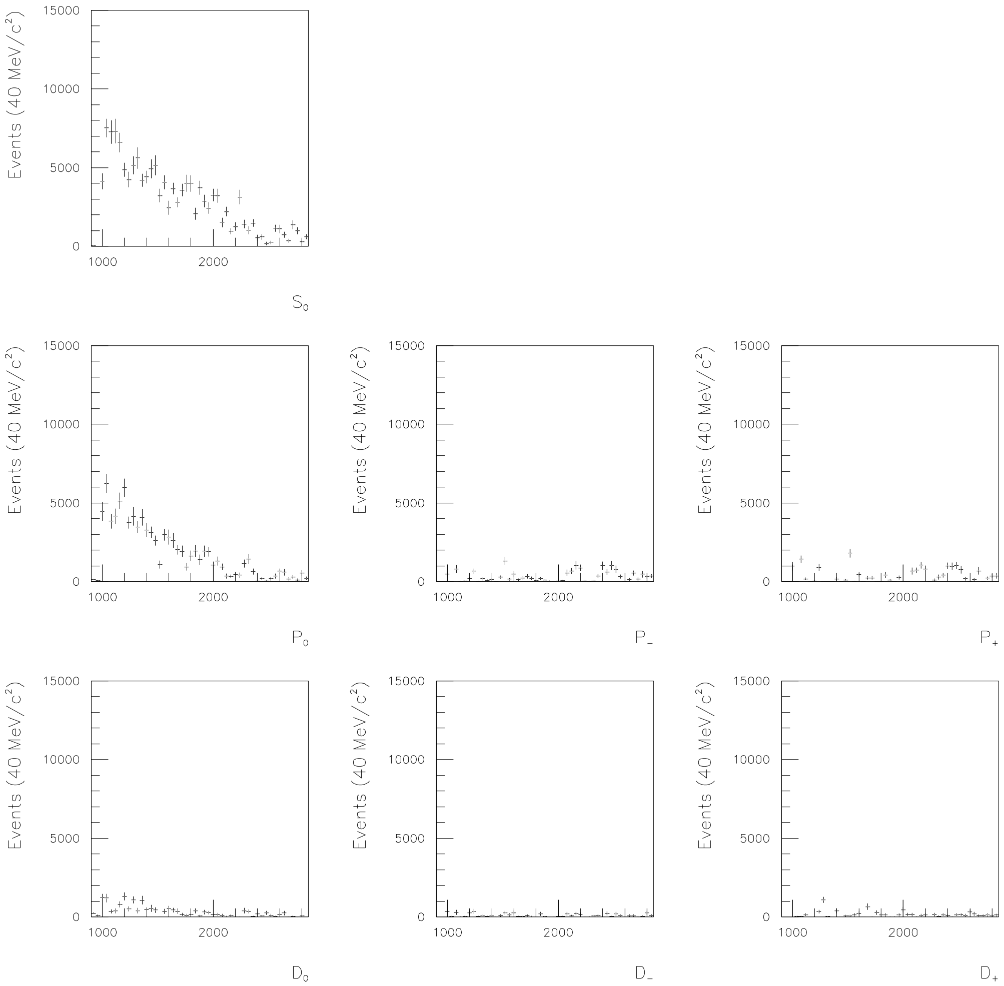

Figure B.4: Solution 4 rejected as being unphysical, from the PWA of an S-wave phase-space.

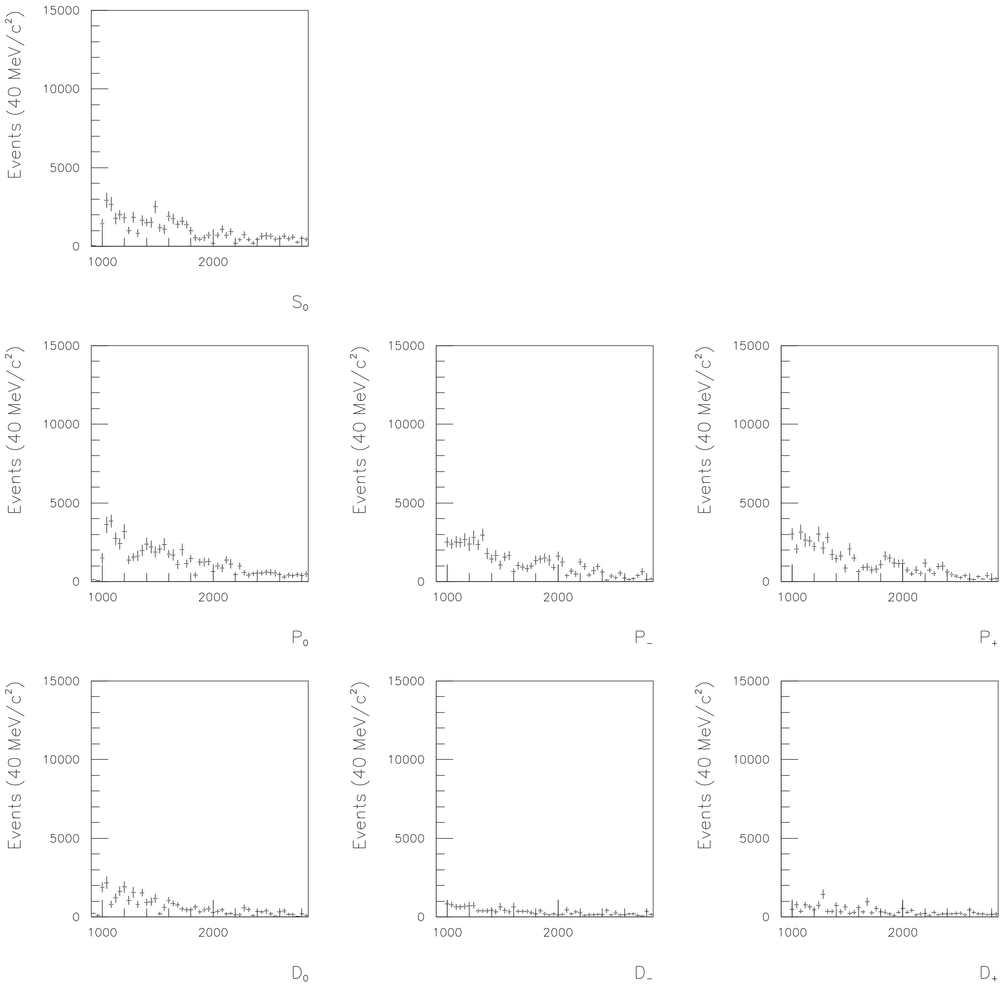

Figure B.5: Solution 5 rejected as being unphysical, from the PWA of an S-wave phase-space.

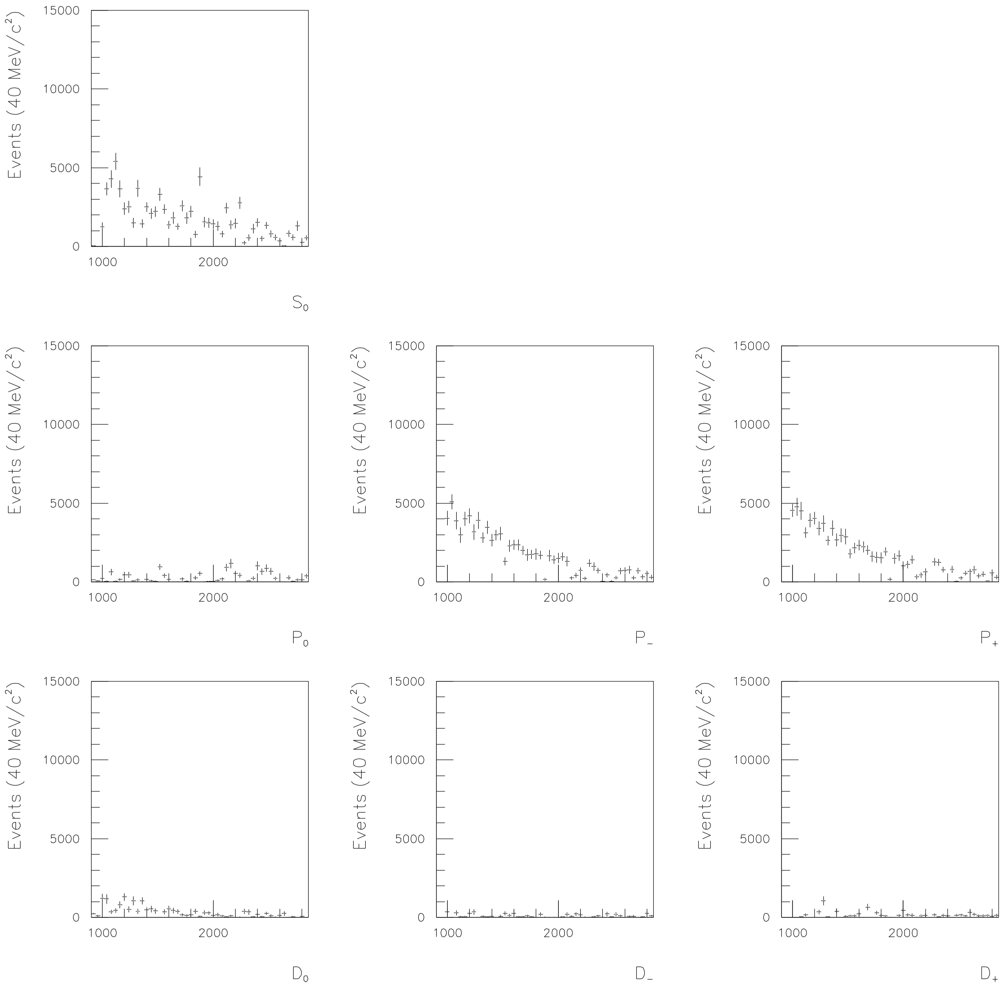

Figure B.6: Solution 6 rejected as being unphysical, from the PWA of an S-wave phase-space.

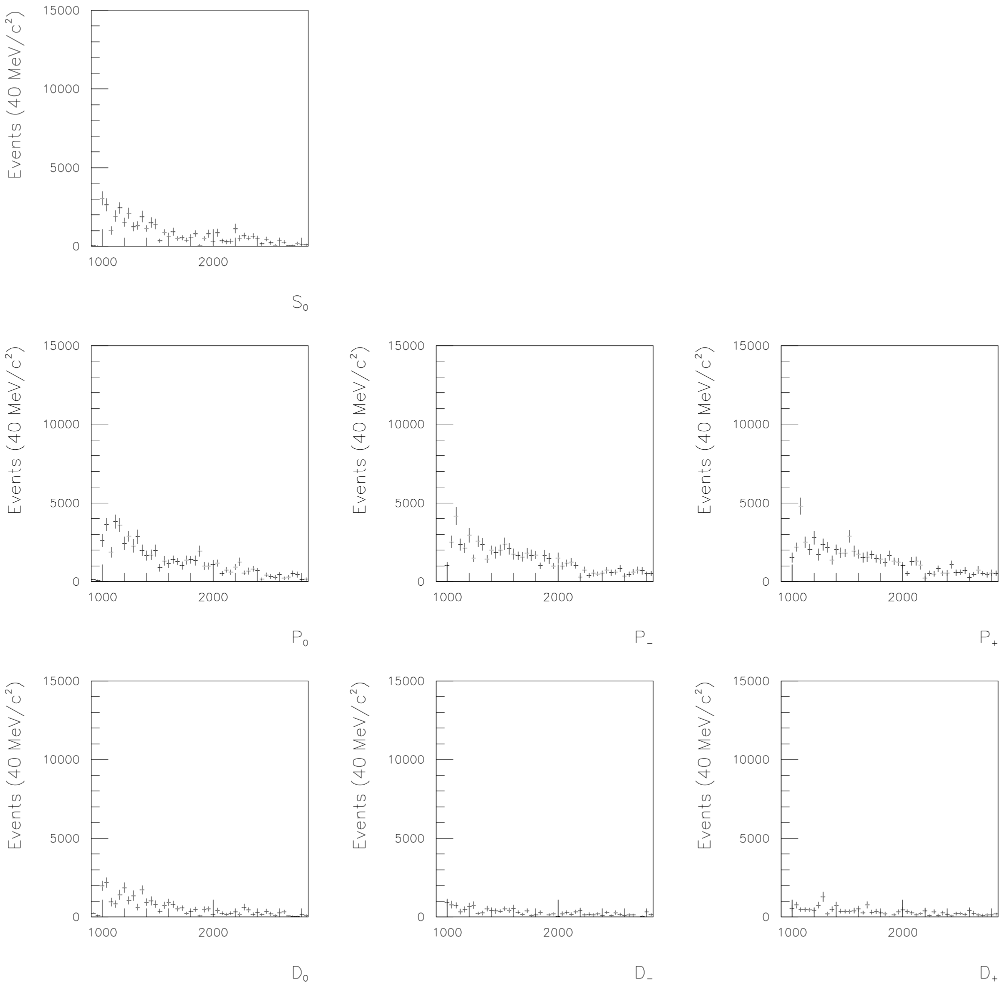

Figure B.7: Solution 7 rejected as being unphysical, from the PWA of an S-wave phase-space.

B.2 Unphysical Solutions: 1996 K^+K^- Data

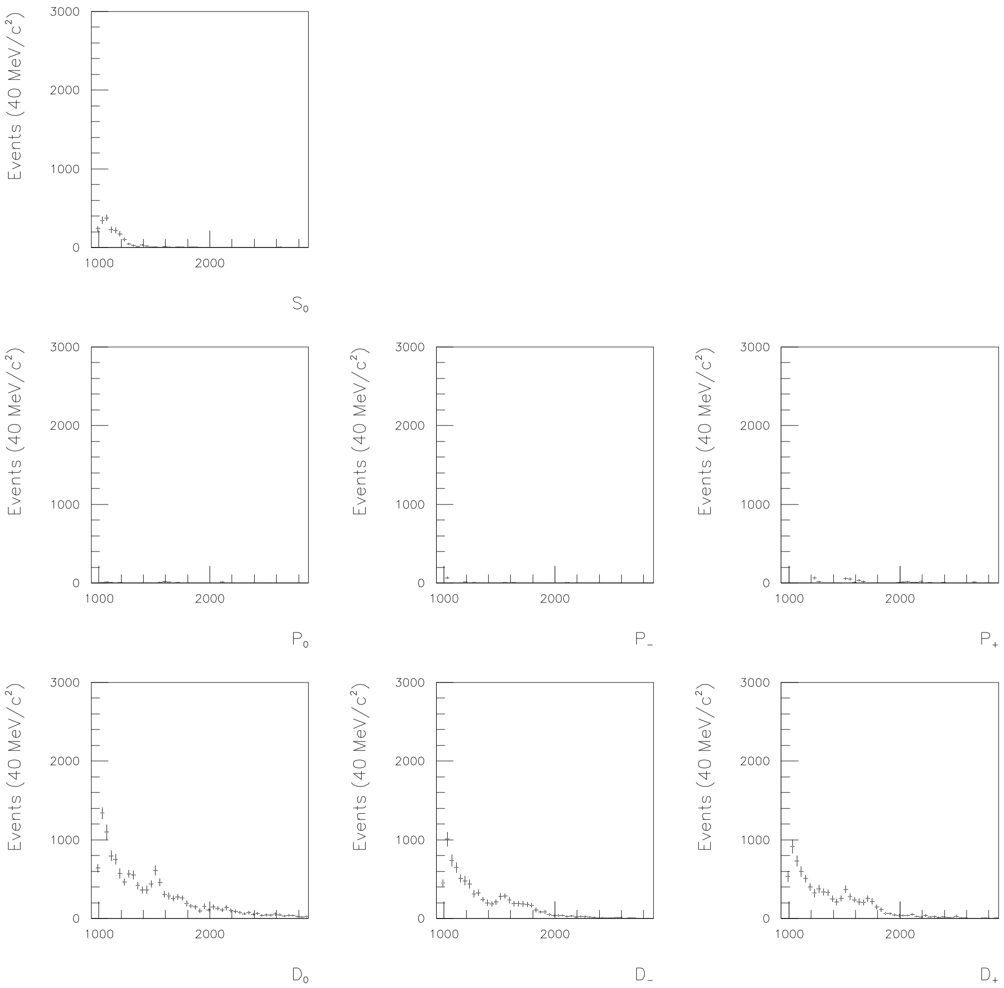

Figure B.8: Solution 1 rejected as being unphysical, from the PWA of the acceptance corrected 1996 K^+K^- data.

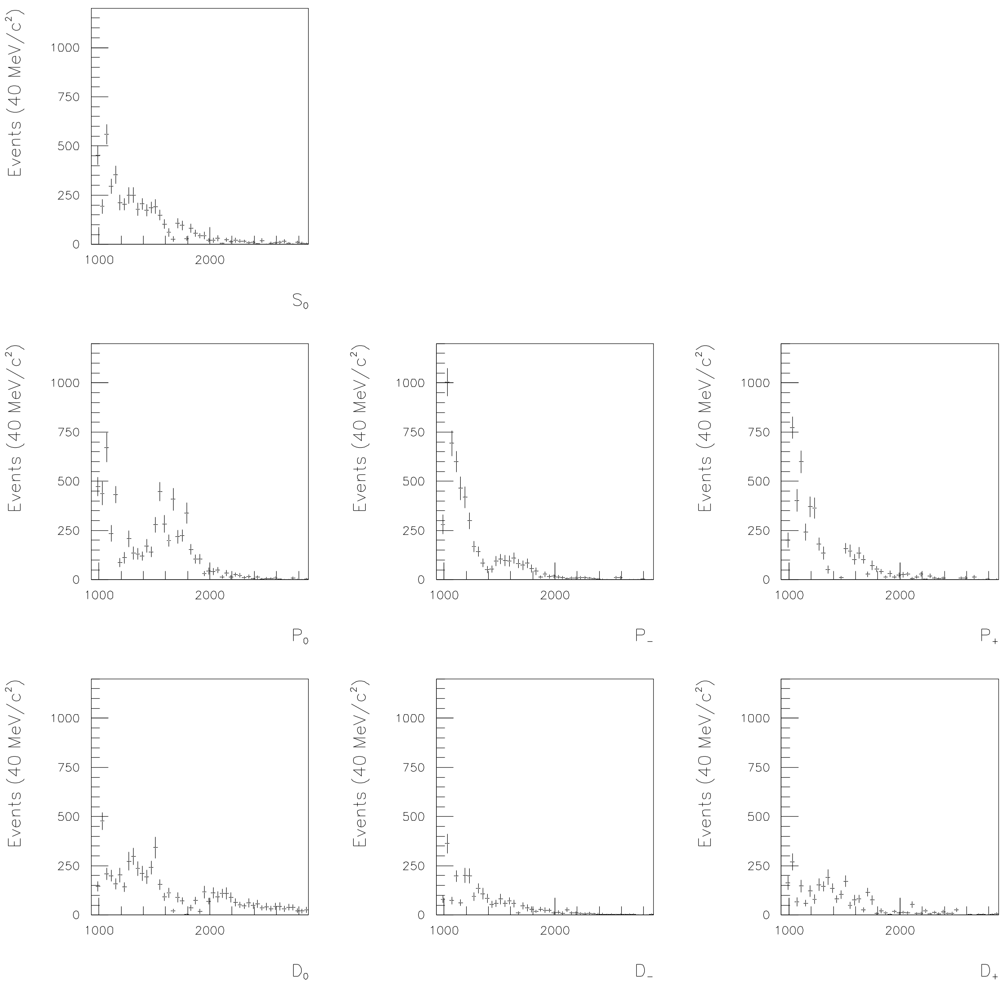

Figure B.9: Solution 2 rejected as being unphysical, from the PWA of the acceptance corrected 1996 K^+K^- data.

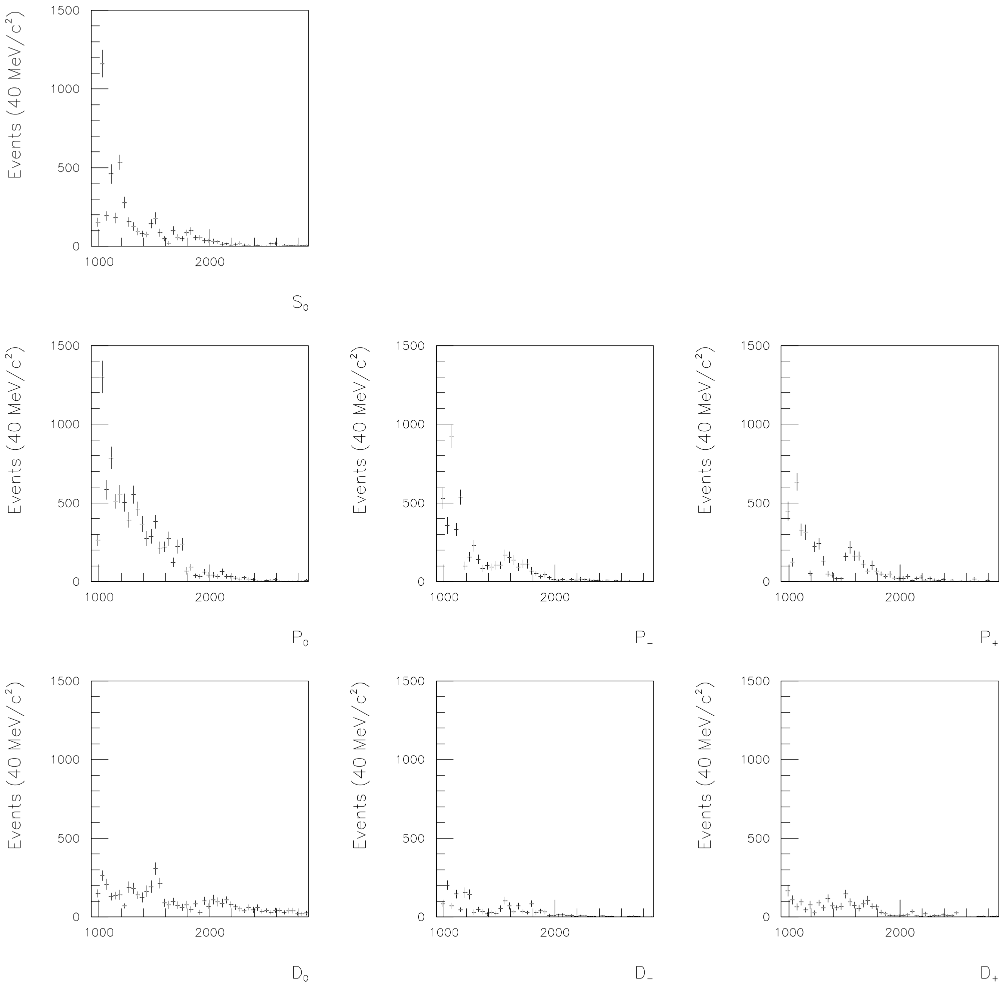

Figure B.10: Solution 3 rejected as being unphysical, from the PWA of the acceptance corrected 1996 K^+K^- data.

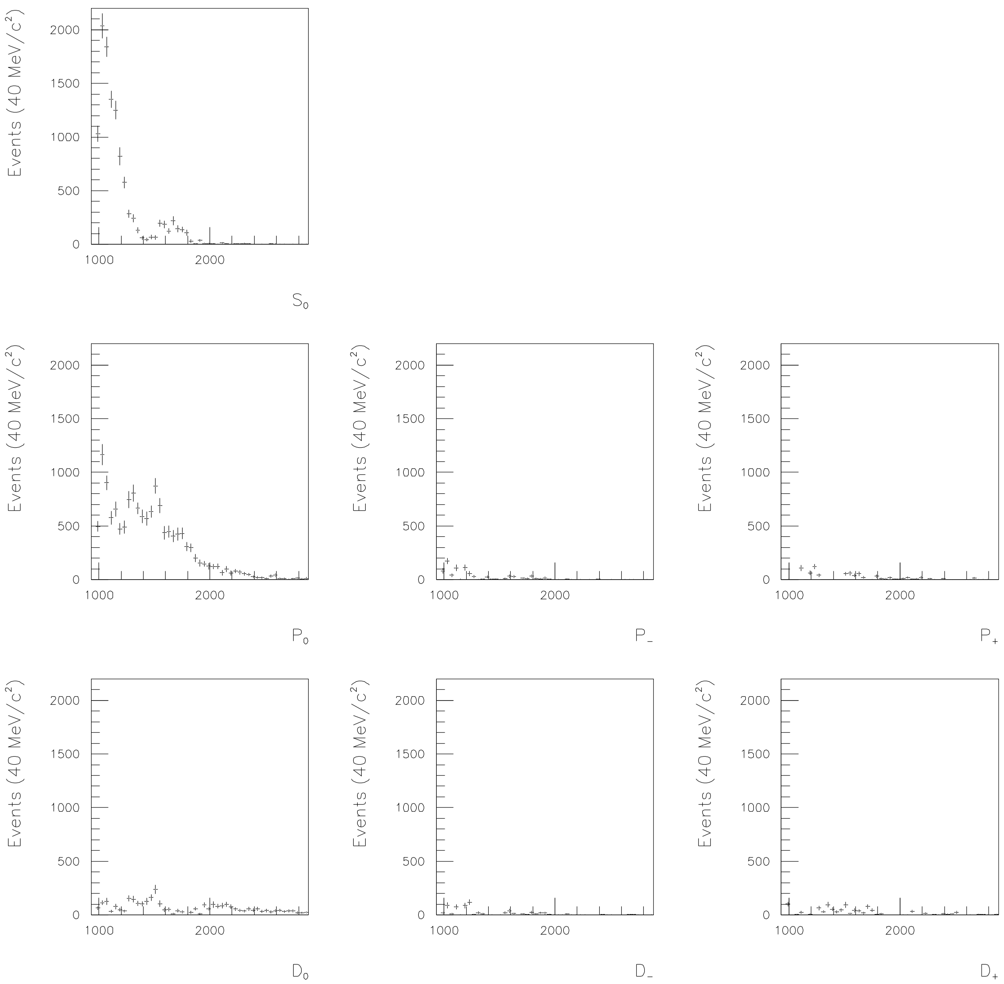

Figure B.11: Solution 4 rejected as being unphysical, from the PWA of the acceptance corrected 1996 K^+K^- data.

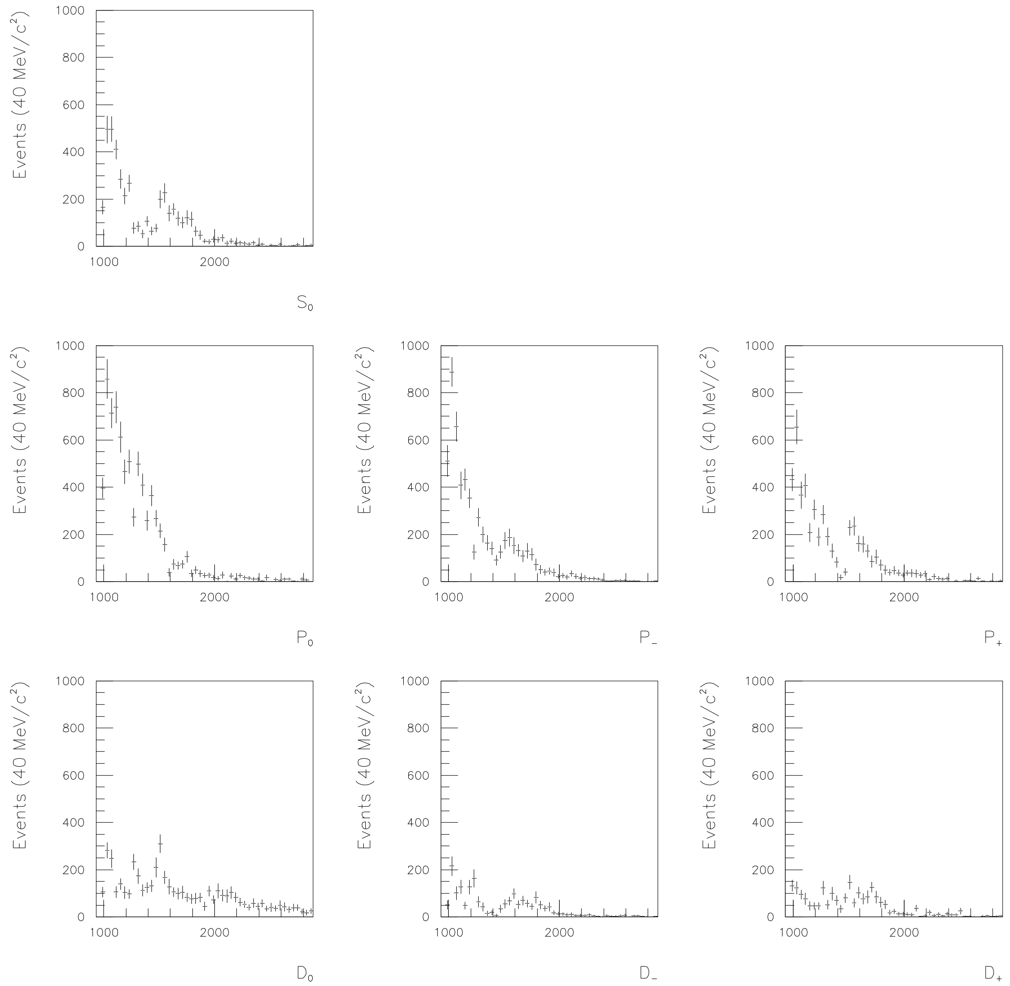

Figure B.12: Solution 5 rejected as being unphysical, from the PWA of the acceptance corrected 1996 K^+K^- data.

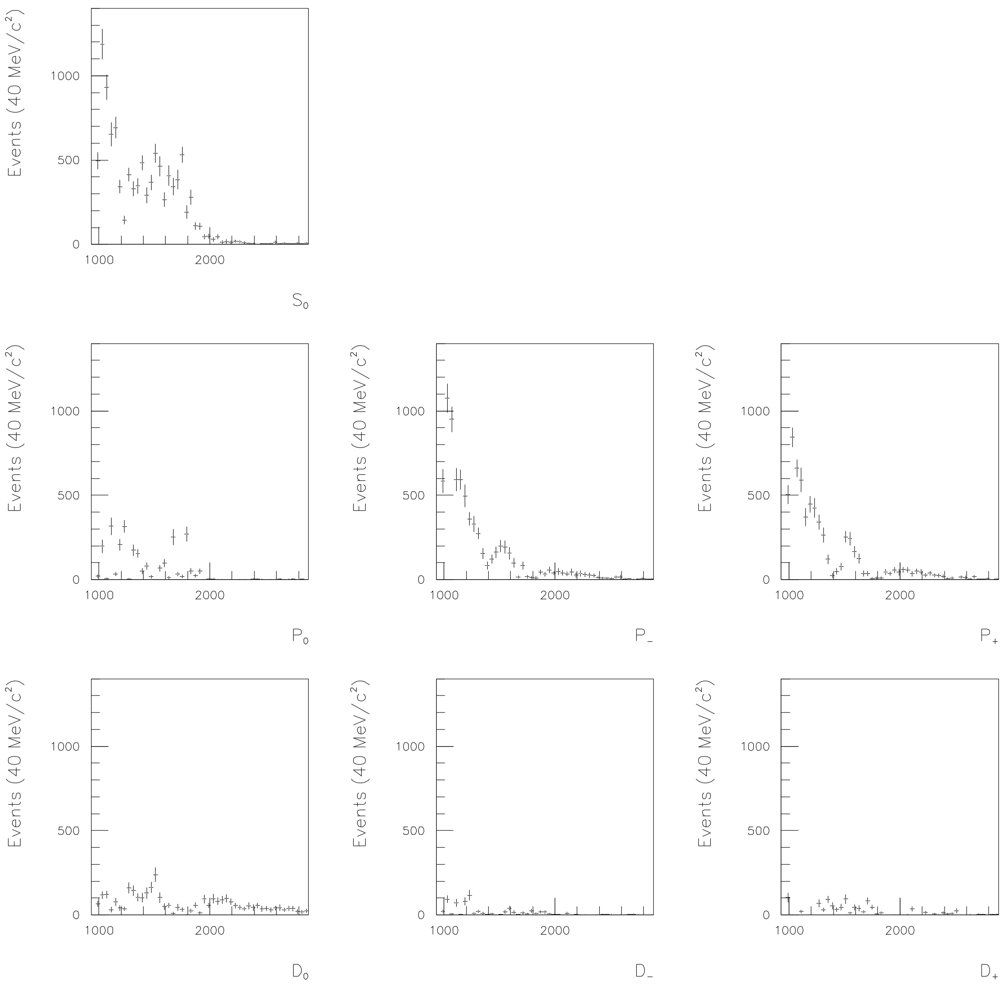

Figure B.13: Solution 6 rejected as being unphysical, from the PWA of the acceptance corrected 1996 K^+K^- data.

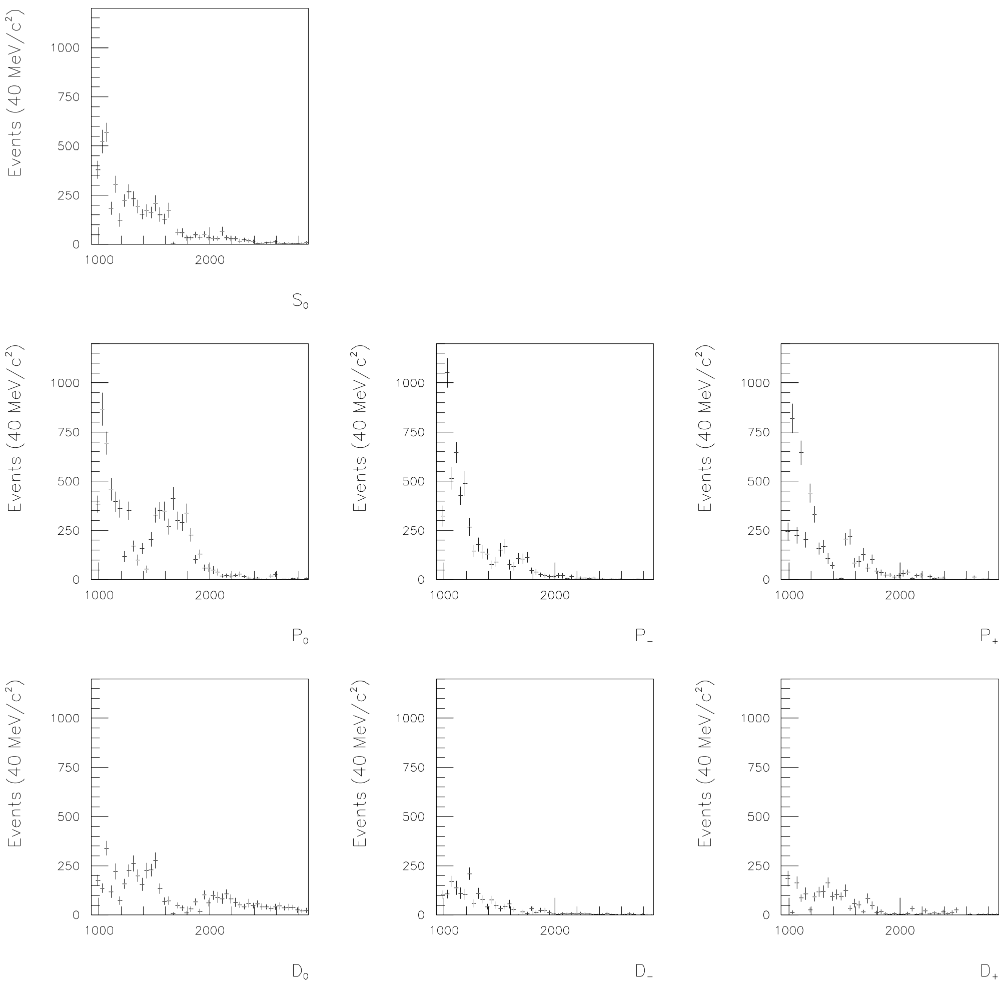

Figure B.14: Solution 7 rejected as being unphysical, from the PWA of the acceptance corrected 1996 K^+K^- data.

Bibliography

[1] S.F. Mason, 'A History of the Sciences' (1962) MacMillan Press

[2] M. Gell-Mann, Proceedings of the International Conference on High-Energy Nuclear Physics, Geneva (1962) 805

[3] V.E. Barnes *et al.*, Phys. Rev. Lett. **12** (1964) 204

[4] M. Gell-Mann, Phys. Lett. **8** (1964) 214

[5] G. Zweig, CERN-TH/401, 402, 412 (1964)

[6] M. Teper, Lectures given at Isaac Newton Institute, NATO-ASI School (1997), hep-lat/9711011

[7] F. Butler *et al.*, Phys. Rev. Lett. **70** (1993) 2849
F. Butler *et al.*, Nucl. Phys. **B430** (1994) 179
F. Butler *et al.*, Nucl. Phys. **B421** (1994) 217

[8] W. Lee and D. Weingarten (1998), hep-lat/9805029

[9] A. Vaccarino and D. Weingarten, to appear

[10] C. Morningstar and M. Peardon, Phys. Rev. **D56** (1997) 4043

[11] M. Teper, Talk given at HEP97, Jerusalem (1997), hep-ph/9711299

[12] G. Bali *et al.*, Phys. Lett. **B309** (1993) 378

[13] J. Sexton, A. Vaccarino and D. Weingarten, Phys. Rev. Lett. **75** (1995) 4563

[14] S.N. Ganguli and D.P. Roy, Phys. Rep. **67** (1980) 203

[15] F.E. Close, Rep. Prog. Phys. **51** (1988) 833

[16] D. Robson, Nucl. Phys. **B130** (1977) 328

[17] S. Okuba, Phys. Lett. **5** (1963) 165
J. Iizuka, Prog. Theor. Phys. Suppl. **37** – **38** (1966) 21

[18] S.J. Lindenbaum and H.J. Lipkin, Phys. Lett. **B149** (1984) 407

[19] G.M. Beladidze *et al.*, Phys. Lett. **B313** (1993) 276

[20] D.R. Thompson *et al.*, Phys. Rev. Lett. **79** (1997) 1630

[21] A. Abele *et al.*, Phys. Lett. **B423** (1998) 175

[22] F.E. Close, G.R. Farrar and Z. Li, Phys. Rev., **D55** (1997) 5749

[23] S.S. Gershtein *et al.*, Zeit. Phys. **C24** (1984) 305
R. Akhoury and J.-M. Frère, Phys. Lett. **B220** (1989) 258

[24] D. Barberis *et al.*, Phys. Lett. **B397** (1997) 339

[25] F.E. Close and A. Kirk, Phys. Lett. **B397** (1997) 333

[26] A. Kirk, Submitted to Yadernaya Fiz. (1998), hep-ex/9803024

[27] I. Pomerančuk, Sov. Phys. JETP. **7** (1958) 499

[28] K. Goulianos, Phys. Rep. **101** (1983) 169

[29] P. Landshoff, 'The Two Pomerons', 2$^{\text{nd}}$ Summer School on Neutron Scattering Zuoz, Switzerland (1994), hep-ph/9410250.

[30] A. Donnachie and P. Landshoff, Phys. Lett. **B296** (1992) 227

[31] P.D.B. Collins and A.D. Martin, 'Hadron Interactions', Adam Hilger Ltd. (1984)

[32] R. Bonino *et al.*, Phys. Lett., **B211** (1988) 239
A. Brandt *et al.*, Phys. Lett., **B297** (1992) 417

[33] T. Ahmed *et al.*, H1 Collaboration, Phys. Lett. **B348** (1995) 681

[34] N. Isgur and J. Weinstein, Phys. Rev. **D41** (1990) 2236

[35] V.V Anisovich *et al.*, Phys. Lett. **B323** (1994) 233

[36] C. Amsler *et al.*, Phys. Lett. **B333** (1994) 277

[37] F. Binon *et al.*, Il Nuovo Cimento **78A** (1983) 313
F. Binon *et al.*, Il Nuovo Cimento **80A** (1984) 363

[38] M.R. Pennington, 'Hadron '95 — Summary: Part I' (1995), hep-ph/9510229

[39] D. Aston *et al.*, Nucl. Phys. **B296** (1988) 493

[40] D. Aston *et al.*, Nucl. Phys. **B301** (1988) 525

[41] R.M. Baltrusaitis *et al.*, Phys. Rev. Lett. **56** (1986) 107

[42] M.S. Chanowitz (1984) Proc. VI Int. Workshop on Photon-Photon Collisions, Lake Tahoe, World Scientific (1984) p.95

[43] S. Cartwright *et al.*, 5th UK Phenomenology Workshop on LEP2 Physics, Oxford, UK (1997), hep-ph/9708478

[44] C. Amsler and F.E. Close, Phys. Lett. **B353** (1995) 385

[45] D. Alde *et al.*, Nucl. Phys. **B269** (1986) 485

[46] D. Alde *et al.*, Phys. Lett. **B201** (1988) 160

[47] T.A. Armstrong *et al.*, Phys. Lett. **B228** (1989) 536

[48] D. Barberis *et al.*, Phys. Lett. **B413** (1997) 217

[49] T.A. Armstrong *et al.*, Z. Phys. **C51** (1991) 351

[50] S. Abatzis *et al.*, Phys. Lett. **B324** (1994) 509

[51] F. Antinori *et al.*, Phys. Lett. **B353** (1995) 589

[52] A. Abele *et al.*, Phys. Lett. **B380** (1996) 453

[53] D.V. Bugg *et al.*, Phys. Lett. **B353** (1995) 378

[54] C. Amsler *et al.*, Phys. Lett. **B340** (1994) 259

[55] C. Amsler *et al.*, Phys. Lett. **B342** (1995) 433

[56] C. Amsler *et al.*, Phys. Lett. **B353** (1995) 571

[57] A. Abele *et al.*, Phys. Lett. **B385** (1996) 425

[58] S.M. Flatté *et al.*, Phys. Lett. **B38** (1972) 232

[59] M.A. Reyes *et al.*, Nucl. Phys. (Proc. Suppl.) **56A** (1997) 285

[60] M.A. Reyes *et al.*, Published in proceedings of Hadron '97 (1997) 113

[61] C. Edwards *et al.*, Phys. Rev. Lett. **48** (1982) 458

[62] W. Toki, Published in SLAC Summer Institute on Particle Physics (1984) 471

[63] U. Mallik, published in strong interactions and gauge theories, proceedings of the hadronic session (v 2) J. Tran Thanh Van Ed. Frontières, Gif-sur-Yvette (1986) 431

[64] R.M. Baltrusaitis *et al.*, Phys. Rev. **D35** (1987) 2077

[65] L.P. Chen *et al.*, Nucl. Phys. (Proc. Suppl.) **B21** (1991) 80

[66] L.P. Chen *et al.*, Published in: Hadron '91 Proceedings, S. Oneda and D.C. Peaslee World Sci., Singapore (1992) 111

[67] W. Dunwoodie, Published in: Upton, Hadron spectroscopy (1997) 753

[68] T.A. Armstrong *et al.*, Phys. Lett. **B227** (1989) 186

[69] J.Z. Bai *et al.*, Phys. Rev. Lett. **77** (1996) 3959

[70] T.A. Armstrong *et al.*, Phys. Lett. **B307** (1993) 394

[71] R.M. Baltrusaitis *et al.*, Phys. Rev **D33** (1986) 1222

[72] Particle Data Group, European Physical Journal **C3** (1998) 1

[73] D. Weingarten, Nucl. Phys. (Proc. Suppl.) **B53** (1997) 232

[74] F. Antinori *et al.*, Il Nuovo Cimento **A107** (1994) 1857

[75] T.A. Armstrong *et al.*, Nucl. Instr. and Meth. **A274** (1989) 165

[76] D. Alde *et al.*, Nucl. Instr. and Meth. **A240** (1985) 343

[77] W. Beusch *et al.*, Nucl. Instr and Meth. **A249** (1986) 391

[78] K.L. Norman, 'An Analysis of the Centrally Produced $\pi^+\pi^-$ System at 450 GeV/c', Ph.D. Thesis, Univerisity of Birmingham (1996)

[79] S. Clewer, 'Analysis of the Central $K^0_S K^\pm \pi^\mp$ System and Determination of the $f_1(1285)$ Branching Ratio at 450 Gev/c', Ph.D. Thesis, University of Birmingham (1994)

[80] R. Ehrlich *et al.*, Phys. Rev. Lett. **20** (1968) 686

[81] J. Pumplin and F.S. Henvey, Nucl. Phys. **B117** (1976) 377

[82] GEANT, CERN Program Library Long Writeup **W5013** Version 3.21 (1995)

[83] D.M. Brink and G.R. Satchler, 'Angular Momentum', Oxford University Press (1968)

[84] K. Gottfried and J.D. Jackson, Il Nuovo Cimento **33** (1964) 309

[85] S.U. Chung, Phys. Rev. **D56** (1997) 7299

[86] G. Costa et al., Nucl. Phys. B175 (1980) 402

[87] A. Etkin *et al.*, Phys. Rev. **D25** (1982) 1786

[88] F. James and M. Roos, MINUIT, CERN Program Library Long Writeup **D506** Version 94.1 (1994)

[89] S.A. Sadovsky, 'On the Choice of Minimization Functional in the Partial Wave Analysis', IHEP Preprint 91-15 (1991)

[90] M. Reyes, 'Analysis of the decay products from the interaction pp $\longrightarrow$ $p_s(K^0_S K^0_S)p_f$ at 800 GeV/c^2, Ph.D. Thesis, Cinvestav, Mexico (1996)

[91] E. Barrelet, Il Nuovo Cimento **8A** (1972) 331

[92] WPOLYZ, CERNLIB Short Writeup **C209** (1992)

[93] D. Barberis *et al.*, To be printed in Phys. Lett. (1999), hep-ex/9903042

[94] J.D. Jackson, Il Nuovo Cimento **34** (1964) 6692

[95] S.M. Flatté, Phys. Lett. **B63** (1976) 224

[96] A. Kirk and O. Villalobos-Baillie (1998), hep-ph/9811230